Qualification of the Code d³f++

Qualification of the Code d³f++

Anke Schneider
Anne Gehrke
Klaus-Peter Kröhn
Hong Zhao

February 2017

Acknowledgement

Abstract

The code d³f++ is a modern tool for modelling density-driven flow and nuclide transport in the far field of repositories for hazardous material in deep geological formations. It is applicable in porous media as well as in fractured rock or mudstone, for modelling salt- and heat transport as well as a free groundwater surface.

The objective of this work is proving the capability of code d³f++ to simulate correctly density-driven flow and pollutant transport in large scale, complex geological situations in order to improve the confidence in groundwater modeling in general. The applications presented in this report are related to haline and thermohydraulic groundwater flow and transport in porous or fractured media. Among them are laboratory and field experiments as well as real site studies. The d³f++ results are verified by measurements or compared to the results of other density-driven flow codes.

Three applications presented are related to Task 8 defined by the Task Force on Groundwater Flow and Transport of Solutes (TF GWFTS) of SKB to investigate the hydraulic interaction of the fractured, granitic host rock and the bentonite clay buffer in a deep geological repository at the Hard Rock Laboratory (HRL) at Äspö. Presented are the results from work on the Buffer-Rock-Interaction-Experiment (BRIE) in the framework of Tasks 8c and 8d and on the Prototype Repository in the framework of Task 8e.

Another application refers to a thermal injection and storage experiment in the Borden field research site. These works are focused on heat flow and free surface modeling.

A 2d benchmark based on a laboratory experiment concerning formation and degradation of a freshwater gave the possibility to compare the results of various density-driven flow codes.

The Waste Isolation Pilot Plant (WIPP) is a repository for transuranic waste in New Mexico, USA. A 6,000 km², basin scale model of the WIPP-Site overburden is presented here with the objective to enhance the understanding of the groundwater flow dynamics in the basin as well as to show the ability of d³f++ to set-up a strongly anisotropic, 3d model of these extension, to simulate density-driven groundwater flow and to handle a free groundwater surface of these dimension.

Zusammenfassung

Das Programm d³f++ wurde mit dem Ziel entwickelt, die dichtebeeinflusste Grundwasserströmung und den Transport von Nukliden und anderen Schadstoffen im Fernfeld von Endlagern in tiefen geologischen Formationen modellieren zu können. Es ist sowohl in porösen Medien als auch im Kluftgestein, zur Modellierung des Salz- und Wärmetransportes sowie in Gebieten mit freier Grundwasseroberfläche einsetzbar.

Ziel der hier präsentierten Arbeiten war es nachzuweisen, dass der erst kürzlich auf eine neue Softwarebasis transformierte Code d³f++ in der Lage ist, Dichteströmung und Stofftransport in großen, geologisch komplexen Modellgebieten korrekt zu simulieren. Die dafür herangezogenen Anwendungen beziehen sich auf haline und thermohydraulische Grundwasserströmungen in porösen sowie geklüfteten Medien. Es werden Labor- und Feldexperimente sowie reale, regionale Anwendungsfälle betrachtet. Die Resultate von d³f++ werden anhand von Messwerten verifiziert oder mit den Resultaten anderer Codes verglichen.

Drei der präsentierten Anwendungen beziehen sich auf Task 8 der Task Force on Groundwater Flow and Transport of Solutes (TF GWFTS) von SKB. Dabei werden die hydraulischen Interaktionen des klüftigen Granits als Wirtsgestein mit dem Bentonitversatz im Tiefenlager des Hard Rock Laboratory (HRL) Äspö untersucht. Gezeigt werden Ergebnisse zum Buffer-Rock-Interaction-Experiment (BRIE) im Rahmen der Tasks 8c und 8d sowie des Proto-type Repositorys in Task 8e.

Weiterhin wird ein thermisches Injektions- und Speicherexperiment in der Borden Site (USA) untersucht. Dabei geht es vor allem um die Modellierung des Wärmetransportes und der freien Grundwasseroberfläche.

Im Rahmen eines 2d Benchmarks, basierend auf Laborexperimenten zur Entwicklung und Zurückbildung einer Süßwasserlinse, wurden die Ergebnisse mehrerer Dichteströmungsprogramme miteinander verglichen.

Schließlich wird ein Deckgebirgsmodell der Waste Isolation Pilot Plant (WIPP), eines Endlagers in New Mexico, dargestellt. Damit soll ein besseres Verständnis der Grundwasserströmung in dem 6.000 km² großen Becken erreicht werden. Es handelt sich um ein stark anisotropes Modell mit freier Grundwasseroberfläche.

Table of contents

1   Introduction

Long term safety assessment for a repository requires a comprehensive system under-standing and qualified high-performance tools. These tools have to be able to describe all relevant processes concerning nuclide transport through the host rock or the related geological formations, respectively.

To meet the needs of modeling groundwater flow and nuclide transport, starting from from 1994 the computer codes d³f (distributed density-driven flow) and r³t (radio-nuclides, reaction, retardation, and transport) were developed /FEI 99/, /FEI 04/, and af-terwards step by step advanced as well as continuously adapted to the state-of-the-art of science and technology /SCH 12/, /SCH 13/, /NOS 12/. The codes d³f and r³t were based on version 3 of the UG Toolbox, developed at the Frankfurt University /BAS 97/. Recently, they were adapted to the substantially updated, C++-based version UG4 /VOG 13/, and during this process the codes were combined to one conjoint code named d³f++ /SCH 16/. All these works were funded by the Federal Ministry of Education and Research (BMBF) and by the Federal Ministry of Economics and Technology (BMWi), respectively.

According to the German safety case requirements for heat-generating radioactive waste an assessment period of one million years has to be regarded, and the requirements on modeling are growing: Today regional-scale models are asked for, and the demands for accuracy and grid resolution are growing.

By means of d³f++ it is feasible to simulate density-driven flow and pollutant transport in porous and fractured media, including heat transport as well as free surface flow on large model domains with complex hydrogeological structures. In the past, various appli-cations and test cases were performed by d³f, r³t, among them examples from literature, laboratory and field experiments as well as practical applications, see e. g. /SCH 04/, /FEI 08/, /GRI 10/ and /SCH 12/. The results were compared to analytical solutions, measurements or results of other codes. One laboratory experiment developed in the context of density-driven flow was the Saltpool test case /OSW 98/, /JOH 02/.

The content of the work reported here is the modeling of groundwater flow and transport for laboratory and field experiments as well as for real site applications. The objective

was proving the capability of the new code d³f++ to simulate correctly density-driven flow and pollutant transport in large scale, complex geological situations in order to improve the confidence in groundwater modeling in general.

The applications presented here are related to haline and thermo-hydraulic groundwater flow and transport in porous or fractured media. Among them are laboratory and field experiments as well as real site studies. The d³f++ results are verified by measurements or compared to the results of other density-driven flow codes.

1.1   The code d³f++

The new d³f++ implementation based on the open-source UG4 software package is based on an object-oriented software design and written in C++. The system of partial differential equations to be solved is described in chapter 1.2.

For spatial discretization, finite volume methods are used, ensuring mass conservation. The time dependent system is discretized by an implicit Euler algorithm because this method allows large time steps.

The nonlinearity is solved by a modified Newton algorithm. Geometric and algebraic multigrid methods are used as the most effective solvers of large linear equation systems. d³f++ can not only be run on desktop as well as on massively parallel computers, it also may make use of modern multicore and hybrid computer structures /HEP 13/, /REI 13/.

The recently developed preprocessor tool ProMesh (www.promesh3d.com) and the graphical user interface /HOF 13/ enable the user to set-up regional, complex-structured models in a comfortable way.

1.2   Basic equations of d³f++

The thermohaline groundwater flow in porous media is modelled by a coupled system of nonlinear, time-dependent differential equations for the brine mass fraction, the pressure and the temperature. Let $\Omega \subset \mathbb{R}^d$ be a physical domain and let the brine mass fraction $\omega \colon \Omega \mapsto \mathbb{R}\ [-]$, the pressure $p \colon \Omega \mapsto \mathbb{R}\ [Pa]$ and the temperature $\theta \colon \Omega \mapsto \mathbb{R}\ [K]$ be the unknown functions. The system of equations for thermohaline flow is given by

$$\begin{cases} \qquad\qquad Find\ (\omega, p, \theta),\ such\ that \\[1em] \qquad\qquad\qquad\quad \partial_t(\phi\rho) + \nabla \cdot (\rho\boldsymbol{q}) = Q,\quad in\ \Omega, \\ \qquad\qquad \partial_t(\phi\rho\omega) + \nabla \cdot (\rho\omega\boldsymbol{q} - \rho\boldsymbol{D}\nabla\omega) = Q_s,\quad in\ \Omega, \\ \partial_t\left((\phi\rho C_f + (1-\phi)\rho_s C_s)\theta\right) + \nabla \cdot (\rho C_f \boldsymbol{q}\theta - \Lambda\nabla\theta) = 0,\quad in\ \Omega, \\[1em] \qquad\qquad\qquad \boldsymbol{q} = -\dfrac{\boldsymbol{k}}{\mu}(\nabla p - \rho\boldsymbol{g}), \end{cases} \qquad (1.1)$$

where the first equation describes the mass conservation of the fluid, the second the mass conservation of the brine and the third one the heat conservation. The physical parameters are given by:

- ϕ [-]: the porosity
- $\rho \equiv \rho(\omega)$ [$kg\ m^{-3}$]: the fluid density
- $\mu \equiv \mu(\omega)$ [$kg\ m^{-1}\ s^{-1}$]: the fluid viscosity
- $\mathbf{D}_{\mathrm{disp}} \equiv \mathbf{D}_{\mathrm{disp}}(\mathbf{q})$ [$m^2 s^{-1}$]: the mechanical dispersion tensor
- $D_{\mathrm{m}} \equiv D_{\mathrm{m}}$ [$m^2 s^{-1}$]: the molecular diffusion coefficient
- $\mathbf{T}$ [$-$]: the tortuosity tensor
- $\mathbf{D} \equiv \phi\, D_m\, \mathbf{T} + \mathbf{D}_{\mathrm{disp}}(\mathbf{q})$ [$m^2 s^{-1}$]: the hydrodynamic dispersion tensor
- $\mathbf{k}$ [m^2]: the permeability tensor
- $\mathbf{g}$ [$m\ s^{-2}$]: the gravity vector
- Λ [$W\ m^{-1}\ K^{-1}$]: the thermal conductivity
- C_s [$J\ kg^{-1}\ K^{-1}$]: the heat capacity of the solid / rock
- C_f [$J\ kg^{-1}\ K^{-1}$]: the heat capacity of the fluid
- ρ_s [$kg\ m^{-3}$]: the rock density

Q and Q_s at the right hand site denote source and sink terms. For the dispersion tensor the Bear-Scheidegger-Modell can be used, given by:

$$\boldsymbol{D}_{disp}(\boldsymbol{q}) = \alpha_L \boldsymbol{I} + (\alpha_L - \alpha_T)\frac{\boldsymbol{q}\cdot\boldsymbol{q}^T}{||\boldsymbol{q}||}, \qquad (1.2)$$

with the parameters:

- α_L [m]: the longitudinal dispersion length
- α_T [m]: the transverse dispersion length

The transport of radionuclides is modelled using a physical system of convection-diffusion type. The velocity field used for the convection is given by the Darcy velocity as a result of the flow equations.

Let $\Omega \subset \mathbb{R}^d$ be a physical domain and let the radionuclide concentration $c_i : \Omega \mapsto \mathbb{R}$ [$mol \, m^3$] be the unknown function. The system of equations for the transport is given by

$$
\left\{
\begin{array}{c}
Find \ (c_i), such \ that \\[2mm]
\partial_t(\phi R_i c_i) + \nabla \cdot (c_i \boldsymbol{q} - \boldsymbol{D}\nabla c_i) + \phi R_i \lambda_i c_i = Q_i, \ in \ \Omega.
\end{array}
\right.
\tag{1.3}
$$

The physical parameters are given by:
- ϕ [$-$]: the porosity
- ρ_r [$kg \, m^{-3}$]: the rock density
- $K_d^{(i)}$ [$m^3 \, kg^{-1}$]: the distribution coefficient
- $R_i = 1 + \frac{1-\phi}{\phi} \rho_r K_d^{(i)}$ [$-$]: the retardation factor
- $\boldsymbol{D}$ [$m^2 s^{-1}$]: the diffusion-dispersion tensor
- $\boldsymbol{q}$ [$m \, s^{-1}$]: the darcy velocity
- $T_{1/2}^{(i)}$ [s]: the half-life
- $\lambda_i = \frac{\ln 2}{T_{1/2}^{(i)}}$ [s^{-1}]: the decay constant

The source term Q_i includes those radionuclides k that decay into radionuclide i,

$$
q_i = \phi \sum_k R_k \lambda_k \, c_k ,
\tag{1.4}
$$

with:

- λ_k: the decay constant of radionuclide k
- c_k: the concentration of radionuclide k

2 Flow and transport in fractured media

2.1 Introduction

The Task Force on Groundwater Flow and Transport of Solutes (TF GWFTS) and the Task Force on Engineered Barrier Systems (TF EBS) both established by the Svensk Kärnbränslehantering AB (SKB) had defined the so-called Task 8 to investigate the hydraulic interaction of the granitic host rock and the bentonite clay buffer in a deep geological repository at the Hard Rock Laboratory (HRL) at Äspö. Background for this exercise was construction and performance of the Buffer-Rock-Interaction-Experiment (BRIE). In the separate short TASO-tunnel boreholes were drilled for characterizing the flow field and for determining two suitable test boreholes. The geometry of drifts and boreholes for Task 8c is depicted in Fig. 2.1.
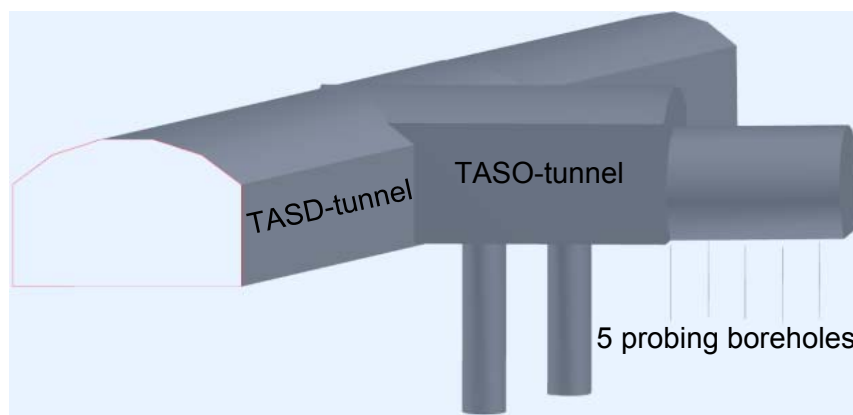
Fig. 2.1 Geometry of drifts and boreholes from the description of Task 8c /BOC 13/

The Task was divided into subtasks 8a to 8d beginning with a theoretical study of the bentonite-rock interaction (Task 8a) followed by three stages of modelling the BRIE based on increasing knowledge and data (Tasks 8b to 8d) as site characterization and the experiment itself progressed. In the following an approach is followed where the aspects of flow in the rock and water uptake by the bentonite are only weakly coupled. Groundwater flow was simplified to a steady-state single-phase flow model including discretely described large fractures. Model calculations concerning an early conceptual un-

derstanding of the site (Task 8b) were already performed with the code $d^3f++^{[1]}$ during a previous project /SCH 12/.

Not initially planned was Subtask 8e that is concerned with the full-scale Prototype Repository (PR) at the HRL at Äspö. One of the key questions of Task 8e was: Is the conceptual approach for groundwater flow that was developed for the BRIE viable at other conditions or scales?

This question could best be answered by modelling flow during the pre-installation phase of the PR meaning after excavation of tunnel and deposition boreholes but before installation of heaters, buffer and tunnel backfill. As long as the deposition holes had not been filled, the flow conditions were quite similar to the conditions at the BRIE, namely isothermal flow, a hydraulic gradient from deep in the rock towards tunnel and boreholes, flow via matrix, large deterministic fractures, as well as background fractures[2] and outflow over tunnel and borehole walls. Differences between the BRIE and the PR concern the geometry of the geotechnical openings and the size of the in-situ tests thus allowing to check the approach developed for the BRIE. A view of the tunnel system at the PR as well as the six deposition boreholes is depicted in Fig. 2.2[3].
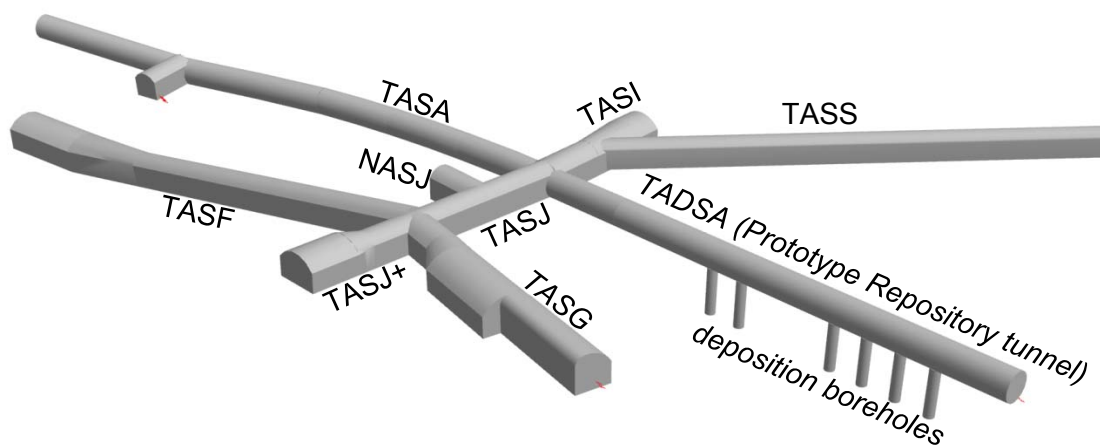
Fig. 2.2   Sketch of the tunnel system around the Prototype Repository

---

[1] formerly d^3f and r^3t
[2] fractures that are of significantly smaller scale than the model domain and are usually described in terms of stochastic mathematical relations
[3] The labelling of the tunnels in the figure is in line with the official notation. Informally, though, the TASS would also be called 'S-tunnel'.

Besides implementing the option for modelling flow and transport in fractured porous media, d^{3}f++ was also enabled to model coupled flow and heat transport /SCH 12/. Task 8e was thus also seen as an opportunity to demonstrate the capability of d^{3}f++ to simulate thermo-hydraulically (TH) coupled flow processes in fractured rock.

On the whole, work on Task 8 consisted basically of calculating outflow data from the rock and testing the features for flow and transport in fractured rock that were newly implemented in d^{3}f++ /SCH 12/. Presented in the following are the results from work on the BRIE in the framework of Tasks 8c and 8d and on the Prototype Repository in the framework of Task 8e. A much more detailed description of all modelling work concerning the BRIE can be found in /KRO 17a/ and concerning the PR in /KRO 17b/.

## 2.2   Isothermal 3D-flow at the BRIE-site

2.2.1   Task 8c

During the work with Task 8b it had become apparent that there was little data referring to steady-state flow that could be compared to model results. Only consistency and plausibility of the results could therefore be checked. This unfortunate situation had improved a little for Task 8c where some outflow data had become available. Moreover, a new definition of the large fractures and the five probing boreholes drilled in the meantime called for a new flow model for the BRIE site. With this new model, also a better representation of the fracture system could be realised.

Model geometry

The model domain suggested by the task description /BOC 13/ was cube-shaped with a side length of 40 m. The relation of the model domain to the other geotechnical structures at Äspö at a larger scale can be seen in Fig. 2.3.

In the model domain two drifts had been excavated: the TASD- and the TASO-tunnel. The drifts have a plane floor and plane walls but a domed roof. The TASD-tunnel begins outside the model domain but ends within. The TASO-tunnel branches off from the TASD-tunnel and also ends within the domain. The cross-sections of both drifts are re-

duced at the last meters towards the end of the respective drift. Contrary to the task description, these changes in the cross-section are not considered in the model presented here because they are considered to be negligible in comparison to the uncertainties introduced by other factors especially permeabilities and boundary conditions.
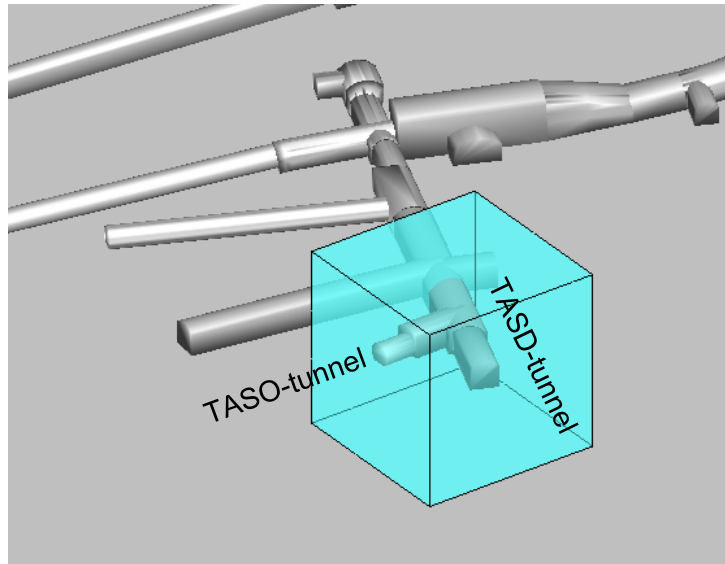

Fig. 2.3   Geometry of geotechnical structures at Äspö at a larger scale; from /BOC 13/

There are two boreholes at the bottom of the TASD-tunnel representing boreholes from the previously performed Temperature Buffer Test (TBT) and the Canister Retrieval Test (CRT), respectively. They are labelled here "deposition borehole 2" and "deposition borehole 3". Their size is not directly given but from the data it can be assumed that they have a diameter of 1.60 m and a depth of 9 m.

The geometrical model was derived from a CAD-file which contained some inaccuracies. These were not considered to be important, though, and were thus corrected in what was seen as a sensible way:

−   The intersection of TASD- and TASO-tunnel was still not resolved.

−   There was a little slope in the TASD-tunnel leading to an initial slanting of the floor of the TASO-tunnel.

−   The top of the boreholes was only approximately consistent with the floor of the drifts.

Together with five new probing boreholes in the TASO-tunnel this led to the geometry of the openings depicted in Fig. 2.4.
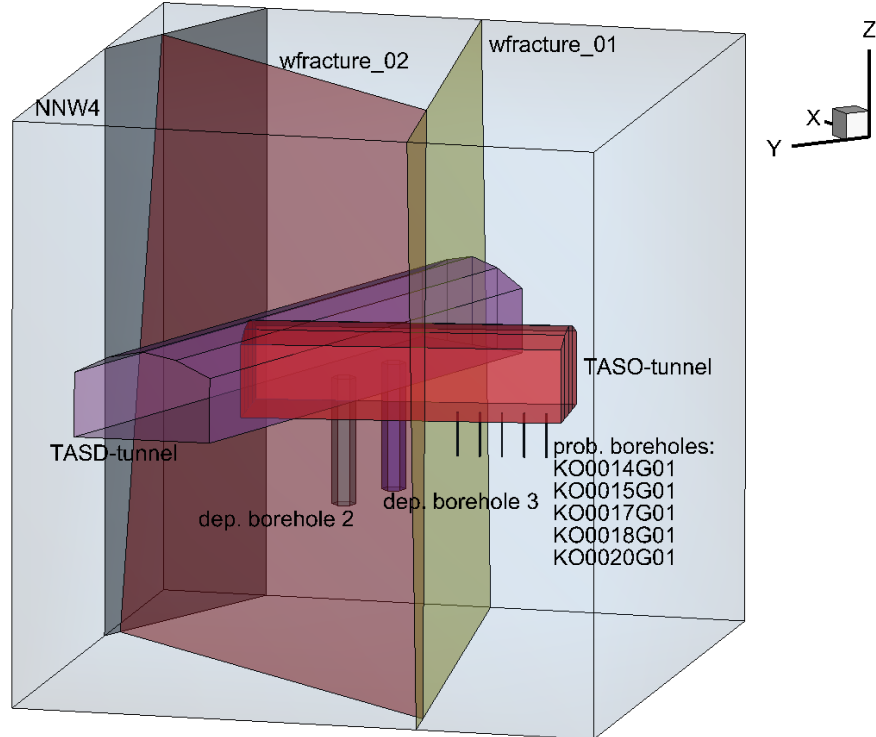

Fig. 2.4   Geometry of the geotechnical openings and location of the large fractures

Different from Task 8b, there are only three large deterministic fractures located in the model domain, all being larger than the 40 m domain. The edges of the fractures in the model are therefore defined by the interception of fractures and the model boundaries. Images of these fractures are integrated in Fig. 2.4.

Background fractures had been ignored in the model for Task 8b. This changed for Task 8c when five probing boreholes had been drilled in a row with a distance of 1.5 m and extremely different outflow rates had been observed for them. To account for this phenomenon, the vicinity of the boreholes was treated differently from the rest of the model as shown in Fig. 2.5. A box-like zone (depicted in yellow) was defined in such a way that the minimal distance of the boreholes to the zone boundary amounted to 1 m. The box was assumed to contain only undisturbed rock except for two fractures that where assumed to cross the two comparatively strong water producing probing boreholes and connected them to the outside of the box. Outside of the box an increased

matrix permeability was assumed to account for the network of smaller background fractures.
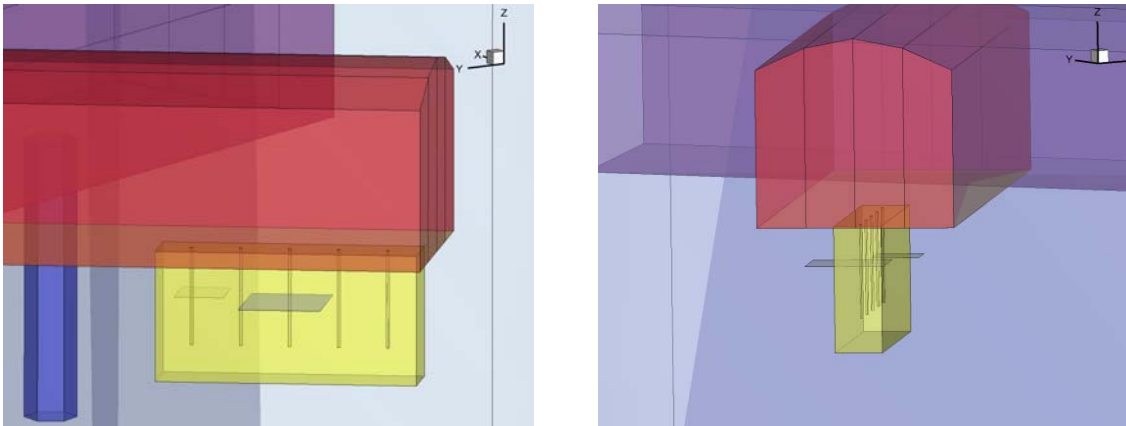
Fig. 2.5   Close-ups of the small box of undisturbed rock and the assumed fractures

Hydraulic parameters

Matrix conductivity[4] as low as 10^{-14} m/s was defined in the task description. This value translates into a permeability of 10^{-21} m². Six core measurements presented by /VIL 07/ for the rock matrix at the Forsmark site which is believed to be comparable to the rock at Äspö indicated a spectrum for the permeability roughly ranging from 10^{-21} m² to 10^{-19} m². A fracture network model for the undisturbed rock pointed in the direction of slightly less than 10^{-20} m² /SVE 12/. Measurements at GRS on core samples from the BRIE-site resulted in a gas permeability of roundabout 3 to 6 10^{-20} m². The value from the task description thus appears to represent the lowest value in a possible range of one to two orders of magnitude.

According to the approach concerning the background fractures, two different permeability values were required, one for the undisturbed rock and one for the rock including a network of small background fractures. This network was assumed to increase the matrix permeability in the reference case by one order of magnitude to 10^{-20} m².

---

[4] At Äspö there is in principle the so-called "undisturbed matrix" or "intact rock". It is a common assumption though that fractures exist on all length-scales. In /DER 03/ for instance it is claimed that "The connected porosity in crystalline rock is mainly made up of micro fractures …". This means there are always fractures that are smaller than any reasonably sized volume thus challenging the concept of a REV.

The task description assigned different transmissivity values to the three large determin-istic fractures: $2\cdot10^{-8}$ m²/s for wfracture_01, $2\cdot10^{-9}$ m²/s for wfracture_02, and $6.5\cdot10^{-7}$ m²/s for NNW4. Since the code d³f++ treats fractures as porous media /SCH 12/ the transmissivities had to be converted to equivalent permeabilities which required also fitting fracture apertures. For the sake of simplicity, the transmissivity values were taken as conductivities for fractures with an width of 1 m since standard measurements of the transmissivity had been performed in a packered interval of approximately one metre length /VID 11/. Then conductivity was transformed into permeabilities of $2\cdot10^{-15}$ m², $2\cdot10^{-16}$ m², and $6.5\cdot10^{-14}$ m², respectively.

The effect of background fractures on the rock permeability depends not only on trans-missivity and frequency of the fractures but also on the connectivity. The lower the con-nectivity the less is the impact on the overall rock permeability. An indication for the con-nectivity at the BRIE site on tunnel scale is provided by measurements in the five probing boreholes that were drilled in a row in early 2011. Despite the fact that they were positioned at a distance of just 1.5 m from each other, only the first and the third bore-hole (KO0014G01 and KO0017G01) cut through significantly water bearing fractures. And even these fractures did not appear to be hydraulically connected. Qualitatively, on-ly a limited impact of the background fractures on the rock permeability was thus ex-pected.

The assumed fractures at KO0014G01 and KO0017G01 were square-shaped and had a side length of 1.5 and 2.5 m, respectively. The size was geometrically limited by the condition that they should not cut through the neighbouring boreholes. According to the transmissivity-size relation of fractures at Äspö provided in the task description /BOC 13/ this size falls into the range of the background fractures encountered in the TRUE Block Scale exercise. A transmissivity of approximately 10^{-10} m²/s up to 10^{-9} m²/s can typically be assigned to such fractures. For modeling purposes, this translated into a permeability of 10^{-17} m² up to 10^{-16} m² at an aperture of 1 m. All the model-relevant data are compiled in Tab. 2.1. Derived values are given in italics.

Boundary conditions

Atmospheric pressure was assigned to the surface of the drifts and boreholes. For the conditions on the outer surface of the model, an excel-file with the results of a large-

scale flow simulation at Äspö was provided. The resulting pressure distribution is shown in Fig. 2.6. The excel-file contained also information about dynamic pressure[5], salinity and flow velocity. The data was given as point wise information from the nodes of an ir-regular grid which was then projected bit by bit on the outer model surface by a proce-dure described in /KRO 17b/. The model surface is also shown in Fig. 2.6 including the interception of fractures and boundary faces.

**Tab. 2.1**   Hydraulic properties of the hydraulic features

feature	conductivity [m/s]	permeability [m²]	transmissivity [m²/s]
undisturbed rock matrix	$1 \cdot 10^{-14}$	$1 \cdot 10^{-21}$	
rock matrix including back-ground fractures		$1 \cdot 10^{-20}$	
wfracture_01		$2 \cdot 10^{-15}$	$2 \cdot 10^{-8}$
wfracture_02		$2 \cdot 10^{-16}$	$2 \cdot 10^{-9}$
NNW4		$6.5 \cdot 10^{-14}$	$6.5 \cdot 10^{-7}$
assumed fracture at KO0014G01		$1 \cdot 10^{-17}$	$1 \cdot 10^{-10}$
assumed fracture at KO0017G01		$1 \cdot 10^{-16}$	$1 \cdot 10^{-9}$

The resulting pressure distribution showed a certain trend but was rather erratic on a small scale. The adopted projection procedure apparently introduced some "noise" in the results of the large-scale simulation. Flow simulations based on these boundary condi-tions were expected to show numerical difficulties and unphysical results. An inverse dis-tance weighing procedure for smoothing the dynamic pressure on the boundaries was therefore implemented in the flow code. The effect of this smoothing procedure can be seen in Fig. 2.7.

Note that the pressure distribution of the original simulation accounts apparently only ra-ther loosely for the influence of the open TASD-tunnel and the fractures. Some inaccura-cies concerning the local flow rates at the tunnel opening were therefore expected.

---

[5] the difference between absolute pressure and hydrostatic pressure
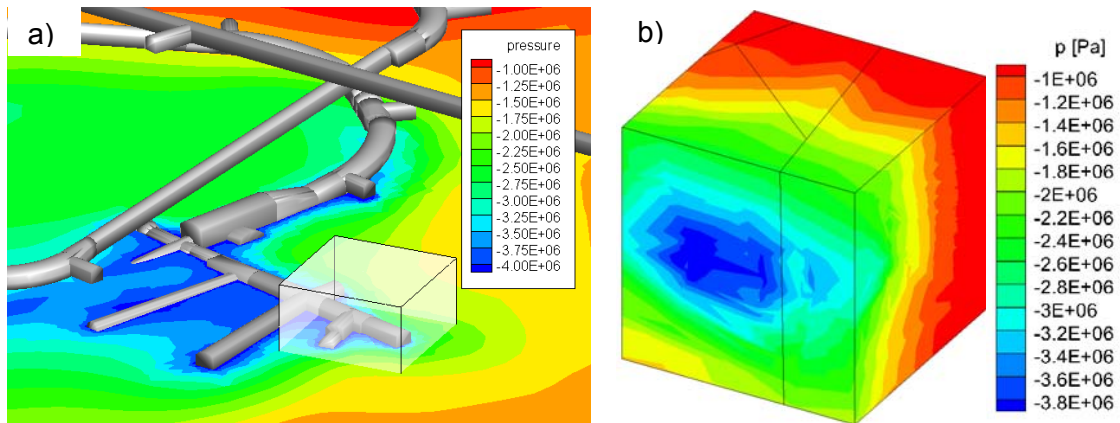
Fig. 2.6   Pressure distribution at the BRIE-site;
a) large-scale model from /BOC 13/, b) projected data (BRIE-site model)
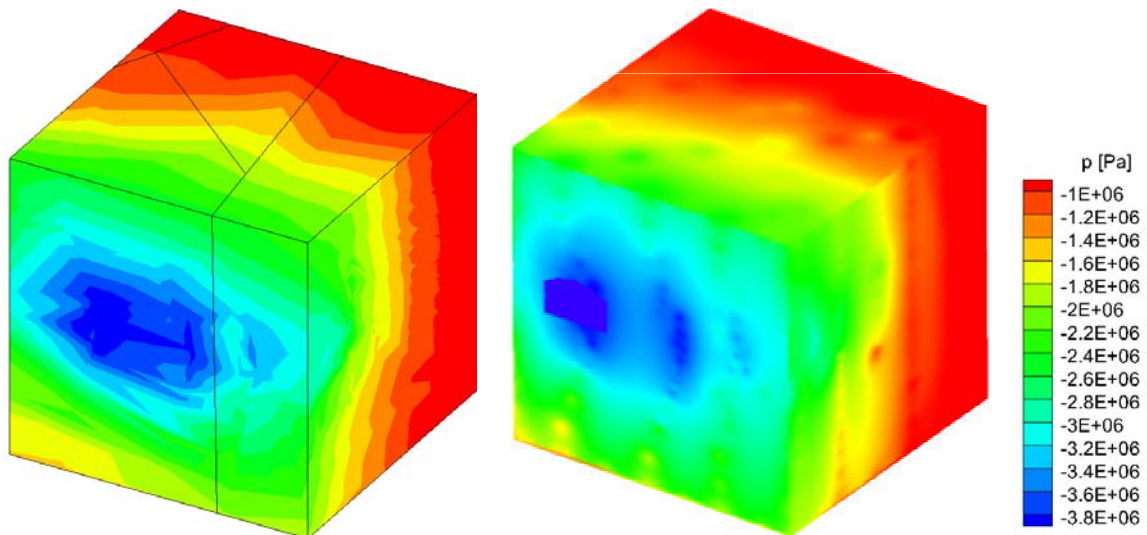
Fig. 2.7   Initial and smoothened pressure distribution on the model boundaries

While there is a noticeable trend in the salinity data provided by the data file, the maximum difference amounts to less than 0.1 % salinity /SCH 12/. In the light of the overall model uncertainties, the effect from the varying density can therefore safely be neglected.

Calibration parameters

In order to fit the outflow rates of the model to the measurements, the quantities listed in Tab. 2.2 were open to be varied within the also in Tab. 2.2 indicated parameter ranges.

Technically, also the aperture of the fractures could be varied but the aperture had simply come into play in the course of transforming transmissivity into permeability. It is thus sufficient to vary just the permeability.

Tab. 2.2   Calibration parameters and possible ranges (where applicable)

quantity	value range
permeability	
undisturbed rock (small box)	10^{-21} to 10^{-19} m²
rock including background fractures	(higher than undisturbed rock)
large deterministic fractures	after /BOC 13/ ± one order of magnitude
assumed fractures	(not used)
boundary conditions	

It was also tried to lower the boundary pressure along the intersections of fractures and model surface. A first try revealed that considerable work in the code would have been required so that the effort was aborted in the end.

Control quantities and data for checking the model

There were two measurement campaigns that could be used for checking the flow model. Both were performed at the probing boreholes. Firstly, the five probing boreholes were packered off below the top metre allowing hydraulic pressure to build up. Even without taking the transient pressure development into account – only steady-state is considered in the model – the maximum pressure build-up can nevertheless be used for comparison. When the boreholes were packered off, the fluid pressure in KO0014G01 and KO0017G01 was measured to reach 0.3 and 0.6 MPa, respectively.

Secondly, the inflow rates into the boreholes after opening one of the packers at a time were also measured. For calibrating the steady-state flow model, only the outflow rates of $1.7 \cdot 10^{-8}$ m³/s and $8.5 \cdot 10^{-9}$ m³/s for boreholes KO0014G01 and KO0017G01, respectively could be used because no outflow could be measured in the other three boreholes. The outflow rates into these three boreholes had been below the detection limit and must therefore have been substantially lower than the rates for KO0014G01 and KO0017G01. The results for pressure build-up and inflow rates are given in Tab. 2.3. Additionally, at the time of Task 8c there was the estimation of the total outflow out of the TASO-tunnel as $1.0 \cdot 10^{-5}$ m³/s /FRA 12a/.

Tab. 2.3 Maximum pressures and outflow rates in the probing boreholes; ◻from /BOC 13/[6]

	KO0020G01	KO0018G01	KO0017G01	KO0015G01	KO0014G01
Inflow, Q Built-up pressure, P	Yes, but below the measurement limit	No	Yes $Q \approx$ 0.5 ml / min $P \approx$ 6 bar	No	Yes $Q \approx$ 1 ml / min $P \approx$ 3 bar

Calibration strategy

At first, the model described in the previous sections was set up as a reference case – also called case A in the following. After checking the output of the model against measured data (control quantities), variants called cases B, C, D, and E were defined to adjust the input of the model (calibration parameters) varying the reference values preferably within the ranges given in Tab. 2.2. The target values of the control quantities were considered to be matched if the deviation between the measured and calculated values amounted to less than a factor of five. These variations of the reference case provided also some information about the sensitivity of the model to the specified changes. The last case includes the final set of hydraulic parameters and thus represents the hydraulic model for Task 8c.

Results

Case A: Reference case

Pressure is generally decreasing from the outer model surface (surface of the cubic domain) towards the tunnels and boreholes. This is exemplarily shown in Fig. 2.8 for the vertical cross-section through the TASO-tunnel. Rather little influence is exerted by wfracture_01 on the pressure field in the vicinity of borehole KO0014G01. A comparison of Fig. 2.8 a) and Fig. 2.8 b) reveals that opening the boreholes has only an influence in the immediate vicinity of the boreholes. Also observable in the borehole field is a slight trend to less pressure along the TASO-tunnel towards the TASD-tunnel (to the right in

---

[6] The flow rates for KO0017G01 and KO0014G01 are equal to 8.3 10^{-9} m³/s and 1.7 10^{-8} m³/s, respectively.

Fig. 2.8). Taking the maximum pressure in a borehole to be the measured pressure in the test, the model gives 6.3 bar for KO0014G01 and 7.7 bar for KO0017G01 which relates loosely to the measured values of 3 bar for KO0014G01and 6 bar for KO0017G01.
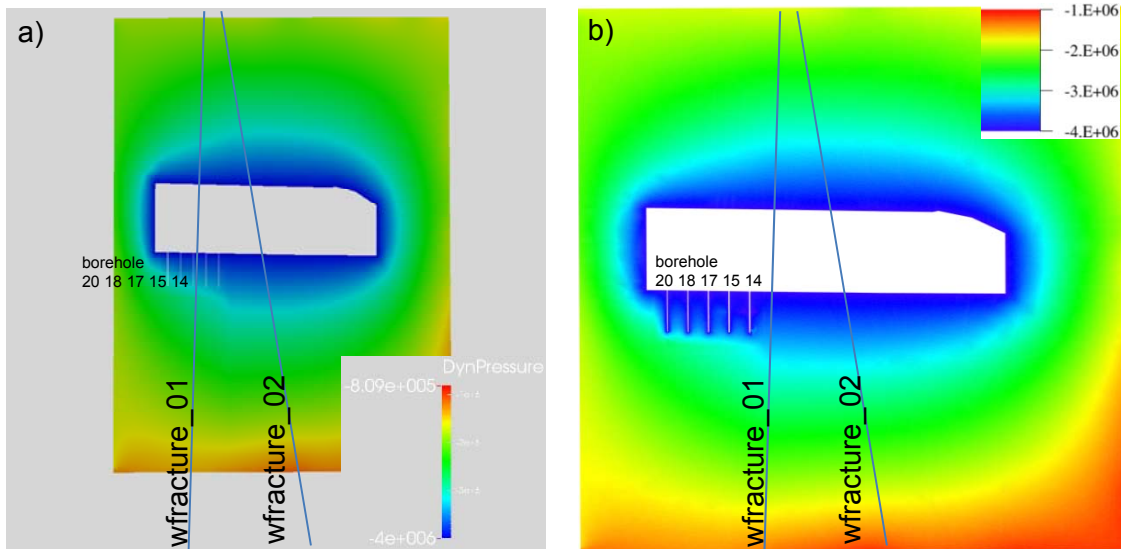
Fig. 2.8   Dynamic pressure in a vertical cross-section through the TASO-tunnel;
a) all boreholes closed (reference case), b) all boreholes open

Flow rates out of the rock into the probing boreholes as well as into the TASO-tunnel were also calculated. They are compiled as well as the results from the other cases in Tab. 2.4.

Total flow through the whole tunnel surface in the model exceeds the estimated total outflow of 10^{-5} m³/s /FRA 12a/ only by 40 %. Additionally, outflow from the two fractures and outflow over the remaining tunnel surface were distinguished in the model results. From this data it became clear that total outflow into the tunnel is dominated by w_fracture_01 for case A as well as for all other cases.

An outflow value of 5.0 10^{-11} m³/s, chosen as an ad-hoc criterion for unobservable outflow into the boreholes, was nowhere nearly exceeded.

Case B: Only borehole KO0014G01 opened

Opening borehole KO0014G01 in the reference case showed clearly that the permeability values adopted for the matrix were far too low. The target value was missed by a factor of about 2000. Flow from the fractures and over the tunnel surface proved to be virtually insensitive to opening the borehole. Note that all changes in the boundary conditions and the permeability values referring to case A are indicated in Tab. 2.4.

Case C: Borehole KO0014G01 opened and increase of permeability in the matrix

For case C it was assumed that a network of background fractures would increase the matrix permeability by three orders of magnitude. This increased outflow into borehole KO0014G01 by two orders of magnitude and brought the resulting value of $1.0 \ 10^{-9} \ m^3/s$ almost in an acceptable range.

Case D: Increasing the permeability in the box and the assumed fractures

The increase in outflow rate for borehole KO0014G01 had not been proportional to the increase in matrix permeability as case C had shown. Therefore, the permeability of the box that was supposed to represent the undisturbed matrix adjacent to the boreholes was increased. As this proved not to be sufficient yet, the permeability for the assumed fracture at KO0014G01 was increased also. The resulting model showed a permeability contrast between the matrix and the box of two orders of magnitude that provided a satisfying contrast in the outflow rates between the high and low water producing boreholes, KO0014G01 and KO0017G01 on the one hand and KO0015G01, KO0018G01, and KO0020G01 on the other hand. The assumed permeability of the fractures in the box needed indeed to be higher than the matrix permeability in order to attract a sufficient amount of water to KO0014G01 and KO0017G01. The calculated outflow rate for KO0014G01 lay eventually by less than a factor of 5 off the target value.

Case E: Final model – all boreholes successively just opened once

With the permeability set derived for case D outflow rates for all five probing boreholes were checked. As Tab. 2.4 shows all flow rates were reproduced within the adopted un-

certainty of a factor of 5. The calculated values deviated by factors of 0.24, 1.04 and 1.6 from the measurements for KO0014G01, KO0017G01 and the tunnel, respectively.

The contrast of flow rates for KO0014G01 and KO0017G01 in comparison to the rates for the other boreholes showed that the assumed fractures contributed substantially to the outflow. However, the calculated values for KO0018G01 and KO0020G01 were high and disturbingly. This reflects a related increase of the pressure gradients along the TASO-tunnel towards its end which is consistent with the pressure distribution discussed above.

Note that variations in the permeability of the three large fractures resulted in significant changes of outflow rates only in these fractures. The rest of the flow system remained largely unaffected by such changes.

Discussion of the final model (case E)

The flow model for Task 8c was able to reproduce the trend of a pressure decrease along the TASO-tunnel towards the TASD-tunnel which had been observed in the series of five probing boreholes

The calculated flow rates for all boreholes lay within a factor of 4 of the measured values. Parameter variations confirmed that inflow rates are mainly depending on matrix permeability and on additional water-bearing fractures that were opened by these boreholes. The large deterministic fractures wfracture_01, wfracture_02 and NNW4 had apparently little influence on these flow rates.

However, boreholes KO0018G01 and KO0020G01 were producing too much water when opened in the model. This is because these boreholes reach deeper into the zone of higher pressures around the tunnel. Therefore these boreholes attract more water than those which are almost totally located in the low pressure zone created by the tunnel. It is not clear if this has to do with the location of the model boundary that lies rather close to the end of the TASO-tunnel or with the heterogeneities introduced by the network of background fractures. Note that the borehole field generally lowers the pressure within its perimeter.

Tab. 2.4   Input parameters and calculated flow rates for the cases A to E

case	property	rock	small box	fractures					boreholes					TASO tunnel	
				wf_01	wf_02	NW4	ass.fr. KO 14	ass.fr. KO 17	KG14	KG15	KG17	KG18	KG20	surface	total
meas.	Q_t [m³/s]								$1.7\ 10^{-8}$	-	$8.3\ 10^{-9}$	-	-	-	10^{-5} [7]
A	k [m²] / b.c. bore.h.	10^{-20}	10^{-21}	$2\ 10^{-15}$	$2\ 10^{-16}$	$2\ 10^{-14}$	10^{-17}	10^{-17}	closed [8]	closed	closed	closed	closed		
	Q_c [m³/s]			$1.4\ 10^{-5}$	$9.0\ 10^{-7}$		$2.7\ 10^{-14}$	$6.8\ 10^{-14}$	$8.1\ 10^{-14}$	$6.9\ 10^{-14}$	$1.6\ 10^{-13}$	$2.1\ 10^{-13}$	$1.4\ 10^{-13}$	$9.3\ 10^{-10}$	$1.4\ 10^{-5}$
B	b.c. bore.h.								**open**	closed	closed	closed	closed		
	Q_c [m³/s]			$1.4\ 10^{-5}$	$9.0\ 10^{-7}$		$7.6\ 10^{-12}$	$8.2\ 10^{-14}$	$8.4\ 10^{-12}$	$1.1\ 10^{-13}$	$1.7\ 10^{-13}$	$2.1\ 10^{-13}$	$1.4\ 10^{-13}$	$9.2\ 10^{-10}$	$1.4\ 10^{-5}$
C	k [m²] / b.c. bore.h.	10^{-17}							**open**	closed	closed	closed	closed		
	Q_c [m³/s]			$1.4\ 10^{-5}$	$9.3\ 10^{-7}$		$1.0\ 10^{-9}$	$3.3\ 10^{-11}$	$1.0\ 10^{-9}$	$8.8\ 10^{-14}$	$3.3\ 10^{-11}$	$2.2\ 10^{-13}$	$1.4\ 10^{-13}$	$9.3\ 10^{-7}$	$1.6\ 10^{-5}$
D	k [m²] / b.c. bore.h.	10^{-17}	10^{-19}				10^{-16}		**open**	closed	closed	closed	closed		
	Q_c [m³/s]			$1.4\ 10^{-5}$	$9.3\ 10^{-7}$		$4.0\ 10^{-9}$	$3.5\ 10^{-11}$	$4.0\ 10^{-9}$	$1.0\ 10^{-11}$	$4.4\ 10^{-11}$	$2.2\ 10^{-11}$	$1.4\ 10^{-11}$	$9.3\ 10^{-7}$	$1.6\ 10^{-5}$
E	k [m²] / b.c. bore.h.	10^{-17}	10^{-20}				10^{-16}		**open** [9]	**open** [9]	**open** [9]	**open** [9]	**open** [9]		
	Q_c [m³/s]			$1.4\ 10^{-5}$	$9.3\ 10^{-7}$				$4.0\ 10^{-9}$	$1.5\ 10^{-11}$	$8.6\ 10^{-9}$	$2.3\ 10^{-11}$	$2.5\ 10^{-11}$	$9.3\ 10^{-7}$	$1.6\ 10^{-5}$

colour coding

open borehole: 1/5 * target value < calculated value < 5 * target value
closed borehole: calculated value < $5.0\ 10^{-11}$; ad-hoc criterion for unobservable outflow
open borehole: calculated value < 1/5 * target value   or   calculated value > 5 * target value
closed borehole: calculated value > $5.0\ 10^{-11}$; ad-hoc criterion for unobservable outflow

---

[7] This data refers to the estimations that were valid at the time of calculation.

[8] no-flow boundary condition at the borehole wall; given values indicate the precision of the flow calculation as it should read 0

[9] there were five models for case E in each of which just one borehole was opened; the data from the closed boreholes are not given

Parameter variations indicated an effective permeability of the rock matrix including background fractures of about 10^{-17} m². This value is surprisingly high in comparison to the values of 10^{-21} to 10^{-19} m² for the undisturbed matrix. It suggests on a larger scale a somewhat homogeneous fracture network consisting of rather well-connected smaller fractures.

Flow into the tunnel was dominated by outflow from wfracture_01. Outflow from wfracture_02 and the tunnel surface contributed less than 10 % each to the total outflow.

From the measured outflow rates into the probing boreholes can be concluded, though, that the flow field is very inhomogeneous on the scale of these boreholes. Larger local background fractures provide apparently inflow for some of the probing boreholes. Connectivity of the larger background fractures is thereby rather low since there is little if no hydraulic connection between the five probing boreholes despite the fact that they are located only 1.5 m apart from each other.

The source of the outflowing water is therefore not quite clear. A hydraulic connection by a few background fractures to one of the strongly water conducting large deterministic fractures is as likely as a connection of just one fracture to a better connected network of smaller fractures that are more homogeneously distributed in the matrix. Considering the low connectivity of the larger background fractures it is quite probable that the water producing boreholes KO0014G01 and KO0017G01 are drawing the water from different sources.

2.2.2   Task 8d

Model geometry

By and large, a similar approach for the flow model was used for Task 8d as for Tasks 8b and 8c. Slight variations were due to additional probing boreholes that had been drilled in the meantime and to the widening of the designated test boreholes to a diameter of 30 cm. Additional to the five probing boreholes considered in Task 8c, fourteen vertical and four horizontal observation boreholes had been drilled before the beginning

of Task 8d. Locations of these boreholes are depicted in Fig. 2.9 and Fig. 2.10, respectively. The diameter of the test boreholes KO0017G01 and KO0018G01 had been increased to 30 cm.
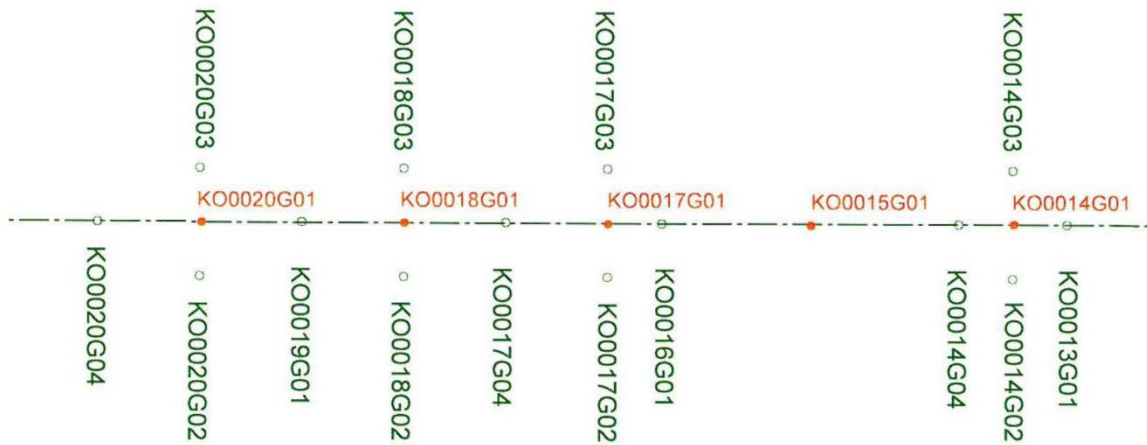
Fig. 2.9   Location of the vertical boreholes in the TASO-tunnel; from /BOC 13/
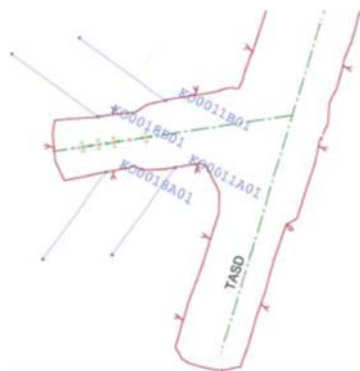
Fig. 2.10   Location of the horizontal boreholes in the TASO-tunnel; from /BOC 13/

The most important change, though, concerned the connection of the background fractures to the geotechnical openings. In Task 8c two artificial fractures had been introduced to mimic the connection of the boreholes with the stochastic background fracture network. This is not a method to be applied in general, though, as it requires an extremely detailed knowledge about size and location of the fractures intersecting drifts and boreholes. The approach applied here had only chances of success because the inflow rates into the boreholes had been measured and the boreholes had been inspected with a view to size and location of fractures.

For a long time it had been observed that a reduction of outflow from the rock is apparently caused by a narrow zone of reduced permeability adjacent to geotechnical openings (e.g. /OLS 92/, /KUL 02/). A skin-like zone ('skin') around all geotechnical openings was therefore adopted for the flow model in Task 8d. Except for the three large fractures no smaller fractures were considered to cut through the skin. The effect of the small intersecting fractures was assumed to be averaged over the surface of the skin. While losing accuracy with respect to local flow features, the approach allowed for a quick application to the complete ensemble of geotechnical openings. Note that the physical reason for the observed skin-effect has not been determined yet.

The flow model for Task 8d encompassed 23 boreholes. Taking the skin effect into account the model contained the following structural elements:

– matrix including background fractures

– tunnel skin

– borehole skin

– large fractures (wfracture_01, wfracture_02, NNW4)

– large fractures within tunnel/borehole skin

Shown in Fig. 2.11 is a part of the model where the skin around the TASD-tunnel is partly removed and around the TASO-tunnel even totally omitted. Also not depicted are the borehole skins outside the tunnel skins.

Hydraulic properties

New laboratory tests on de-stressed matrix core samples showed a range of permeability values between $6 \cdot 10^{-21}$ m² and $9 \cdot 10^{-20}$ m² /BOC 13/ which appeared to be very much in line with the data for Task 8c. However, as the calibration exercise for Task 8c had shown, the effective permeability including the influence of the background fractures was apparently much higher. The value of 10^{-17} m² derived for Task 8c was also adopted for Task 8d.

Hydraulic tests in borehole KO0011A01 provided a somewhat reduced transmissivity value of $4 \cdot 10^{-16}$ m²/s for wfracture_01 in comparison to the value from Task 8c. Where the fractures lay within a skin zone, fracture permeability was generally reduced by one order of magnitude in comparison to the measured data.
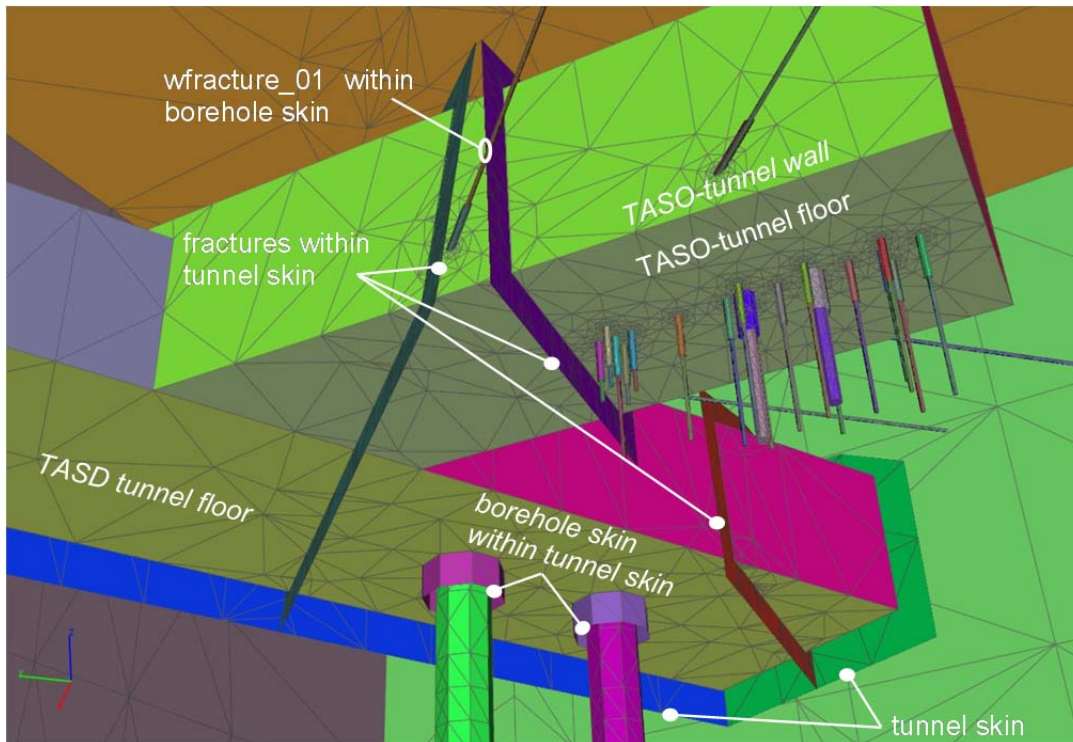
Fig. 2.11 Look from below at the BRIE-model for Task 8d

The permeability of the tunnel skin was assumed to be 10^{-18} m². That is one order of magnitude lower than the matrix permeability. For the assignment of permeability values for the borehole skins, the boreholes were divided into two groups according to the preliminary outflow rates indicated in Fig. 2.12. The skin permeability for all boreholes with an outflow rate above 0.1 ml/min was chosen to be 10^{-19} m², while a value of 10^{-20} m² was assigned to boreholes with an outflow rate below 0.1 ml/min. These values are generally lower than the permeability of the tunnel skin since it was expected that a zone of degassed bubbles would be more localised around a borehole than around the tunnel because of stronger converging streamlines. Thus flow should be impeded more effectively at small boreholes than at larger openings. The assignment of permeabilities to the structural elements of the model in the reference case is summarised in Tab. 2.5.

Interference (drilling) and preliminary inflows (2011-09-14/21)
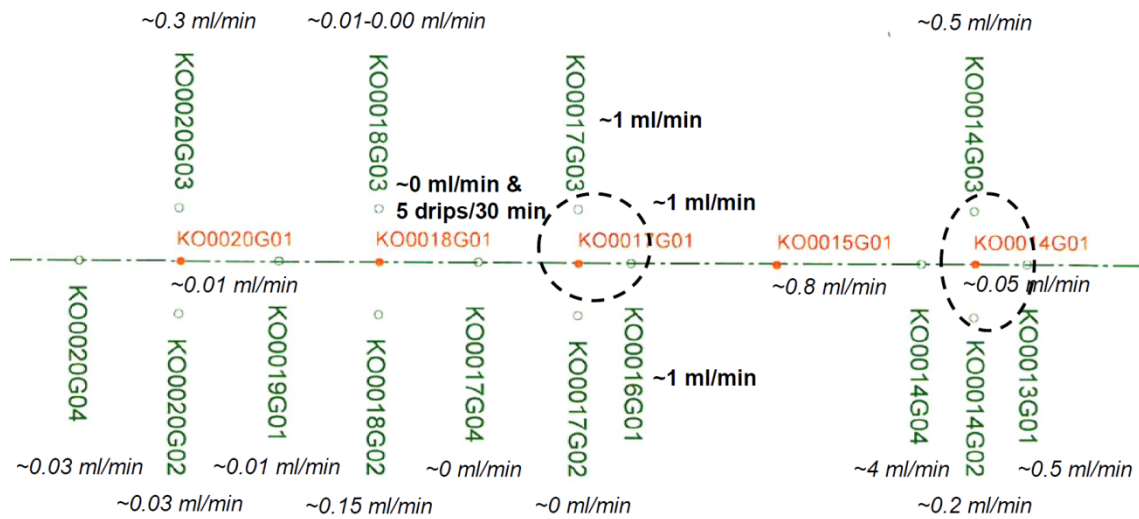
Fig. 2.12   Preliminary outflow data for the vertical boreholes; from /FRA 12b/

Tab. 2.5   Assignment of permeabilities to hydraulic structures; reference case

structure	permeability [m²]
matrix including background fractures	10^{-17}
wfracture_01, wfracture_02, NNW4	$4 \cdot 10^{-16}$, $2 \cdot 10^{-16}$, $6.5 \cdot 10^{-15}$
tunnel skin	10^{-18}
wfracture_01 within tunnel skin	$4 \cdot 10^{-17}$
wfracture_01 within borehole skin	$4 \cdot 10^{-17}$
wfracture_02 within tunnel skin	$2 \cdot 10^{-17}$
Skin for boreholes KO0013G01 KO0014G02, KO0014G03, KO0014G04 KO0015G01,KO0016G01 KO0017G01, KO0017G03 KO0018G02, KO0020G03	10^{-19}
KO0014G01, KO0017G02, KO0017G04 KO0018G01, KO0018G03 KO0019G01 KO0020G01, KO0020G02, KO0020G04	10^{-20}

Calibration parameters

In order to fit the outflow rates of the model to the measurements, some of the quantities listed in Tab. 2.6 were varied. The table also provides indications for possible parameter ranges.

Tab. 2.6   Permeability values and possible ranges for the Task-8d model

hydraulic structure	permeability range
matrix	10^{-17} m² ± one order of magnitude
tunnel skin	less than matrix permeability
borehole skin	less than matrix permeability
wfracture_01	$4 \cdot 10^{-16}$ m² ± one order of magnitude
wfracture_02	$2 \cdot 10^{-16}$ m² ± one order of magnitude
NNW4	$6.5 \cdot 10^{-15}$ m² ± one order of magnitude
wfracture_01 within tunnel skin	between 1 and 1/100 of fracture permeability
wfracture_02 within tunnel skin	between 1 and 1/100 of fracture permeability
wfracture_01 within borehole skin	between 1 and 1/100 of fracture permeability

Control quantities and data for checking the model

There had been several campaigns to measure outflow into the boreholes:

− 2010 (campaign A):

   short-term measurements after drilling the first five boreholes for all five boreholes

− 2010 (campaign B):

   a 400 minute test of inflow into KO0017G01

− 2011 (campaign C):

   short-term measurements (15 min) after drilling 18 additional observation boreholes

− 2012 (campaign D):

   investigation of outflow distribution into KO0017G01 after

   • widening and deepening of KO0017G01

   • widening of KO0018G01

The task description concentrated on data for the first five probing boreholes which is summarized in Tab. 2.7. The data varied from campaign to campaign and thus seemed to indicate a certain change in the flow system. The pronounced short-term transient behavior of the outflow rates as depicted in Fig. 2.13 for KO0017G01 and for KO0011A01 suggested that short-term tests overestimated the steady-state flow rate. The two columns furthest to the right in Tab. 2.7 contain the outflow values against which the flow model has been calibrated. They are actually based on some scientific guesswork because they are especially uncertain if one campaign provided no flux above the detection limit.

Tab. 2.7   Outflow rates at different times

| borehole | outflow in [ml/min] from campaign | | | | adopted | |
	A	B	C	D	[ml/min]	[m³/s]
KO0014G01	1.0	-	0.1	-	0.30	5.00 10^{-09}
KO0015G01	0	-	0.6	-	0.15	2.50 10^{-09}
KO0017G01	0.5	0.25	1.0	0.12 – 0.25	0.25	4.17 10^{-09}
KO0018G01	0	-	0	0.01 – 0.03	0.02	3.33 10^{-10}
KO0020G01	0	-	0.01	-	0.01	1.67 10^{-10}
KO0011A01[10]	-	-	0.1	-	0.10	1.67 10^{-09}
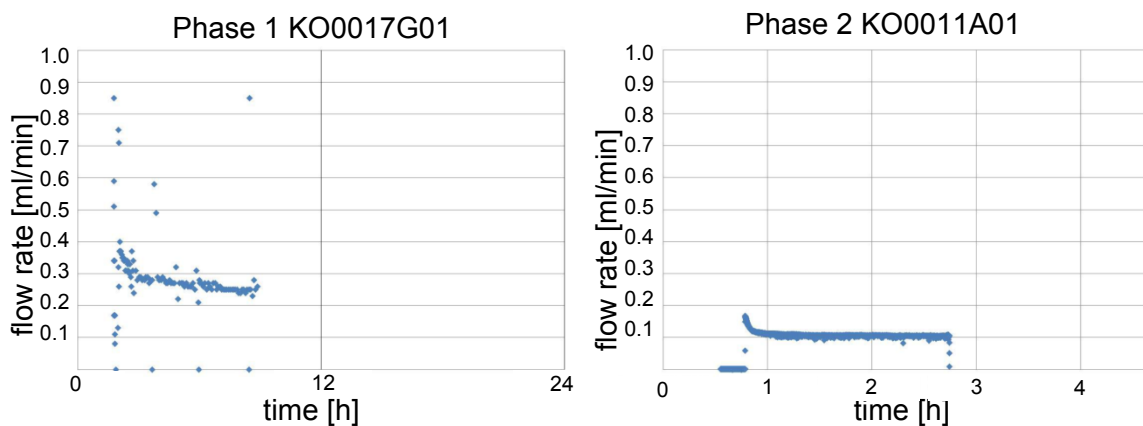
Fig. 2.13   Outflow rates for KO0017G01 and for KO0011A01; from /BOC 13/

Note that the adopted flow rates were in contradiction to the trend of increasing pressure gradients towards the end of the TASO-tunnel. Since model geometry and boundary conditions are basically the same as for Task 8c the same contradiction was expected for the Task 8d model. However, the preliminary flow data for all vertical boreholes summarised in Fig. 2.12 indicated that the flow rates can change from borehole to borehole by two orders of magnitude if an outflow rate could be measured at all (e.g. KO0014G01 and KO0014G04 or KO0017G01 and KO0017G02). A rather high inhomogeneity in the permeability appears to be introduced by water conducting background fractures. The adopted flow rates for calibration were therefore considered to be more a guideline than an absolute target.

New data from the test with sorbing mats provided an estimation for the outflow into the TASO-tunnel of only 1.7 ml/s for Task 8d /BOC 13/. While it is not explicitly mentioned in

---

[10]   Filed under campaign C because it was performed at the same time as the other tests of this campaign. In contrast to the other tests, however, this particular test lasted about 120 min.

the task description, it is assumed from the data of the test that this value does not account for outflow from the large deterministic fractures.

Water pressure in the packered-off boreholes cannot be simulated with the model described here. A qualitative assessment by looking at the calculated pressure field was performed, though. Basis was the data summarized in Tab. 2.8. In the Task description it was asked to "use primarily KO0017G01 and boreholes in wall (11A01, 11B01, 18A01, 18B01)" as calibration targets.

Tab. 2.8   Pressure measured in the packered-off boreholes; after /BOC 13/

borehole	orientation	section [m]	pressure [bar]
KO0015G01	vertical	2.1-3-03	5
KO0017G01	vertical	2.11-2.97	5
KO0018G01	vertical	1.42-3.06	4
KO0020G04	vertical	2.0-3.5	10.5
KO0020G03	vertical	2.0-3.5	9
KO0011A01	horizontal	1.01-10	27
KO0011B01	horizontal	1.24-10	3
KO0018A01	horizontal	1.11-10	26
KO0018B01	horizontal	1.28-10	21

Calibration strategy

Modelling groundwater flow for Task 8d started out again with a reference case which was then supposed to be adjusted in order to match the calibration targets. As it turned out, though, the resulting match was not bad from the beginning on. The remaining discrepancies could not be resolved so that the reference case became the final flow model for Task 8d. For the reference case, the following models were set up:

−   model A: all boreholes closed
−   models B to G: just one of the following boreholes open: KO0014G01, KO0015G01, KO0017G01, KO0018G01, KO0020G01, and KO0011A01
−   model H: only both test boreholes KO0017G01 and KO0018G01 open

General observations from the results

The trend of decreasing pressure from the model boundary towards the geotechnical openings is not surprisingly also found in the flow model for Task 8d as shown in the two cross-sections in Fig. 2.14. In graph a) the traces of wfracture_01 and wfracture_02 are noticeable. Graph b) demonstrates the effect of the skin zone around the TASO-tunnel if compared to the analogous cross-section in Fig. 2.8 a). Clearly recognizable is the shift of the high pressure zone towards the geotechnical openings. This occurs because in comparison to a model without skin the pressure gradient within the skin increases while it decreases outside the skin.

a)   b)
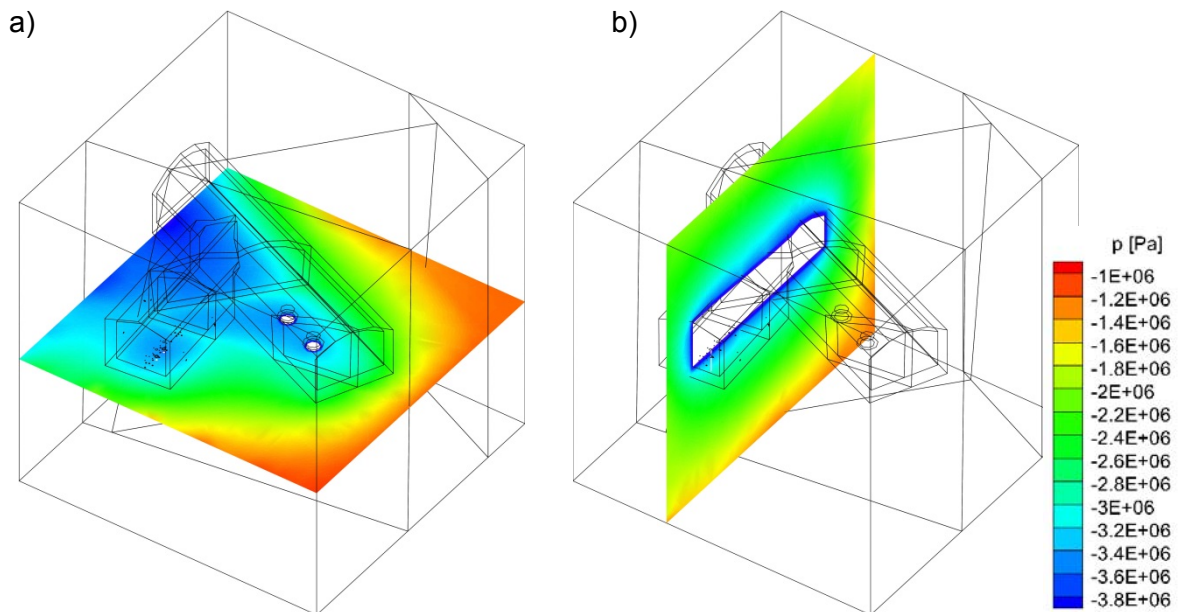
Fig. 2.14   Pressure distribution in two cross-sections;
  a) horizontal cross-section 1 m below tunnel floor,
  b) vertical cross-section through some of the boreholes

The influence of the skin around the boreholes on the pressure field is rather little, though, as Fig. 2.15 shows. Plot a) depicts the dynamic pressure when all boreholes are closed while plot b) shows the pressure field if only KO0017G01 is opened. The most prominent difference between plots a) and b) is the very low pressure zone tightly enveloping the borehole. Otherwise, the differences appear to be marginal even if shown in a different scale as in plots c) and d).
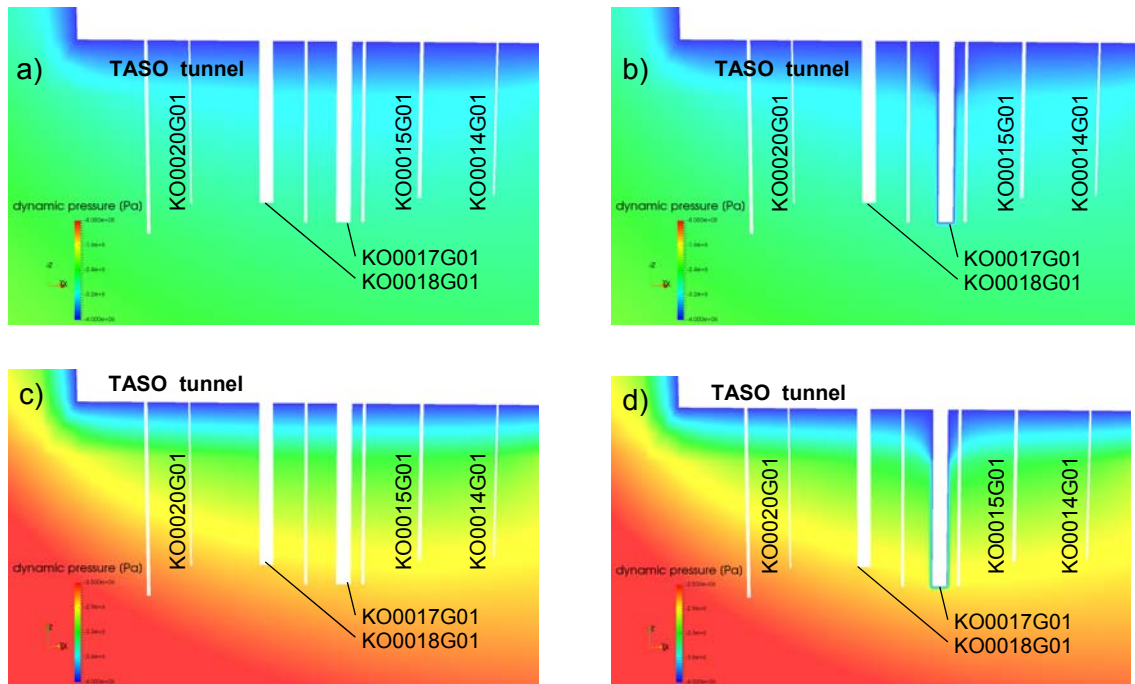
Fig. 2.15   Pressure in a vertical cross-section through some of the boreholes;
a) all boreholes closed, b) only KO0017G01 open,
c) and d) like a) and b) with different scales

Plots c) and d) in Fig. 2.15 show clearly, that the vertical pressure gradient from the tunnel floor into the rock increases along the TASO-tunnel towards the tunnel face. Since the boreholes have roughly the same length they reach therefore deeper into the field of increasing pressure the closer they are located to the tunnel face. The model thus predicts a tendency of higher outflow rates from open boreholes and higher pressure in closed boreholes towards the end of the tunnel.

The composite view of the pressure field and the resulting flow in Fig. 2.16 shows nicely the water-drawing effect of borehole KO0017G01 in the TASO-tunnel and of the boreholes for the TBT and the CRT in the TASD-tunnel. Additionally, water flow from the fractures into the matrix in the range of the tunnel system can be observed. Outside this range, the effect of the fractures appears to be very limited.
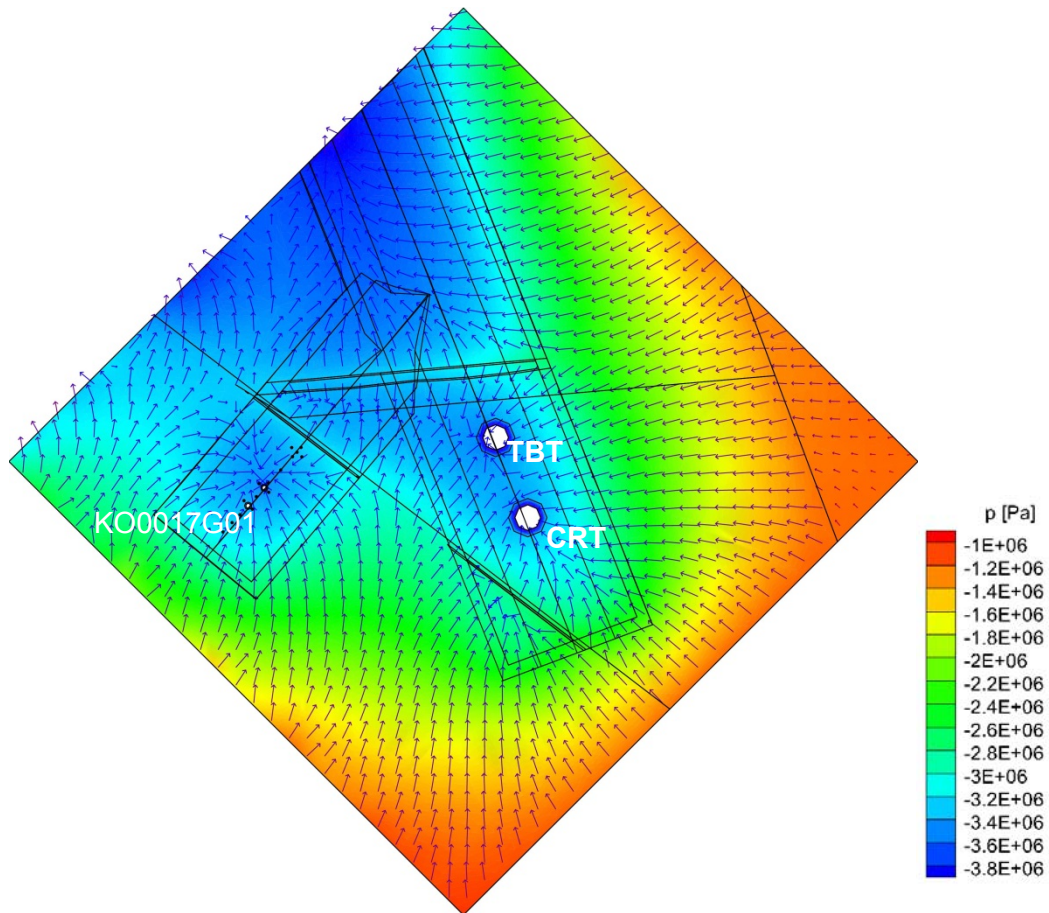
Fig. 2.16   Velocity and pressure in a horizontal cross-section 1 m below tunnel floor

Introducing a low permeable skin around an open structure like a tunnel or a borehole means a higher resistance to outflow into the referring structure. Water migrating towards this structure could therefore be diverted along hydraulically easier ways to nearby boreholes and fractures. The hydraulic effect of introducing a skin at a structure on other structures depends on permeability and structure geometry. This has been tentatively tested with the model by switching skin zones on and off. The results are graphically summarized in Tab. 2.9. While the most system responses are as expected, it is noteworthy that the effect of any skin is hardly observable in the fractures because of the rather high flow rates.

Tab. 2.9 Effect of permeability reduction on outflow

outflow via	tunnel surface	fractures	boreholes
perm. reduction in the			
tunnel skin	↘ (red)	▬	↗ (green)
fractures in tunnel skin	↗ (green)	↘ (red)	↗ (green)
borehole skins	↘ (red)	▬	↗ (green)

Specific results for the reference case / final model for Task 8d

The calculated flow rates from models A to H are compiled in Tab. 2.10. Outflow into the boreholes was generally rather too high than too low in the model. In contrast, outflow into the TASO-tunnel was too low. Any decrease of flow in the matrix that would have adjusted flow into the boreholes would also have decreased flow into the tunnel. As the outflow value for the tunnel was an estimate and the flow regimes in the borehole field were highly inhomogeneous, no sense was seen in further adjustments of the permeabilities. The reference model thus represents already the final flow model for Task 8d.

Tab. 2.10 Comparison of outflow rates for the reference case; values in [m³/s]

	boreholes KO14	KO15	KO17	KO18	KO20	KO11	TASO-tunnel
measured	5.00E-09	2.50E-09	4.17E-09	3.33E-10	1.67E-10	1.67E-09	1.67E-06
model A							5.47E-07
model B	1.59E-09						5.46E-07
model C		2.15E-09					5.46E-07
model D			3.99E-09				5.45E-07
model E				2.73E-09			5.45E-07
model F					1.70E-09		5.46E-07
model G						4.32E-08	5.42E-07
model H			2.62E-09	2.62E-09			5.43E-07

    value lower than 0.2 times the measurement
    value higher than 5 times the measurement

Outflow from the tunnel surface was generally one third of the estimated value and can thus be considered to have been matched. Hardly any influence of open boreholes on the outflow from the tunnel surface can be noticed.

In model H both test boreholes were opened. A comparison of the outflow rates with those of models D and E shows that the flow rate is only moderately affected by opening a neighbouring borehole.

The calculated outflow for boreholes KO0014G01, KO0015G01, and KO0017G01 is matching the measured values. But it is too high for the two last vertical boreholes toward the end of the TASO-tunnel (KO0018G01 and KO0020G01). Increase of outflow toward the end of the TASO-tunnel is consistent with the pressure distribution in Fig. 2.15 around the TASO-tunnel as discussed in the previous subsection. Since the measured outflow in these two boreholes actually decreases towards the end of the tunnel, flow must be strongly influenced by local inhomogeneities caused by fractures.

The calculated outflow rate from the horizontal borehole KO0011A01 is also too high, obviously a consequence of the immediate connection of the borehole with wfracture_01. While Fig. 2.17 shows that a slight shift in the location of wfracture_01 would avoid a direct contact with KO0011A01, the task description states expressively that hydraulic tests had been performed in the fracture from this borehole. The reason for this massive discrepancy between measured and calculated outflow rate is therefore unclear which is quite unsatisfactory in the light of the comparatively well matched other data.
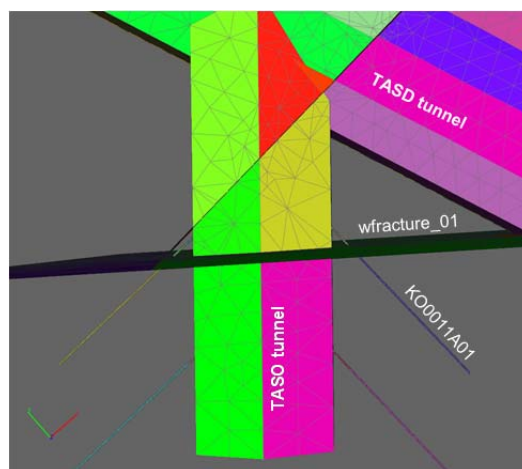
Fig. 2.17   View on the BRIE-model from above

The model without any open borehole formed the basis for the comparison of measured and calculated hydraulic pressure. For this comparison it was assumed that the highest pressure found in the packered test interval (cp. Tab. 2.8) would reflect the measured pressure. The data were retrieved with the help of a visualization tool from a view as depicted in Fig. 2.18 and are compiled in Tab. 2.11.

Tab. 2.11   Measured and calculated hydraulic pressure in the boreholes

borehole	orientation	pressure [bar]	
		measured	calculated
KO0015G01	vertical	5	11.2
KO0017G01	vertical	5	11.6
KO0018G01	vertical	4	12
KO0020G04	vertical	10.5	14.5
KO0020G03	vertical	9	13
KO0011A01	horizontal	27	17
KO0011B01	horizontal	3	9
KO0018A01	horizontal	26	24
KO0018B01	horizontal	21	13

value higher than 2 times the measurement
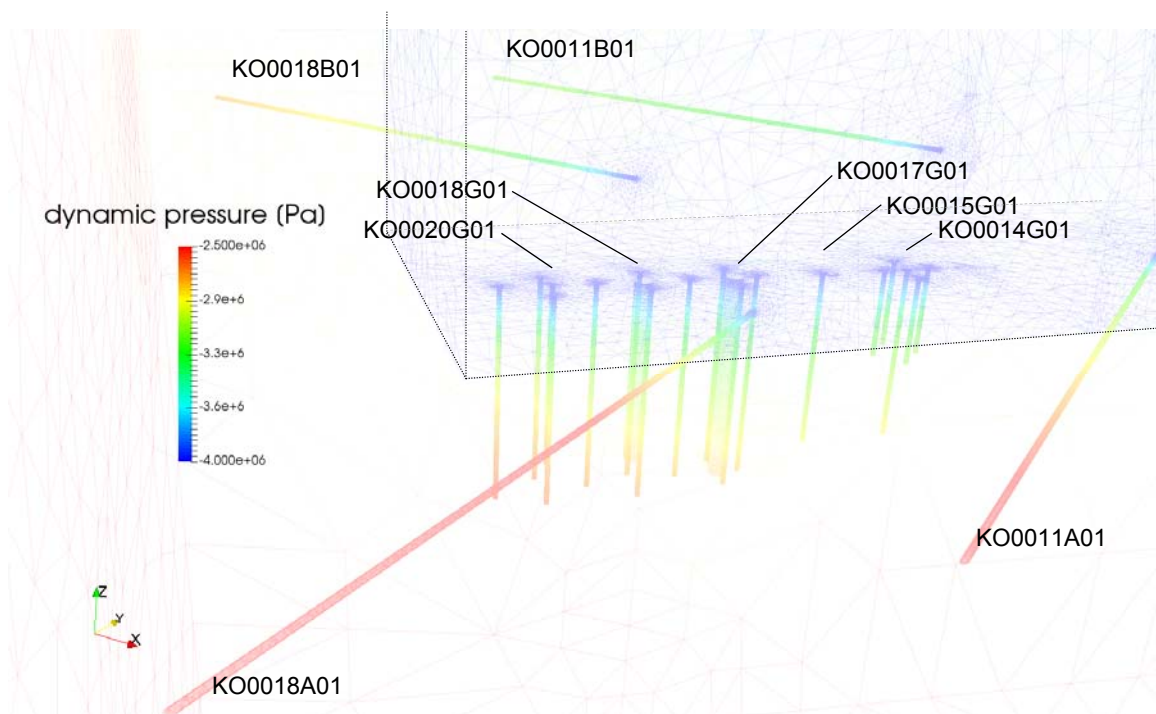
Fig. 2.18   Pressure at the surface of the boreholes

The calculated pressure in the vertical boreholes is generally higher than the measured pressures while the pressure in the horizontal boreholes is underestimated by the model except for KO0011B01. However, in all cases the calculated value is not off by more than a factor of 3.

By and large, the pressure in the horizontal boreholes is higher than in the vertical boreholes as these boreholes reach deeper into the areas where high pressures prevail. The value of 3 bar for KO0011B01, however, appears to be strange in in the light of the 21 to 27 bar for the other horizontal boreholes. It strongly suggests a wrong assumption concerning the size of wfracture_02. As the model layout depicted in Fig. 2.19 indicates, KO0011B01 is almost parallel to wfracture_02. If the fracture was not ending right at wfracture_01 but would extend a few metres beyond this intersection, KO0011B01 would be very closely aligned to wfracture_02 over the whole length. Since wfracture_02 is hydraulically highly conductive the pressure in the vicinity of this fracture would be quite low which would account for a rather low pressure in the packered borehole KO0011B01. Unfortunately, this was realized only after the model had already been set up so there was no possibility to check this hypothesis with the help of model variations.
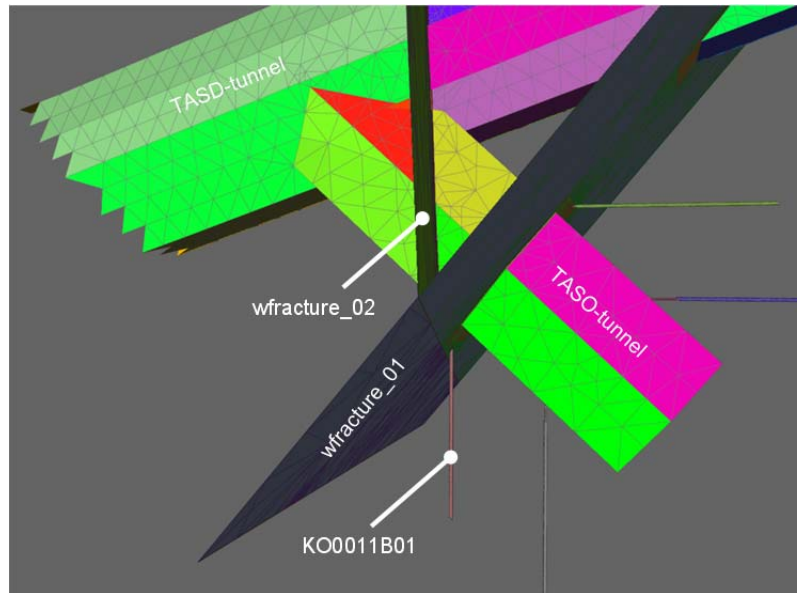
Fig. 2.19   Look from above at wfracture_02 and borehole KO0011B01

Discussion

The following items had changed in the flow model from Task 8c to Task 8d:

− Additional probing boreholes had been drilled.

− There were more outflow and pressure measurements available.

− Conceptionally, the direct modelling of assumed fractures to account for the locally varying outflow from borehole to borehole had been dropped in favour of a low permeable skin at tunnel and borehole walls which was believed to be a more general approach.

Pressure data from the horizontal borehole KO0011B01 suggested a larger extension of wfracture_02 than prescribed in the task description. Unfortunately, this had been realised too late to be taken into account for the model.

The set of permeabilities for the reference case provided already a match with the measured and estimated outflow rates that could only marginally be improved by further calibration. The assumptions that led to the reference/final model were that

− the effective permeability of the matrix of 10^{-17} m² exceeds the value for the undisturbed matrix by about three orders of magnitude as in Task 8c, and is possibly caused by a well-connected network of smaller fractures,

− the skin permeability around the tunnels is one order of magnitude lower than the effective matrix permeability,

− the skin permeability around the boreholes is even two orders of magnitude lower to account for a more concentrated impediment by gas bubbles due to stronger converging streamlines,

− the permeability of fractures within a skin is one order of magnitude lower than fracture permeability outside the skin, and

− just one permeability per borehole skin was adopted.

That the flow field resulting from the first try could not be substantially improved is certainly no prove for a correct representation of reality by the model. But it provides the warm feeling that a good approximation within the limits of the model concept has been found.

35

There were of course some shortcomings. The outflow from KO0018G01 and KO0020G01 was too high by a factor of about 10. However the inconsistent trend of increasing pressure in the model and the measured decreasing outflow towards the end of the TASO-tunnel indicates an influence of background fractures that could not be captured by a deterministic model.

Even higher is the difference between measured and calculated outflow from the horizontal borehole KO0011A which had been drilled through wfracture_01 according to the task description. Decreasing the fracture permeability within the borehole skin did not help sufficiently because of the little dimension of this zone. The discrepancy could have been fixed alternatively by shifting the position of wfracture_01 by a little bit more than just a metre to avoid a crossing of fracture and borehole. But the task description indicates that wfracture_01 is indeed crossing KO0011A. This contradiction could not be resolved.

2.3 Isothermal 3D-flow at the Prototype Repository

The procedure of the PR-experiment can roughly be divided into a pre-installation phase where only the tunnel and the boreholes existed and an operational phase after installing buffer and heaters when the heaters were switched on. During the pre-installation phase groundwater flow was isothermal without interference of the buffer and a lot of effort went into characterizing the hydrogeological conditions around the PR. This phase represents therefore the most simple and, at the same time, the best known flow conditions.

The pre-installation phase was therefore considered to be most appropriate to develop a well-founded flow model. Based on the model concept for the BRIE and beginning with the related material data, a first model was set up which was then calibrated against outflow data for the tunnel as well as for the boreholes.

Tunnel and geometry of the deposition boreholes

Two new tunnels were utilized for the project, TADSA (Prototype Repository Tunnel) and TASG (Data acquisition tunnel). The tunnels run sub-parallel to each other. Holes were drilled to lead cables for power and instruments between the tunnels, see Fig. 2.20.
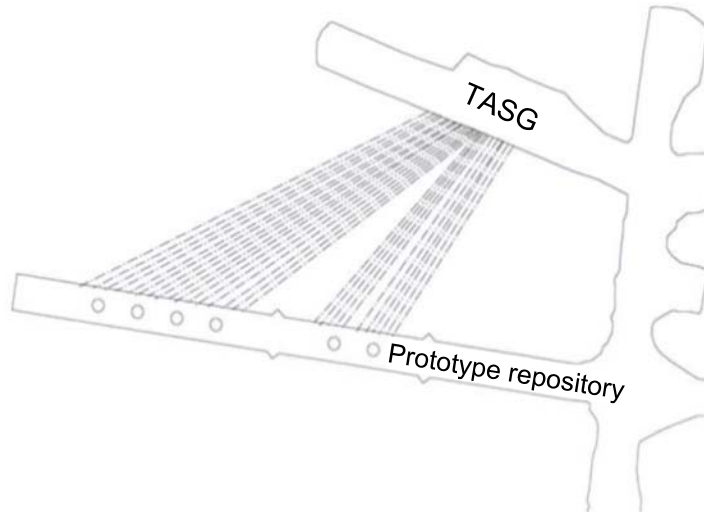
Fig. 2.20   Ground plan showing the PR-tunnel and the G-tunnel; from /BOC 13/

The Prototype Repository tunnel is about 65 m long and has a diameter of 5 m. Six vertical deposition holes, 8.37 m deep and 1.75 m in diameter, have been drilled into the tunnel floor as 1:1 representations of deposition boreholes. The complete Prototype Repository consisted of two sections that were separated by concrete seals to allow for dismantling in two steps without disturbing the ongoing part of the experiment. Section 1 consists of four deposition holes, copper canisters equipped with electrical heaters, bentonite blocks and a deposition tunnel backfilled with a mixture of bentonite and crushed rock and ends with a concrete plug. Two deposition holes are located in section 2 as shown in Fig. 2.21. Characteristic data for each borehole are compiled in Tab. 2.12.
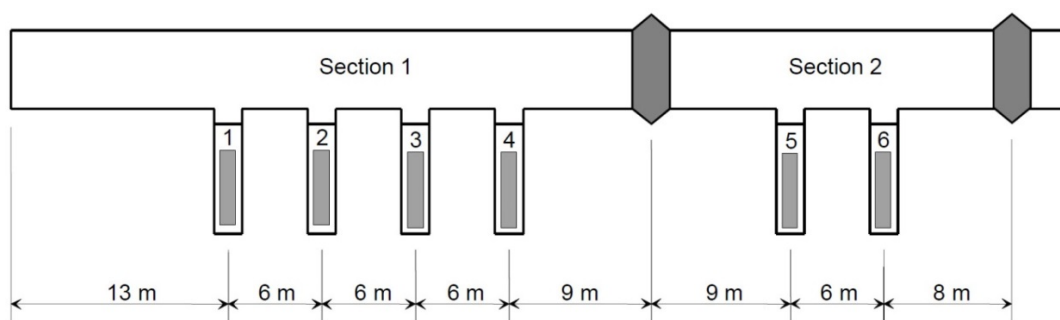
Fig. 2.21   Schematic view of the Prototype Repository; from /BOC 13/

Tab. 2.12   Approximate geometric data of the deposition holes

Deposition hole depth	8 m
Deposition hole diameter	1,75 m
Canister height	~5 m
Canister diameter	1,05 m
Bentonite thickness below the canister	0,5 m
Bentonite thickness above the canister	1,5 m

Secondary boreholes

Location and size of the secondary test boreholes are depicted in /ALM 05/ (Fig. 2.22) as well as in /RHÉ 01/ (Fig. 2.23). According to /FOR 01/ they were already sealed before drilling the deposition boreholes in order to observe changes in the pressure field. During the active time of the PR monitoring was continued /ALM 05/ so that these boreholes did not significantly interfere with the flow field at the PR[11]. They are thus not considered in the flow model.
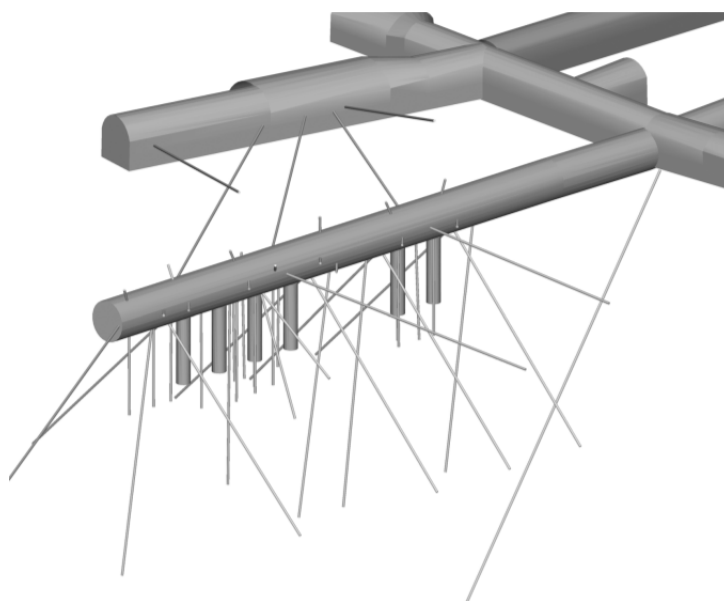
Fig. 2.22   3D-view of location and size of the secondary test boreholes; from /ALM 05/

---

[11] The only exception was when a packer failed in April 2006. On this occasion a significant increase of outflow from the rock could be observed /KRI 10/.
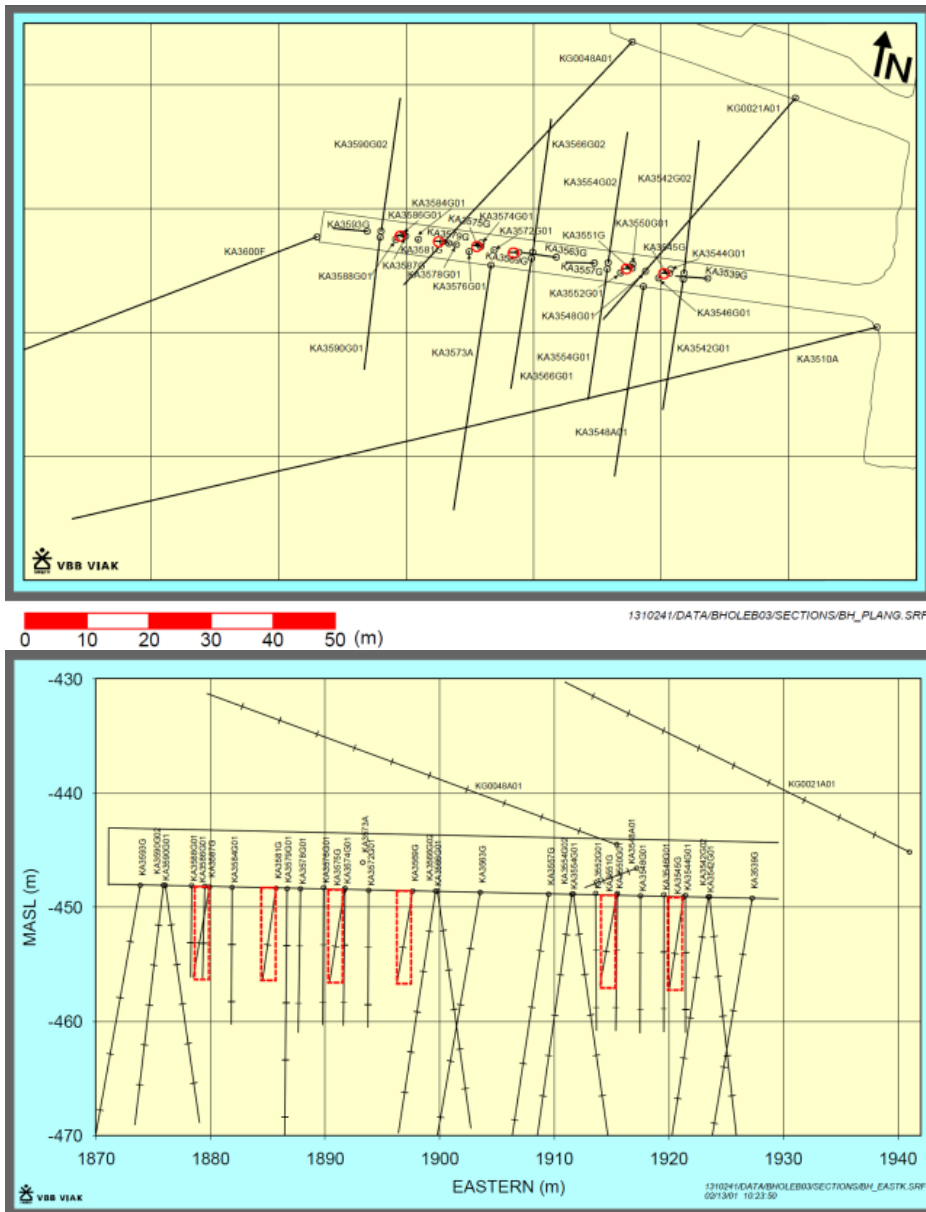
Fig. 2.23   Cross-sections the secondary test boreholes; from /RHÉ 01/

Fractures

No direct information about hydraulic large-scale features was given in the task description /KRI 10/. It included only fracture traces in the drifts. Outflow data for tunnels and boreholes gave some additional indications. Based on these data, a system of six fractures or fracture zones was derived. Only then, the author became aware of the extensive hydraulic test program /RHÉ 01/ that had been performed using the large array of secondary boreholes described above. A comparison of the theoretically postulated frac-

tures with the fractures derived from the hydraulic testing showed that five of the six the-oretical fractures could directly be replaced by the deterministic fractures. Details of the referring reasoning is given in /KRO 17b/.

From this program two major and six minor deterministic fractures had already been identified. The inflow data, however, indicated a third major fracture in section 1. Such a feature at the end of the PR-tunnel was then assumed to fit in with the other two major deterministic fractures in terms of size and orientation. A possible location for this as-sumed fracture had also to comply with the condition that the fracture must have gone undetected by the extensive hydro-testing in the vicinity of the PR-tunnel (cp. Fig. 2.23). The sum of these conditions defined the assumed fracture quite clearly. All considered fractures are depicted in Fig. 2.24. The curious shape of the assumed fracture is caused by being cut off by the model boundary (cp. Fig. 2.29).
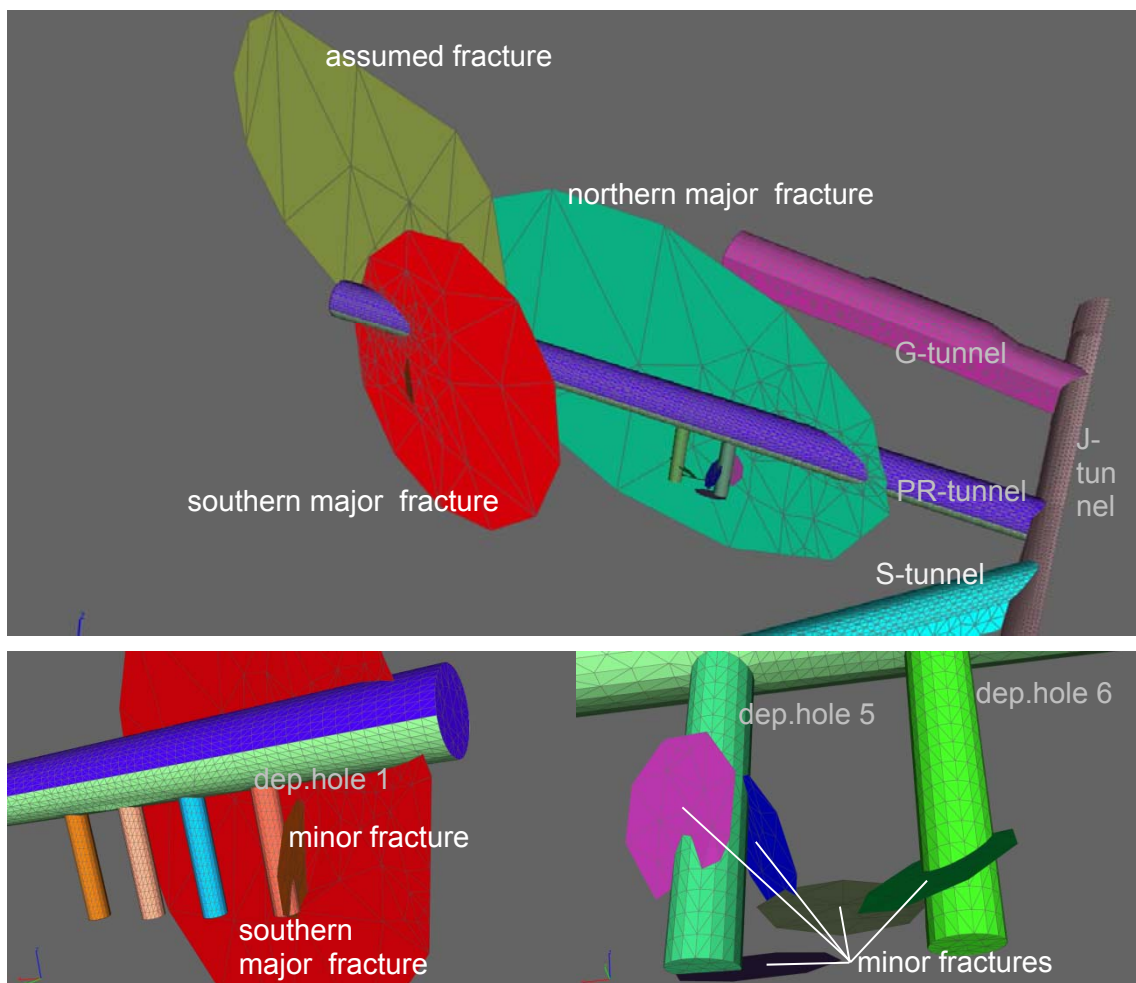
Fig. 2.24   Deterministic fractures according to /RHÉ 01/ and assumed fracture

Outflow

Prototype Repository tunnel

Sectionnally, mean outflow rates have been measured along the PR-tunnel in three campaigns (1997, 1999 and 2000) by means of weirs /RHÉ 01/. The results are compiled in Tab. 2.13 and plotted in Fig. 2.25. Note that range and position of the weirs in the 1997 campaign was different from the other two.
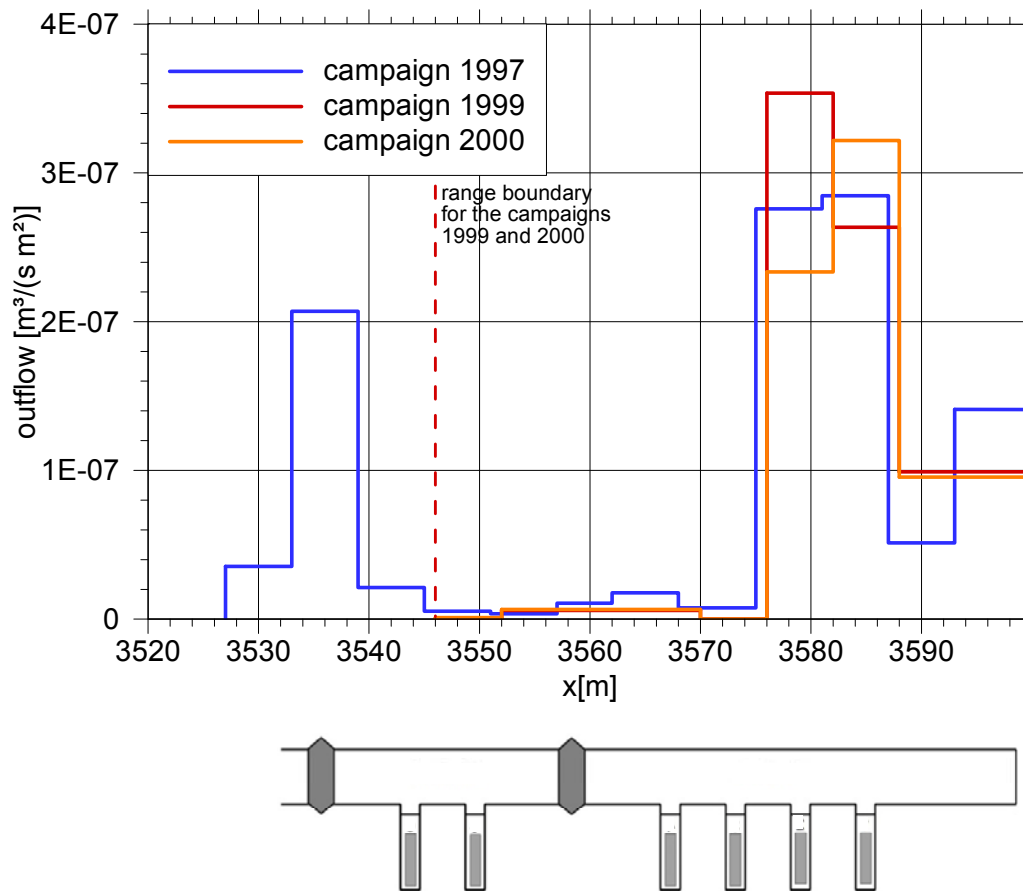
Fig. 2.25 Outflow into the PR-tunnel related to location of the deposition boreholes; □sketch relating to the PR-tunnel after /BOC 13/

Tab. 2.13 Outflow into the PR-tunnel measured by means of weirs; after /RHÉ 01/

Campaign 1997			Campaigns 1999 & 2000				Mass outflow		
Weir sections		Q (1997)	Weir sections		Q (1999)	Q (2000)	1997	1999	2000
from [m]	to [m]	[L/min]	from [m]	to [m]	[L/min]	[L/min]	[kg/s]		
3527	3533	0.20					3.33E-03		
3533	3539	1.17					1,95E-02		
3539	3545	0.12					2.00E-03		
3545	3551	0.03	3546	3552	0.001	0.006	5.00E-04	1.67E-05	1.00E-04
3551	3557	0.02	3552	3570	0.100	0.110	3.33E-04	1.67E-03	1,83E-03
3557	3562	0.05					8,33E-04		
3562	3568	0.10					1.67E-03		
3568	3575	0.05	3570	3576	0.000	0.000	8,33E-04	0.00E+00	0.00E+00
3575	3581	1.56	3576	3582	2.000	1.320	2.60E-02	3.33E-02	2.20E-02
3581	3587	1.61	3582	3588	1.490	1.820	2.68E-02	2.48E-02	3.03E-02
3587	3593	0.29	3588	3600	1.120	1.080	4,83E-03	1,87E-02	1,80E-02
3593	3600	0.93					1.55E-02		

Comparing mean outflow rates with data from the BRIE-site

The data for mass outflow from Tab. 2.13 was transformed into flux densities. On the basis of flux densities the outflow rates into the PR-tunnel can be compared with those of the TASO-tunnel. For Task 8d an average value of $3.63 \cdot 10^{-9}$ m³/(m² s) had been estimated /KRO 17a/ for the tunnel surface without large fractures. Assuming the same geostatistics for the background fractures at the PR as for the BRIE-site indicates a section in the PR-tunnel from 3545 m to 3575 m that is free of larger fractures.

Deposition boreholes

There had been three different measurements in the deposition boreholes:

total outflow into the deposition holes /RHÉ 01/ (see Tab. 2.14)
localized outflow /RHÉ 01/
diaper measurements in deposition holes 2 and 3 /RHÉ 01/ as well as 5 and 6 /FOR 05/

The results of the total outflow measurements are summarised in Tab. 2.14. Mean values are derived also where applicable. They indicate that total outflow varies by a factor of ± 2 around a value of $1.5 \cdot 10^{-04}$ l/min except in borehole 1 where total outflow exceeds this average by a factor of 53. The other two measurement campaigns were of much less relevance as only total outflow rates were later used for calibration.

Tab. 2.14 Total outflow into the deposition boreholes; after /RHÉ 01/

borehole		representative total outflow rates				
		1999	2000/1	2000/2	mean	
code name	#	[l/min]				[kg/s]†
DA3587G01	1	0,0800	0,0787		0,0794	1,32E-03
DA3581G01	2	0,0016	0,0022		0,0019	3,17E-05
DA3575G01	3	0,0028	0,0031		0,0030	5,00E-05
DA3569G01	4	0,0007			0,0007	1,17E-05
DA3551G01	5		0,0016	0,0016	0,0016	2,67E-05
DA3545G01	6		0,0027		0,0027	4,50E-05

† Conversion from [l] to [kg] using a water density of 1000 kg/m³.

Other drifts

Additional weir tests had been performed in different tunnels and tunnel sections. Estimations about outflow into the PR as well as neighbouring drifts are shown in Fig. 2.26. The outflow rate for the PR-tunnel thus amounts to 0.084 l/min per metre tunnel or $8.9 \cdot 10^{-8}$ m³/(s m²) referring to the tunnel surface. As a rule of thumb an average value of 0.1 l/(min m) or $1.1 \cdot 10^{-7}$ m³/(s m²) applies to the whole investigated tunnel system. Note that this average includes outflow from strongly water-producing local fractures. These data are therefore of very limited use for model calibration if the local features are not taken into account.
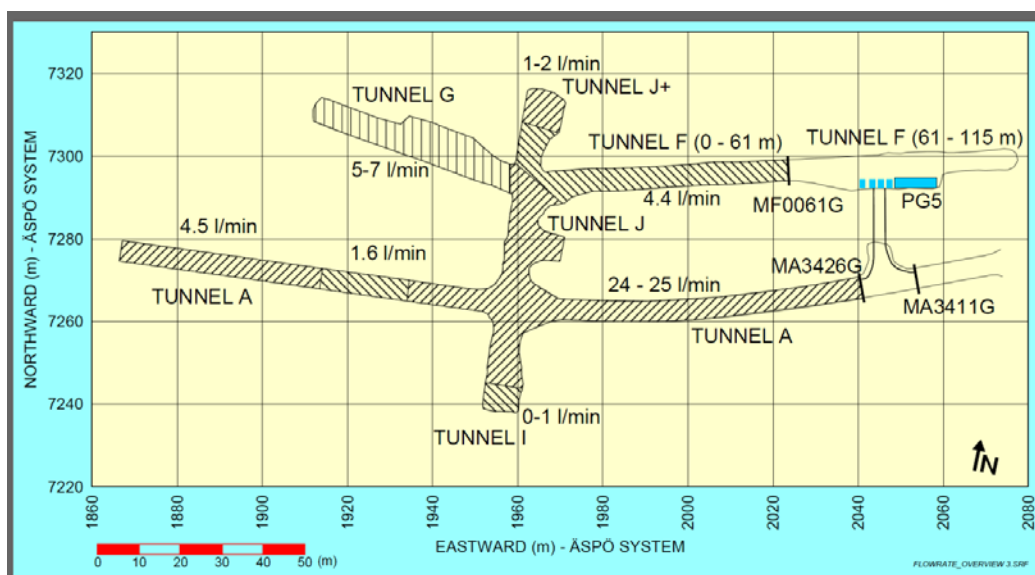
Fig. 2.26 Estimated outflow into different tunnel sections; from /RHÉ 01/

Hydraulic properties

Matrix and background fractures

During model calibration in the framework of Tasks 8c and 8d the strong influence of the background fractures had become apparent increasing the overall permeability of matrix and background fractures up to 10^{-17} m². This value thus became a starting point for the model calibration.

Fractures

Location, orientation, size and permeability of the detected fractures are compiled in Tab. 2.15. The additionally assumed fracture in the model is actually a copy of the northern major fracture where strike was slightly modified. This applies also to the permeability. In contrast to the permeability of the detected fractures this parameter was open to variation in the course of calibration, though.

Tab. 2.15 Characterisation of the deterministic fractures; mainly from /RHÉ 01/

feature	centre coordinates			strike	dip	radius	transmissivity[12]
	x	y	z				
	[m]	[m]	[m] (amsl)	[°]	[°]	[m]	[m²/s]
northern major fracture[13]	1892	7289	-449	118	88	20	$5 - 10 \cdot 10^{-8}$
southern major fracture	1887	7266	-449	124	89	20	$7 - 9 \cdot 10^{-8}$
minor fracture 1	1878.28	7275.03	-453.53	354	79	2	$8.1 \cdot 10^{-9}$
minor fracture 2	1915.42	7271.06	-455.24	312	40	2	$4.7 \cdot 10^{-9}$
minor fracture 3	1917.50	7269.90	-455.56	271	38	2	$3.3 \cdot 10^{-9}$
minor fracture 4	1919.55	7268.80	-456.66	278	24	2	$1.7 \cdot 10^{-9}$
minor fracture 5	1919.55	7268.80	-453.54	164	64	2	$2.8 \cdot 10^{-10}$
minor fracture 6	1921.45	7270.22	-453.14	298	64	2	$1.3 \cdot 10^{-8}$
assumed fracture	1153.18	7775.34	-435.30	126	88	20	$5 - 10 \cdot 10^{-8}$

---

[12] For conversion of the transmissivity T into a hydraulic conductivity K it is necessary to define a more or less arbitrary fracture aperture d. The formula reads then: K=T/d.

[13] Note that the northern major fracture has been modified according to speculations of /RHÉ 01/ to an ellipsoid which still has a vertical diameter of 40 m.

Salinity

As for the models in Tasks 8c and 8d salinity variation were also neglected for the PR-site.

Model description

Domain

Model size is approximately 150 m x 200 m x 50 m. The model consists basically of three 3d-components: the matrix, the skin around the geotechnical openings and the fractures. Numerically it is necessary to represent these components not only by 3d-Elements but also by 2d-elements describing the surface and allowing for allocation of boundary conditions. These elements are grouped in so-called subsets which are identified by assigned names and are in some cases included in the following figures. The model surface is depicted in Fig. 2.27.
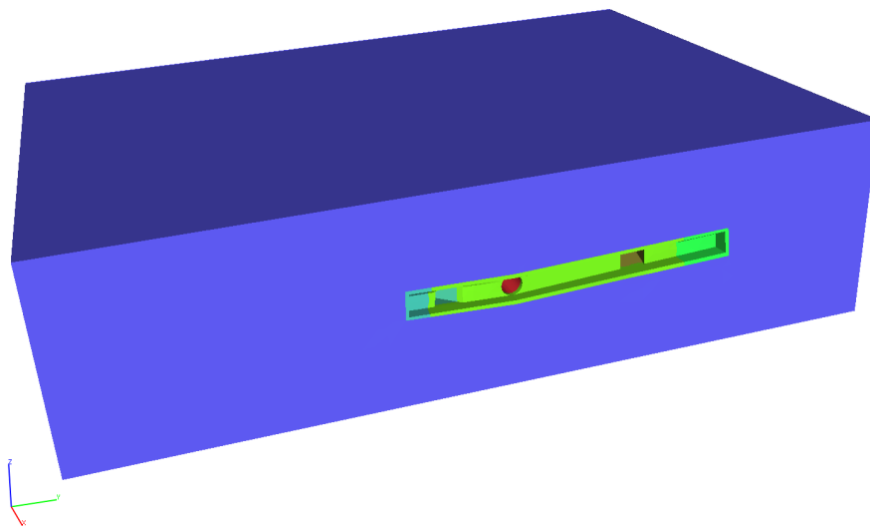
Fig. 2.27   Matrix block including cut through the IJ-tunnel

The model comprises four tunnels called S-, PR- G- and J-tunnel here, and two extensions to the J-tunnel called I- and J+-tunnel as shown in Fig. 2.28. The six deposition holes drilled from the PR-tunnel are also enveloped in a skin zone like the tunnels. Additionally, there are three major and six minor deterministic fractures (the northern and the southern as well as the assumed fracture plus minor fractures M1 to M6). Only the as-

sumed fracture cross-sects the model surface (c.f. Fig. 2.29) and only fracture M3 does not cut through the PR-tunnel or a deposition borehole.

The data for the fractures were given in terms of transmissivities which had to be transformed into permeabilities for modelling purposes. These two quantities can be related with the help of an arbitrary fracture width which was chosen here to be 1 cm. Since steady-state conditions were assumed, porosity is not required. The data used for the reference model are compiled in Tab. 2.16.
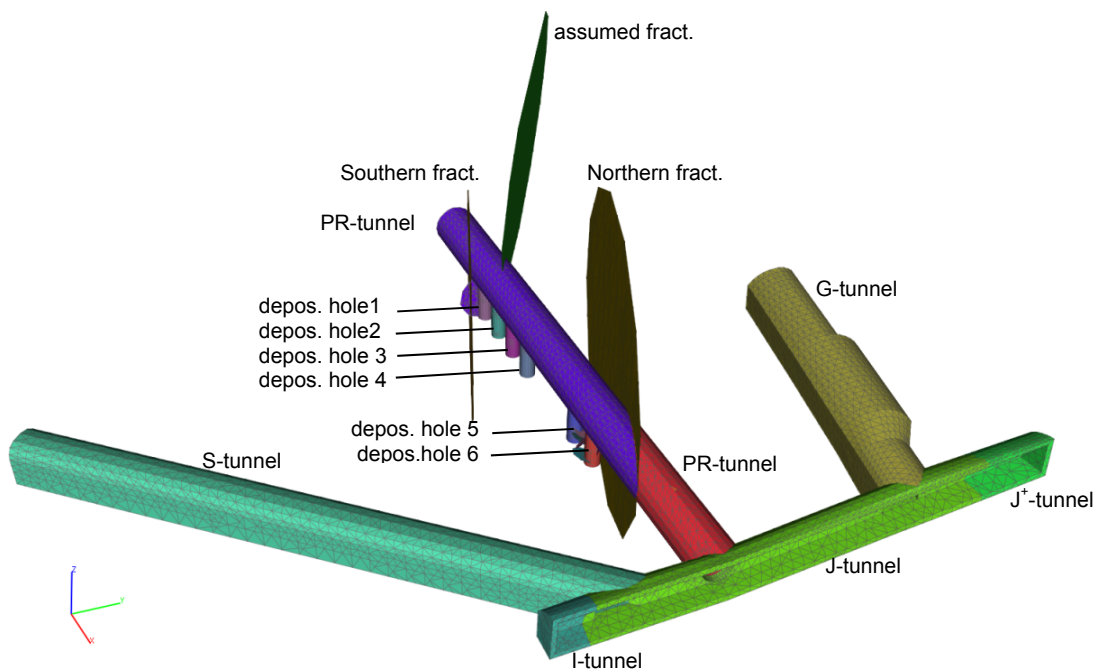
Fig. 2.28   3d-subsets of the model (except matrix) including their names
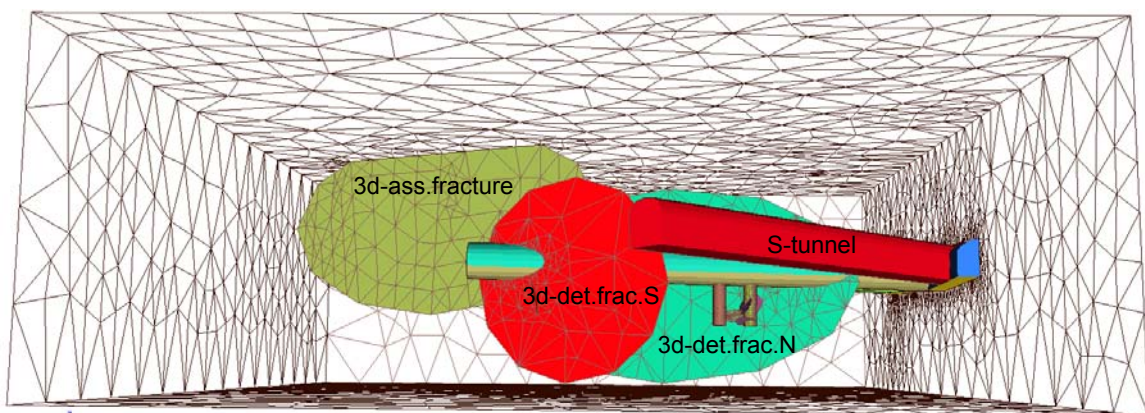
Fig. 2.29   Relation of large fractures to the outer model surface

Tab. 2.16 Hydraulic data

Subset name	Permeability [m²]	Transmissivity [m²/s]
3d-matrix	10^{-17}	not applicable
3d-PR-back-skin	$10^{-18\,*)}$	not applicable
3d-PR-front-skin		
3d-dep.h.1-skin	$10^{-18\,*)}$	not applicable
3d-dep.h.2-skin		
3d-dep.h.3-skin		
3d-dep.h.4-skin		
3d-dep.h.5-skin		
3d-dep.h.6-skin		
3d-S-skin	$10^{-18\,*)}$	not applicable
3d-G-skin		
3d-IJ-skin		
3d-I+-skin		
3d-J+-skin		
3d-det.frac.N	$8 \cdot 10^{-13\,**)}$	$5 - 10 \cdot 10^{-8}$
3d-det.frac.S	$8 \cdot 10^{-13\,**)}$	$7 - 9 \cdot 10^{-8}$
3d-det.fr.M1	$8 \cdot 10^{-14\,**)}$	$8.1 \cdot 10^{-9}$
3d-det.fr.M2	$5 \cdot 10^{-14\,**)}$	$4.7 \cdot 10^{-9}$
3d-det.fr.M3	$3 \cdot 10^{-14\,**)}$	$3.3 \cdot 10^{-9}$
3d-det.fr.M4	$2 \cdot 10^{-14\,**)}$	$1.7 \cdot 10^{-9}$
3d-det.fr.M5	$3 \cdot 10^{-15\,**)}$	$2.8 \cdot 10^{-10}$
3d-det.fr.M6	$1 \cdot 10^{-13\,**)}$	$1.3 \cdot 10^{-8}$
3d-ass.fracture	$8 \cdot 10^{-13\,**)}$	$5 - 10 \cdot 10^{-8}$
3d-det.frac.N-skin	$8 \cdot 10^{-14\,***)}$	not used
3d-det.frac.S-skin	$8 \cdot 10^{-14\,***)}$	
3d-det.fr.M1-skin	$8 \cdot 10^{-15\,***)}$	
3d-det.fr.M2-skin	$5 \cdot 10^{-15\,***)}$	
3d-det.fr.M3-skin	$3 \cdot 10^{-15\,***)}$	
3d-det.fr.M4-skin	$1 \cdot 10^{-15\,***)}$	
3d-det.fr.M5-skin	$3 \cdot 10^{-16\,***)}$	
3d-det.fr.M6-skin	$1 \cdot 10^{-14\,***)}$	
3d-ass.frac-skin	$8 \cdot 10^{-14\,***)}$	

- *) 1/10 of matrix value
- **) estimated for a fracture width of 1 cm
- ***) 1/10 of fracture value

Boundary conditions

The isothermal flow model requires only pressure boundary conditions. These fall into two categories: pressure data for the matrix at the outer surface of the model and atmospheric pressure at the surface of the geotechnical openings. Pressure data for the matrix had been provided along with the task description as a 3d-cloud of data points and had to be pre-processed by means of an inverse distance weighting scheme to ex-

tract appropriate values at the outer model surface. The resulting pressure distribution is shown in Fig. 2.30.
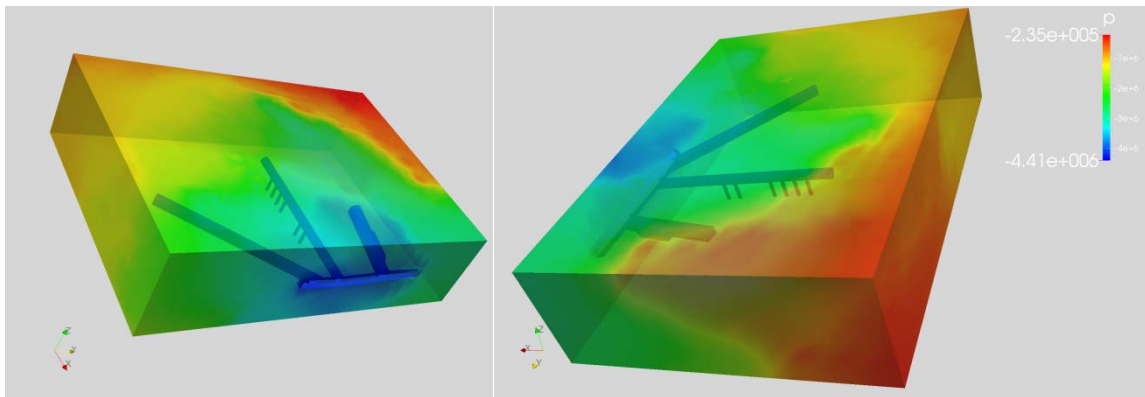
Fig. 2.30   Prescribed pressure distribution at the model boundaries

Different areas of the inner surface of the PR-tunnel were allocated to different 2d-subsets in such a way that outflow from a subset relates to a corresponding outflow measurement in the field. Fig. 2.31 depicts the 2d-subsets representing areal outflow from the tunnel surface or the deposition boreholes.
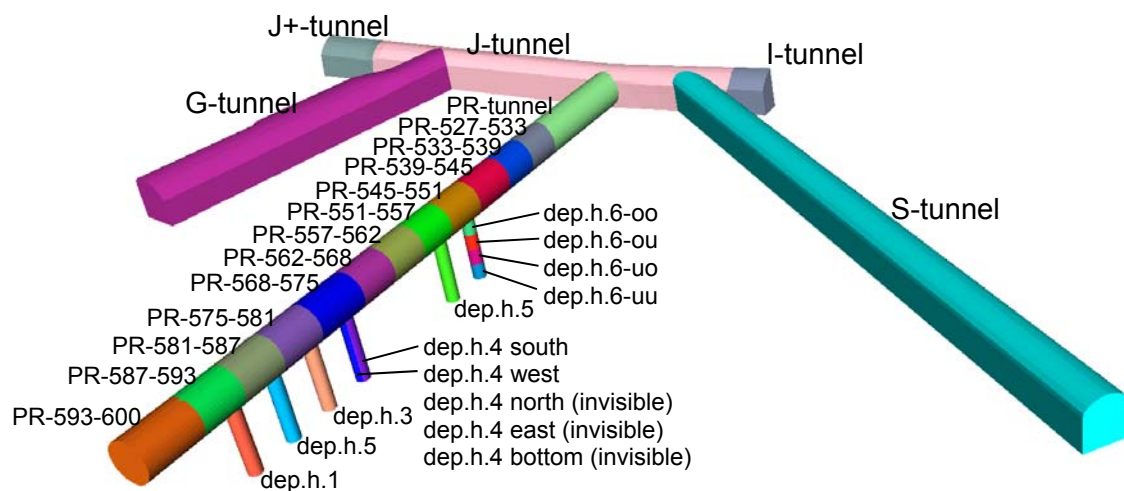
Fig. 2.31   2d-subsets of the model to which atmospheric pressure is assigned

The surface of the geotechnical openings include also the openings of the fractures that had been cut by excavation. The boundary edges of the fractures at the tunnel surface are a bit more difficult to visualize in a comprehensible way as the fractures resemble

planar structures so that the edges look rather like 1d- than 2d-features[14]. Fig. 2.32 shows therefore four variants of the same view, with or without other subsets interfering with the view and with or without the related fractures.

Calibration targets

Calibration of the steady-state, single-phase, and isothermal flow model is based on the following data on outflow:

− Outflow into sections of the PR-tunnel
− Total outflow into deposition boreholes
− Outflow into G-, I-, and J+ tunnel, respectively

For each of the subsets to which atmospheric pressure had been assigned as boundary conditions, outflow can be calculated. Note that Fig. 2.31 also shows that the surfaces of deposition holes 4 and 6 are subdivided to allow for a closer inspection of circumferential and vertical distribution of the outflow into these holes. The target outflow values for calibration are compiled in Tab. 2.17 to Tab. 2.19.

Tab. 2.17   Outflow into the sections of the PR-tunnel; after /RHÉ 01/

weir section			adopted outflow ranges
from	to		
[m]	[m]	subset name	[kg/s]
3527	3533	PR-527-533	$3.33 \cdot 10^{-3}$
3533	3539	PR-533-539	$1.95 \cdot 10^{-2}$
3539	3545	PR-539-545	$2.00 \cdot 10^{-3}$
3545	3551	PR-545-551	$1.67 \cdot 10^{-5}$ - $5.00 \cdot 10^{-4}$
3551	3557	PR-551-557	$3.33 \cdot 10^{-4}$ - $1.83 \cdot 10^{-3}$
3557	3562	PR-557-562	$8.33 \cdot 10^{-4}$ - $1.83 \cdot 10^{-3}$
3562	3568	PR-562-568	$1.67 \cdot 10^{-3}$ - $1.83 \cdot 10^{-3}$
3568	3575	PR-568-575	$<8.33 \cdot 10^{-4}$
3575	3581	PR-575-581	$2,20 \cdot 10^{-2}$ - $3.33 \cdot 10^{-2}$
3581	3587	PR-581-587	$2.48 \cdot 10^{-2}$ - $3,03 \cdot 10^{-2}$
3587	3593	PR-587-593	$4,83 \cdot 10^{-3}$ - $1.87 \cdot 10^{-3}$
3593	3600	PR-593-600	$1.55 \cdot 10^{-2}$ - $1.87 \cdot 10^{-3}$

---

[14] This is reflected in the subsets names.
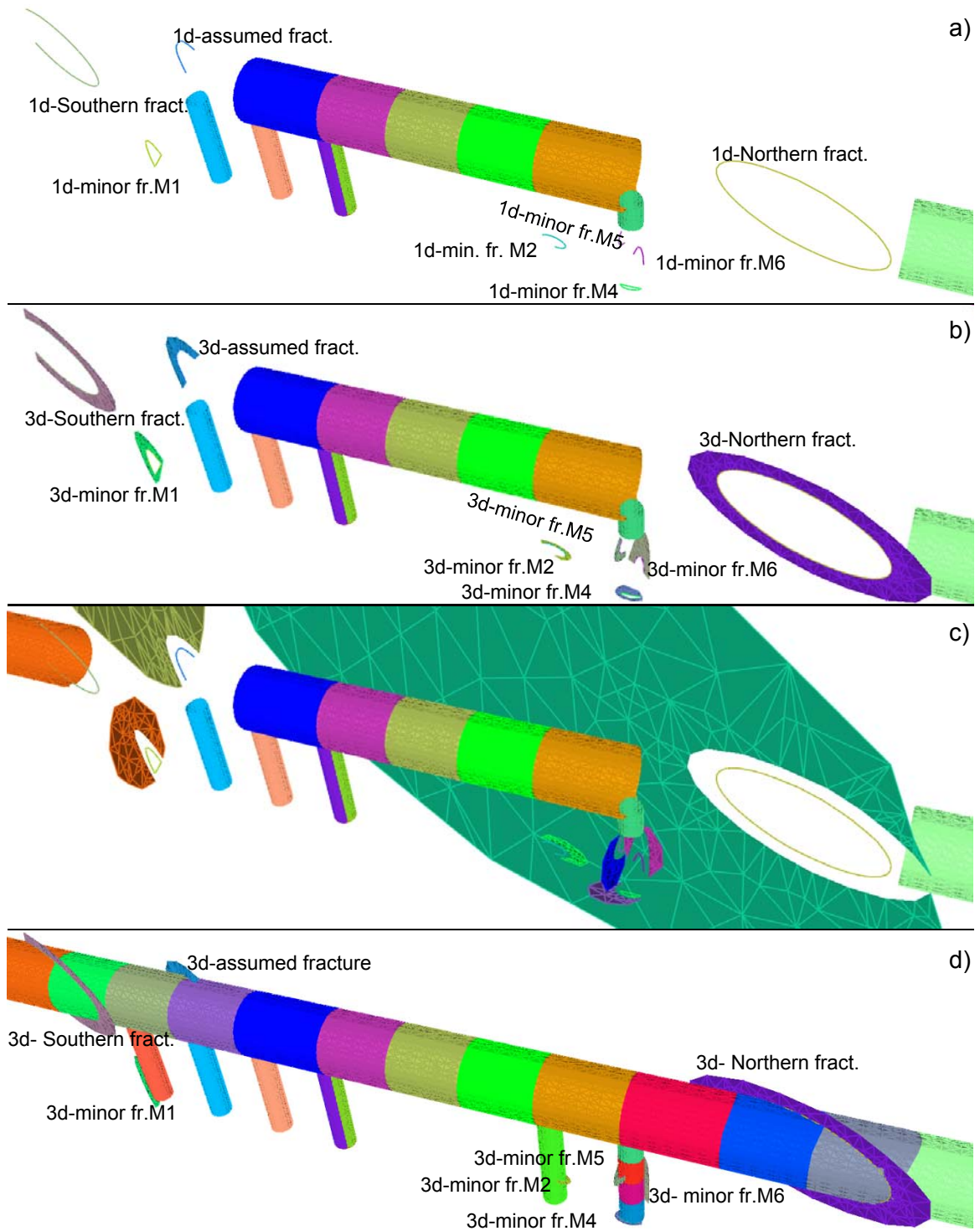
Fig. 2.32 Visualization of fracture boundary edges with boundary conditions;

a) only boundary edges and some parts of tunnel and boreholes missing

b) as a) plus parts of fractures within the skin

c) as a) plus parts of fractures outside the skin

d) as b) with all parts of tunnel and boreholes

Tab. 2.18   Outflow into the deposition boreholes; after /RHÉ 01/

| borehole | | representative total outflow rates |
code name	subset name	[kg/s]
DA3587G01	dep.h.1	$1.32\ 10^{-2}$
DA3581G01	dep.h.2	$3.17\ 10^{-5}$
DA3575G01	dep.h.3	$5.00\ 10^{-5}$
DA3569G01	dep.h.4	$1.17\ 10^{-5}$
DA3551G01	dep.h.5	$2.67\ 10^{-5}$
DA3545G01	dep.h.6	$4.50\ 10^{-5}$

Tab. 2.19   Outflow into other drifts; after /RHÉ 01/

| tunnel | | representative total outflow rates | |
code name	subset name	[l/min]	[kg/s]
TASG	G-tunnel	5 - 7	$8.33\ 10^{-2}$ - 0.117
TASI	I-tunnel	< 1	$< 1.67\ 10^{-2}$
TASJ[+]	J+-tunnel	1 - 2	$1.67\ 10^{-2}$ - $3.33\ 10^{-2}$

Results

Calibration

Calibration was basically performed on the basis of three outflow measurement campaigns along the PR-tunnel as well as on measured outflow into the deposition boreholes. It required a series of four increasingly improved models. Data and approaches from the BRIE-model were applied to the first model (model 1) where appropriate. This led immediately to a good agreement of model results with the outflow data for the six deposition holes but underestimated flow into the PR-tunnel. The results of this first as well as of all the following calibration steps are compiled in Fig. 2.33.

An increase of the matrix permeability by a factor of 5 (model 2) improved the fit for the outflow into the tunnel considerably. One exception, though, was found at the tunnel section that was presumably influenced by the assumed fracture. Here, the calculated outflow was not nearly reflecting the measured high outflow rate.

Since the choice of the permeability for the assumed fracture offered a certain degree of freedom, the permeability was also increased by a factor of 5 (model 3). This led to a

satisfying if a bit low profile for the outflow along the tunnel. No significant changes oc-
curred in the outflow rates for the deposition boreholes from model 2 to model 3.
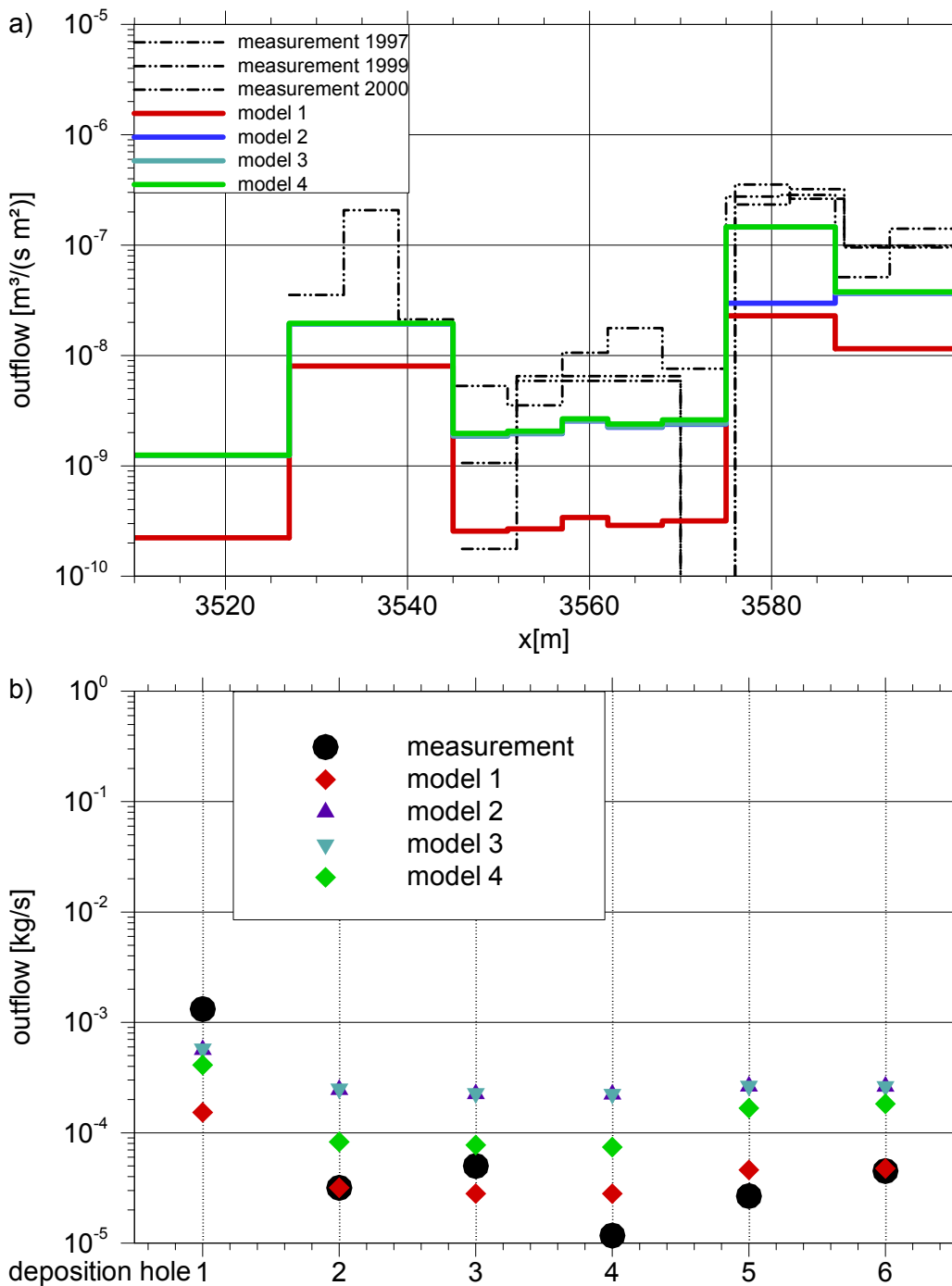
Fig. 2.33   Outflow measurements and model results; a) flux density along the PR-
tunnel, b) total outflow into the six deposition boreholes

However, outflow into the boreholes was now overestimated. As a final measure the permeability of the borehole skins was divided by a factor of 5 (model 4) which resulted in a reasonably good match of calculation and measurement for the tunnel as well as for the boreholes.

It has to be mentioned here that outflow rates for the G-, the I+- and the J+-tunnel calculated with model 4 lay up to two orders of magnitude below the measured values. However, the calculated rates represent only outflow over the matrix because there had been no means to incorporate fractures appropriately. Flow from such fractures could have contributed considerably to the total outflow rate.

All in all, matching the calculated outflow from the rock to the measured outflow distribution along the PR-tunnel and the outflow into the six "deposition boreholes" required only a moderate modification of the initially used permeabilities. The approach for modelling flow at the BRIE-site can thus be considered to be successfully transferred to the Prototype Repository as all geometrical and flow data are acknowledged.

Pressure

The pressure plot in Fig. 2.34 shows the zones of higher pressure being shifted towards the tunnels and boreholes because of the skin. Also the footprint of the three large deterministic fractures is clearly visible. As expected, the pressure gradients point generally from the model boundary towards the geotechnical openings.
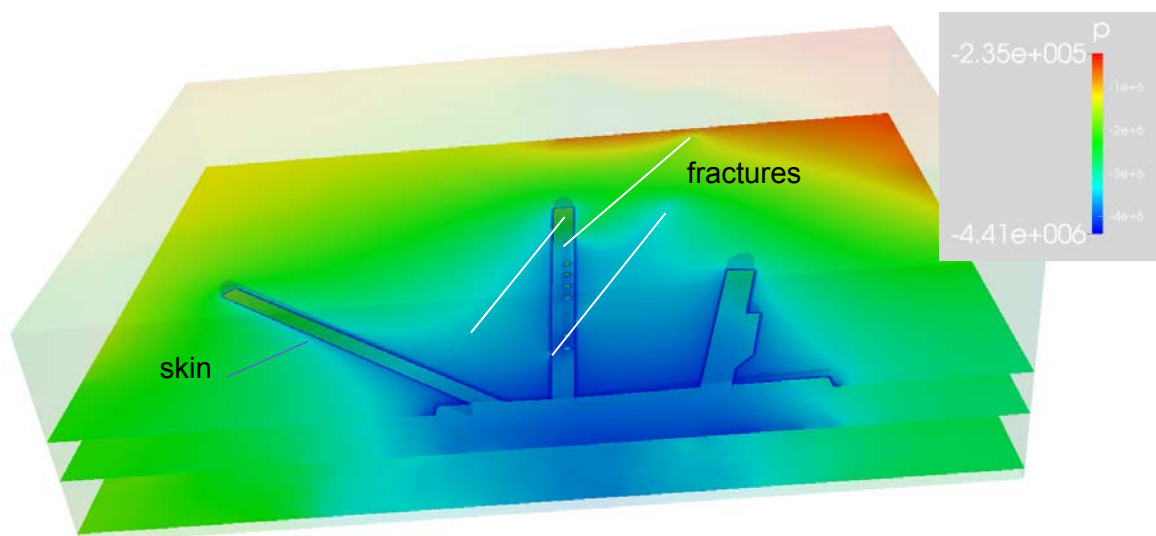
Fig. 2.34   Horizontal cross-sections through the spatial pressure field

Flow

The resulting velocity field is rather complex. Shown in Fig. 2.35 is a horizontal cross-section through the PR depicting only the scalar field of the absolute velocity. A closer look into this plot reveals two phenomena that are specific for fracture flow. The first one can be observed at the rim of the fractures. Very high velocities are found here because the catchment volume at the rim of the fracture is much larger than at its face. This is illustrated by a close-up exemplarily done for the northern discrete fracture in Fig. 2.36. A theoretical investigation of distortions in a unidirectional flow field caused by differently orientated fractures has been reported by /MAT 04/ where the authors come to the same conclusions. Much in the same way also tunnel ends attract more water than the lateral tunnel surfaces (see also Fig. 2.36).
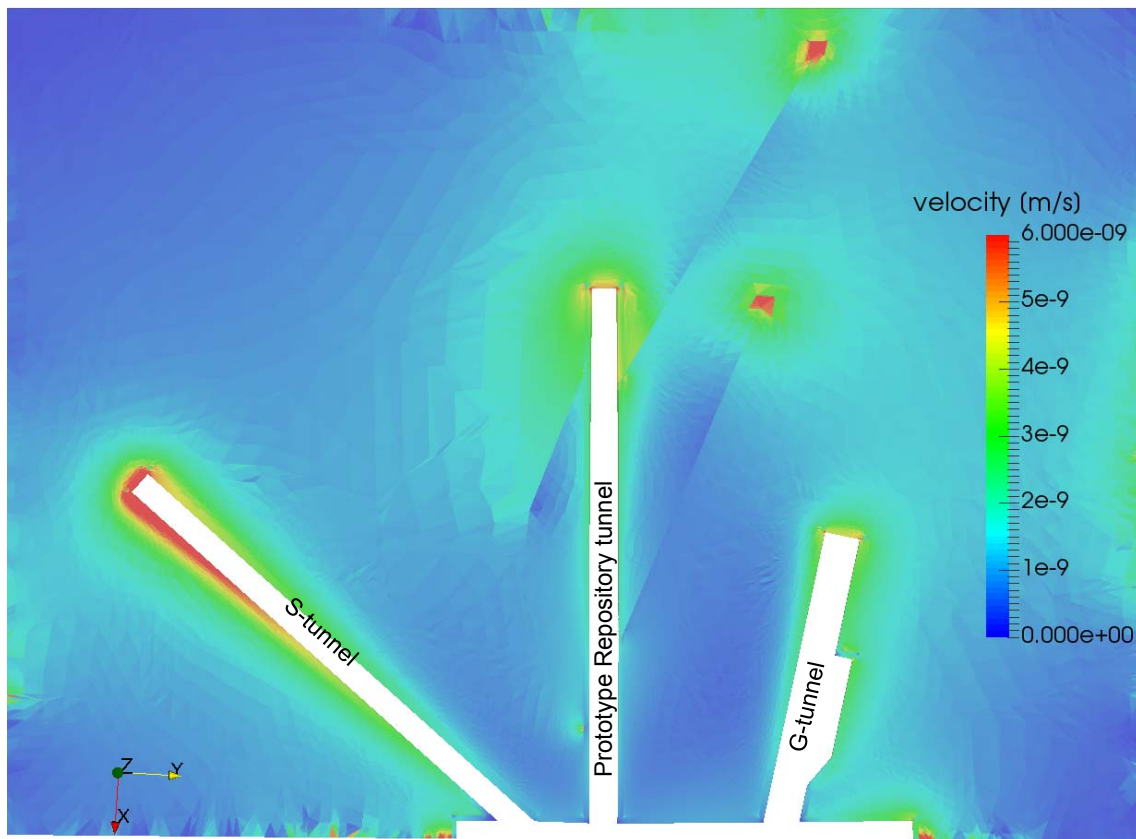
Fig. 2.35   Absolute velocity in a horizontal cross-section
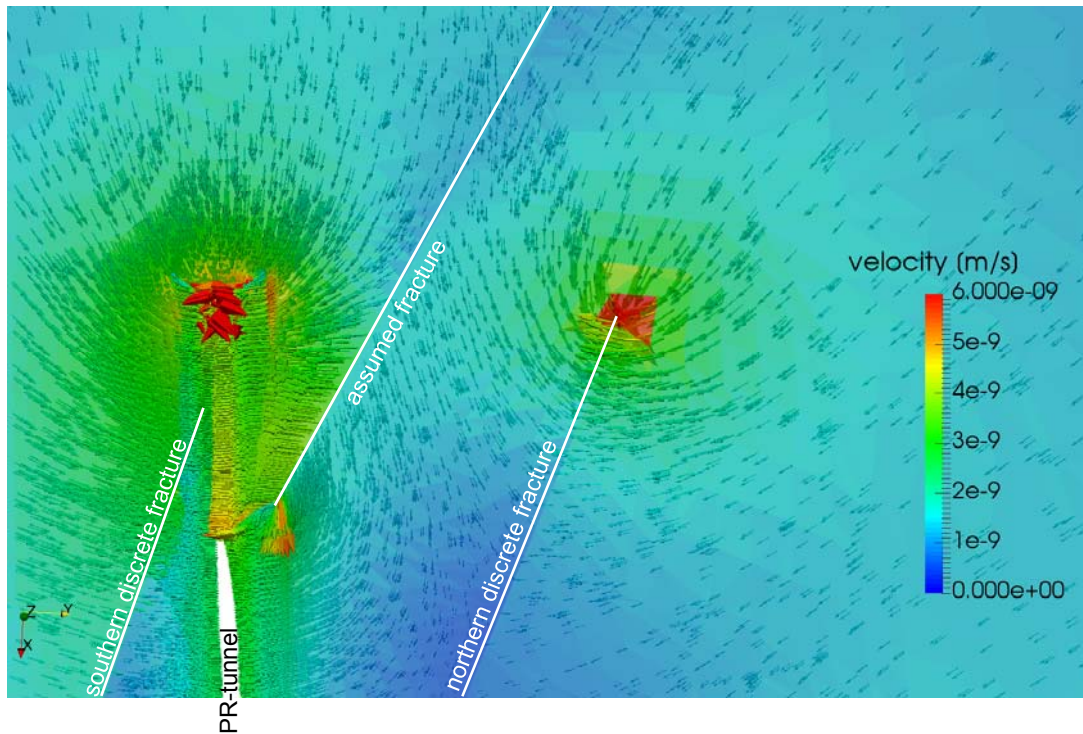
Fig. 2.36   Velocity at the end of the PR-tunnel and at the northern discrete fracture

The second phenomenon concerns the sharp velocity contrasts across the fractures. In Fig. 2.35 the position of the fractures can clearly be identified by this phenomenon. These contrasts form where water reaching a fracture from the matrix is diverted along the fracture because of the comparatively high fracture permeability.

Depending on the overall flow conditions and the permeability distribution, several local flow conditions can prevail at a fracture: water can (a) be drawn from both sides of the fracture, (b) be drawn from one side but also released at the other side, and (c) be re-leased at both sides. Additionally, in case (b) there can be either more water drawn than released (b1) or the reverse (b2). In case (b1) the result is a "hydraulic shading" of the region beyond the fracture.

All variations occur in the flow field around the assumed fracture as shown in Fig. 2.37. Looking along the assumed fracture in Fig. 2.37 from top to bottom, case (a) can be identified first. However, significantly more water is drawn from the left than from the right hand side. Following the fracture trace downwards, the inflow from the right hand side decreases until inflow becomes outflow and case (b1) applies. Even further down outflow to the right eventually exceeds the inflow from the left hand side (case b2). Even-

55

tually, at the bottom of the plot even case (c) can be found where water is apparently strongly attracted to the northern discrete fracture as well as to the PR-tunnel.
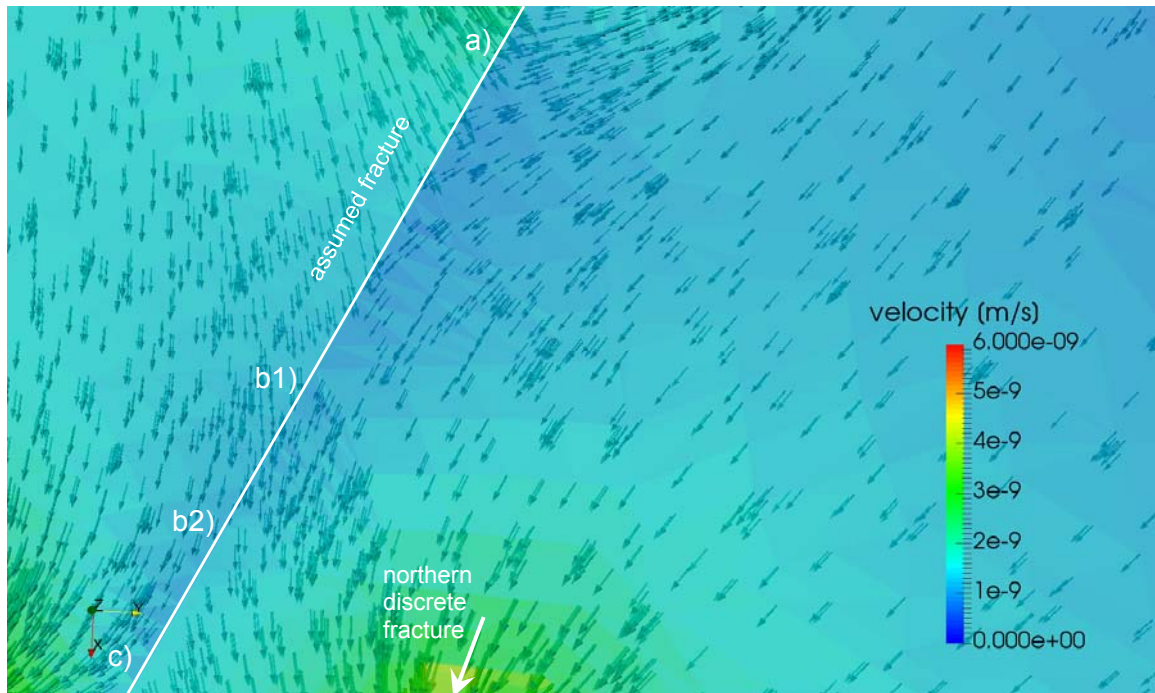
Fig. 2.37   Flow across the northern deterministic fracture

Another interesting flow phenomenon can be observed at the top of the boreholes as exemplarily shown for borehole 1 in Fig. 2.38. The flow pattern is here clearly influenced by the skin zones around borehole and tunnel. These skin zones are depicted in Fig. 2.39 where the top of the tunnel skin as well as one side of the skin of deposition borehole 1 is cut open. Fig. 2.39 shows that the tunnel skin had been assumed to be thicker than the borehole skin and that it is not considered to be interrupted by the borehole skin. However, the same permeability had been assigned to both skin types anyway (cp. Tab. 2.16).

What plays a role here, though, are the different diameters of tunnel and borehole as well as the different thicknesses of the skin. Outside the skin zones water is preferentially drawn towards the tunnel instead of the borehole because of its much larger diameter. The less converging streamlines result in a more favourable pressure distribution for the flow. Close to the skin, though, at the contact of tunnel and borehole skin, less resistance to flow is established by the borehole skin because of the lesser thickness. Water is therefore locally diverted towards the borehole leading to a significantly increased

flow velocity. As a consequence, flow into the borehole within the tunnel skin is by contrast quite low. It would be highly interesting whether this phenomenon could be confirmed in situ.
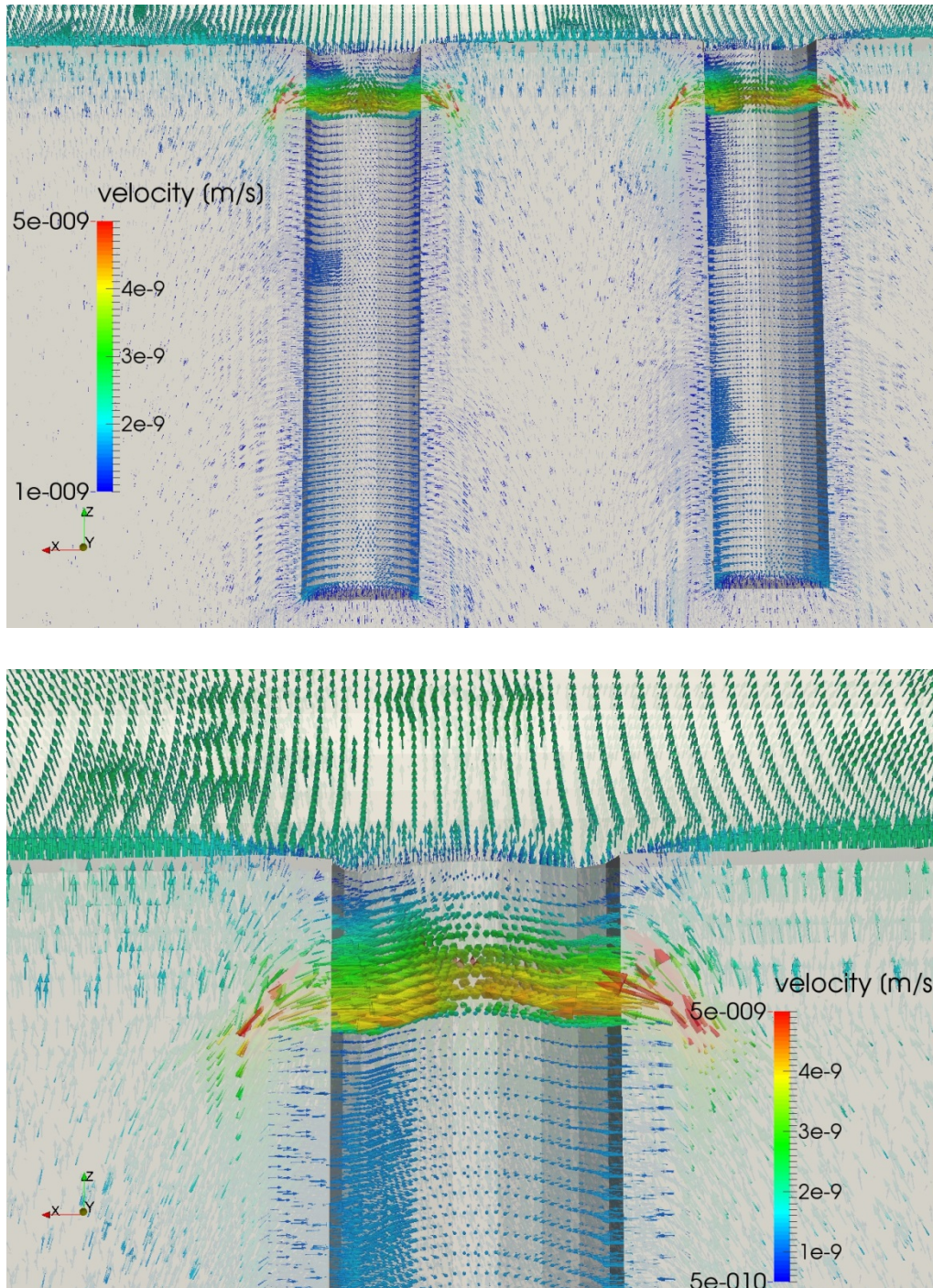
Fig. 2.38   Flow at the top of borehole 1 at different spatial resolutions
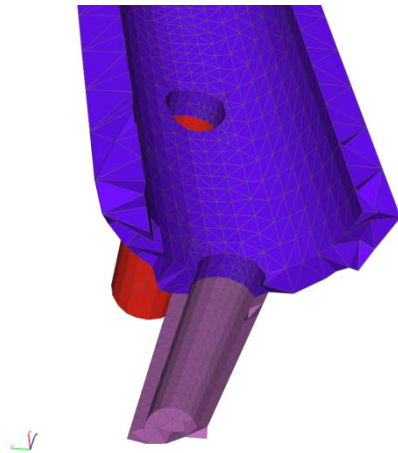
Fig. 2.39   Skin zones of the PR tunnel and borehole 1 sliced open.

One more flow effect can be observed in Fig. 2.40. As the PR-tunnel is attracting water from the boundaries, the streamlines are essentially radially converging towards the tunnel. Water is therefore accelerated in the direction of flow which becomes evident in the immediate vicinity of the tunnel. The increased flow velocity can be identified in Fig. 2.40 by the green zone around the tunnel. Note that the above discussed effects of increased flow velocity at the end of the tunnel, at the rim of the southern discrete fracture and close to the top of the boreholes can also be recognised in this figure.
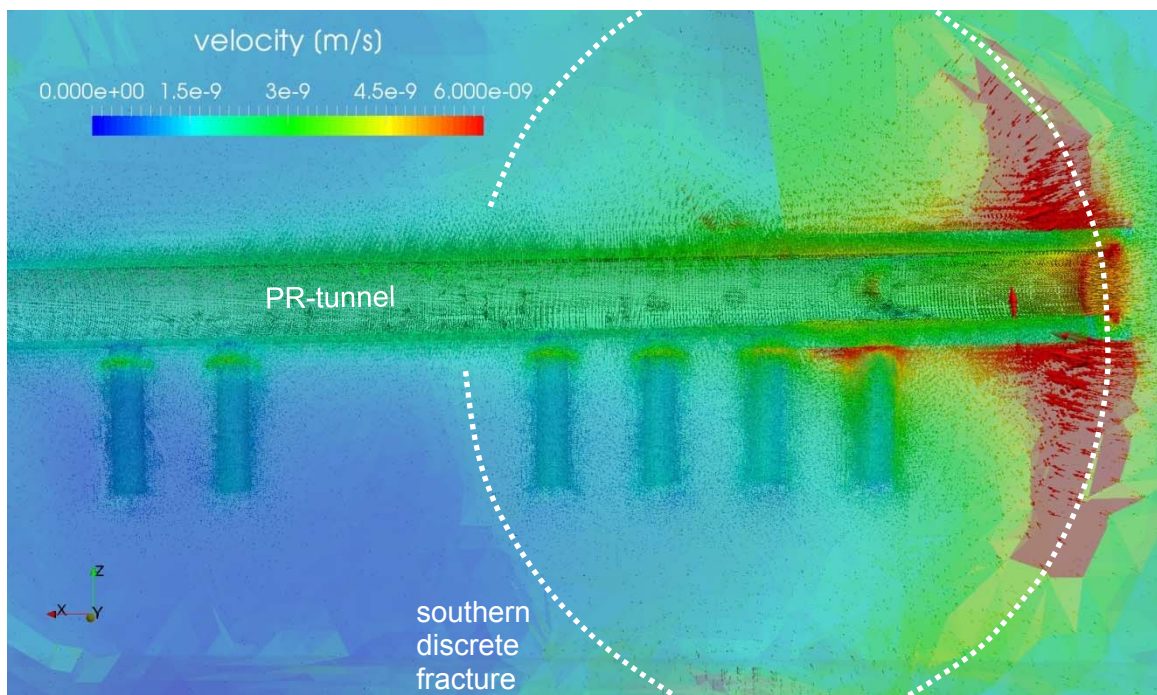
Fig. 2.40   Flow field in a vertical semi-transparent slice of finite thickness.

58

2.4 Non-isothermal 3D-flow at the Prototype Repository

A certain conceptual inconsistency between the hydraulic and the thermal part of the envisaged TH-model became apparent when it came to the boundary conditions. While the fluid flow model represents the pre-installation phase, heat flow occurs only during the operational phase. The difference between these phases lies in the deposition boreholes which are not filled during the pre-installation phase but contain heaters and the buffer during the operational phase.

The hydraulic effect of the bentonite buffer on the flow field in the host rock is in the beginning that more water is drawn by the clay than the rock can provide which is more or less equivalent with an open boundary. Later, though, the clay impedes further water outflow from the rock quite effectively which can be approximated by a no-flow boundary. The BRIE had shown that significant re-saturation of the bentonite via the distributed outflow from the rock can require considerably more than the testing period of 520 days /FRA 15/. For the orientating investigations intended here, the boreholes are therefore assumed to be hydraulically open all the time.

This assumption allowed for dispensing with buffer and heater in the TH-model. But heating would have been most appropriately controlled by the power consumption of the heaters which were now dropped from the model. Instead, a separate heat flow model was set-up providing the temperature evolution at the wall of the deposition boreholes. This was not done with d^3f++ but with the code COMSOL /COM 13/. These temperatures were then incorporated as Dirichlet boundary conditions for the TH-model.

2.4.1 Pure heat flow model

Model domain

The heat transport model encompasses the same volume as the groundwater flow model. However, there are some differences in the model domains. As it is assumed that the structural difference between the skin zone and the matrix has no impact on heat flow. The thermal model does not differentiate between these two subdomains. In

the same way also the fractures are believed to be thermally "invisible" and do therefore not appear in the model.

While the flow model represents the pre-installation phase of the PR, heat can obviously only be introduced after the installation of heaters during the operational phase of the experiment. The deposition boreholes thus contain the heaters as well as compacted bentonite filling the remaining space of the boreholes. In the PR-tunnel backfill composed of a mixture of crushed rock and bentonite and the plugs made of highly compacted bentonite were installed. Simplifying the model, the plugs were treated like the backfill. The resulting model domain is depicted in Fig. 2.41. 73.435 volumetric elements were used for the numerical grid.
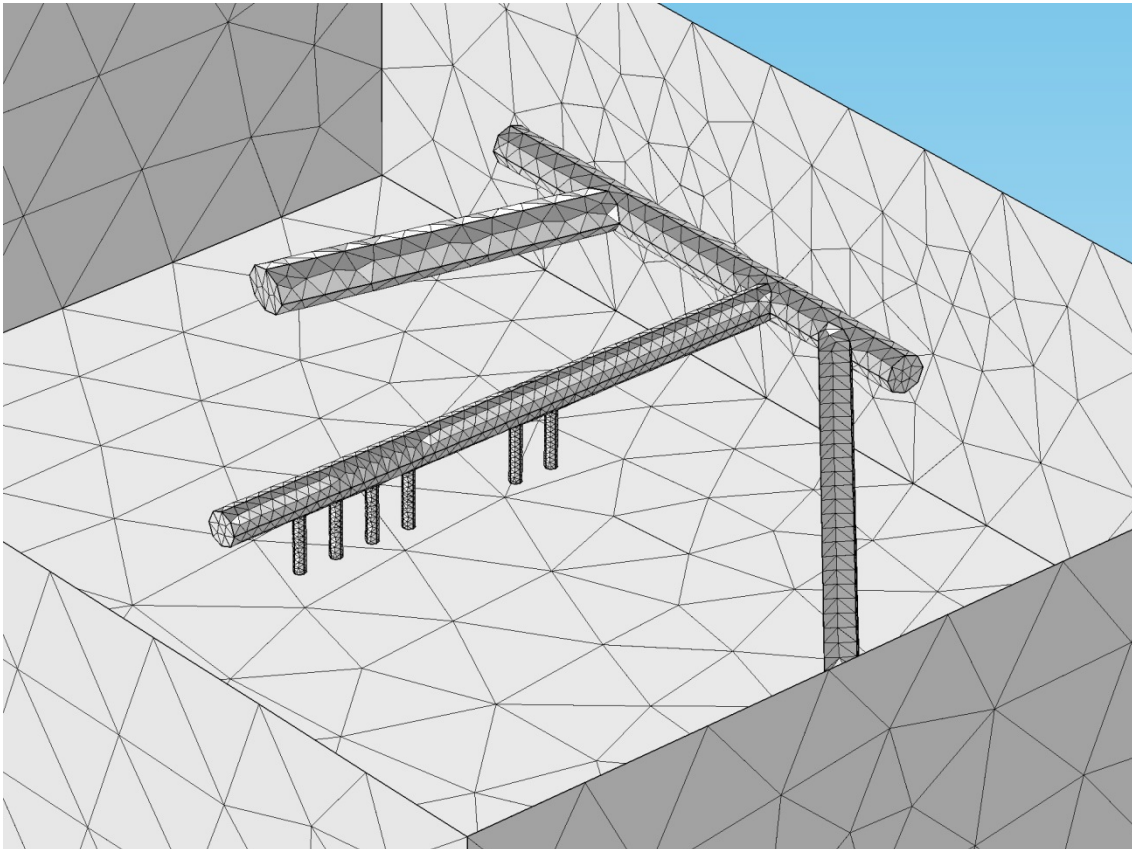
Fig. 2.41   Numerical grid of the thermal model

Thermal properties

Rock

After an extensive effort by /SUN 05/ to characterize the rock at the PR, the sensitivity analysis of the PR-site concerning temperature evolution by /KRI 07/ suggests a singular value of 2.72 W/(m K) as the relevant effective thermal conductivity for the rock. Heat capacities for the minerals constituting the rock types encountered at Äspö have been compiled and a mean weighted by volume fractions has been calculated /PAT 97/. The results for the different rock types are compiled in Tab. 2.20. They show very little variation so that a value of 770 J/(kg K) is assumed to be representative for all rock types. As the porosity of the rock is less than 1%, the impact of pore water on the bulk values of the thermal rock properties is considered to be negligible regardless of a possibly varying degree of saturation.

Tab. 2.20   Heat capacities at 25 °C; after /PAT 97/

Rock type	Mean value [J/(kg °C)]
Greenstone	775
Dioritoids	770
Quartz monzodiorite-granodiorite	760
Granodiorite-granite	755
Granite	740
All samples	755

Other materials

Besides the rock, four other subdomains can be differentiated by their different material properties: canisters, buffer, backfill and air. They are depicted in Fig. 2.42. The related material data was taken from /KRI 07/ except for the heaters and for air, the latter of which was of no concern in /KRI 07/. The data for copper provided by the COMSOL material data base[15](rho = 8700 kg/m³, λ = 400 W/(m K) and c = 385 J/(kg K)) was assumed to represent the canister material as /KRI 07/ also inserted values for copper from a different source.

---

[15]integrated in the code COMSOL

The I-, J-, G- and S-tunnel were assumed to be air-filled using the material "air" from the COMSOL data base which introduces automatically a temperature dependency of all three quantities. As the heat from the canisters barely reaches these three tunnels the referring values can be taken to be constants, though (rho ~ 1.23 kg/m³, λ = 0.024 W/(m K) and c ~ 1005 J/(kg K)). All thermal material data used in the heat transport model are compiled in Tab. 2.21.
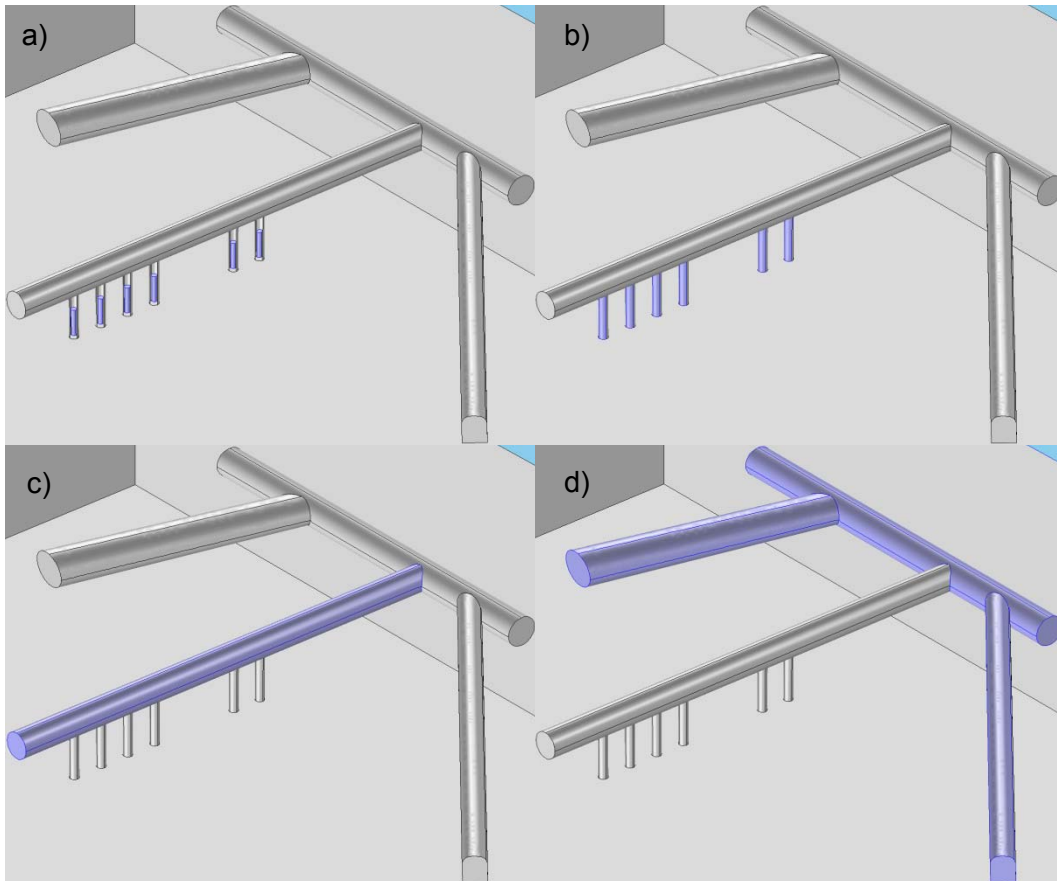
Fig. 2.42 Objects of different properties;a) canisters, b) buffer, c) backfill, d) air

Tab. 2.21 Material data for the heat transport model

Material	Thermal conductivity [W/(m K)]	Specific heat capacity [J/(kg K)]	Density [kg/m³]
granite	2.72	770	2770
air	$\lambda(T)$; ~ 0.024	$c_p(T)$; ~ 1005	$\rho(T)$; ~ 1.23
backfill	1.5	780	2500
bentonite	1.0	800	2780
copper	400	385	8700

□
□

Thermal initial and boundary conditions

In the thermal model the rock takes up heat from the six heaters in the deposition boreholes. Heat inflow is defined in the model by the power uptake of the respective heater where the power is equally distributed over its volume. A free outflow condition is assigned to the boundaries of the model domain. In the following, the heaters are labelled with the same number as the borehole where they have been emplaced. Each heater has its own history of power consumption as there were some failures, power reductions and also different starting times. The graphical log of power uptake is exemplarily given for heaters 1 and 6 in Fig. 2.43. Note that day 0 in the graphs of Fig. 2.43 refers to different dates. To simplify the input for the model the data were approximated by step functions. The simplified functions are depicted in Fig. 2.44 in their actual sequence. The background temperature at the Prototype Repository amounted to 15 °C /KRI 07/.
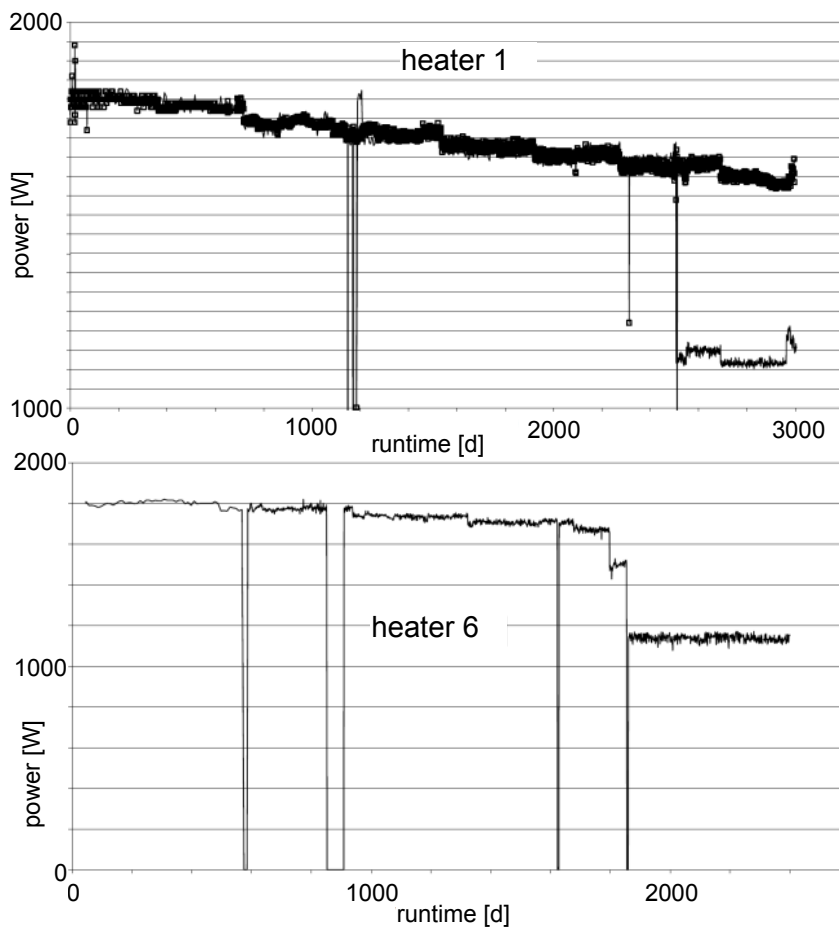
Fig. 2.43 Heater power consumption in deposition holes 1 and 6; from /KRI 10/
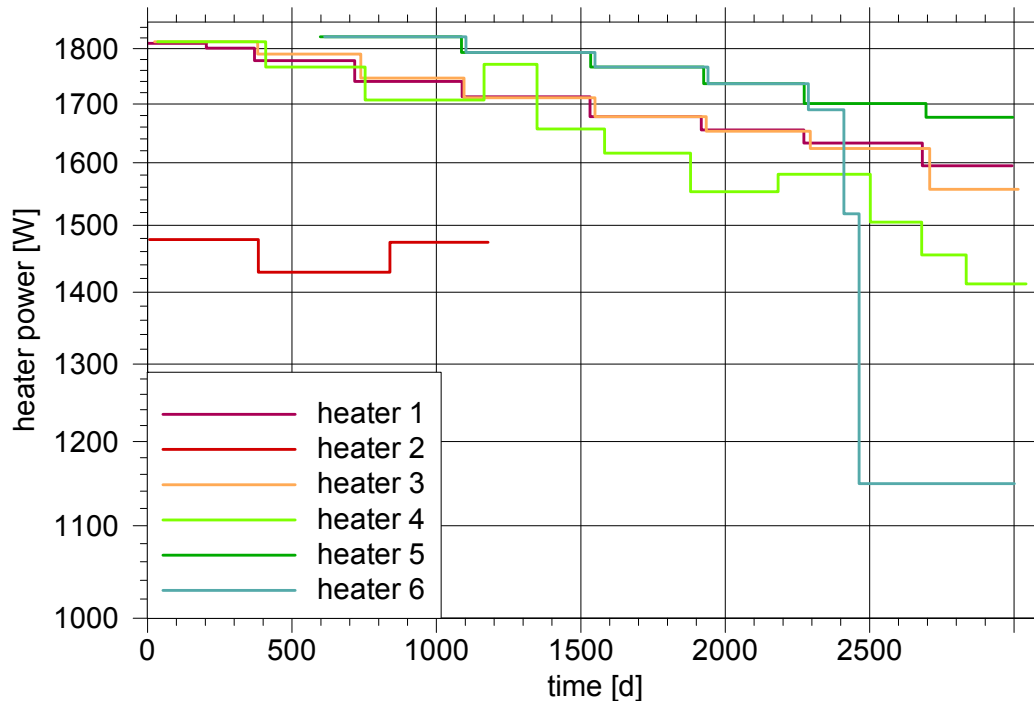
Fig. 2.44   Heater power consumption simplified for modelling

Calibration and results

The heat flow model was intended to be calibrated against continuous sensor data from the rock around deposition boreholes 5 and 6 as well as from the backfill in the tunnel above these boreholes. The position of the temperature sensors as well as the comparison of measured and calculated data are depicted in Fig. 2.45 for deposition hole 5 and in Fig. 2.46 for deposition hole 6. As it turned out, though, the achieved fit was good enough for the purpose at hand without any calibration

The biggest error of about 2-3 °C occurs at the bottom of the tunnel backfill above the deposition hole (TFA 04 in hole 5, cf. Fig. 2.45 c); TFA 13 in hole 6, cf. Fig. 2.46 c)) which is probably caused by a mistake in the model set-up. Compacted bentonite had been assigned to the top metre of the boreholes where the backfill material of the tunnel should have been. The backfill material has a 50 % higher thermal conductivity than the compacted bentonite which explains the comparatively slow temperature increase in the borehole close to the bottom of the tunnel. The resulting errors appear to be local, though, as the fit of measurement and calculation is much better already for the nearest sensor in the lower third of the tunnel cross-section.
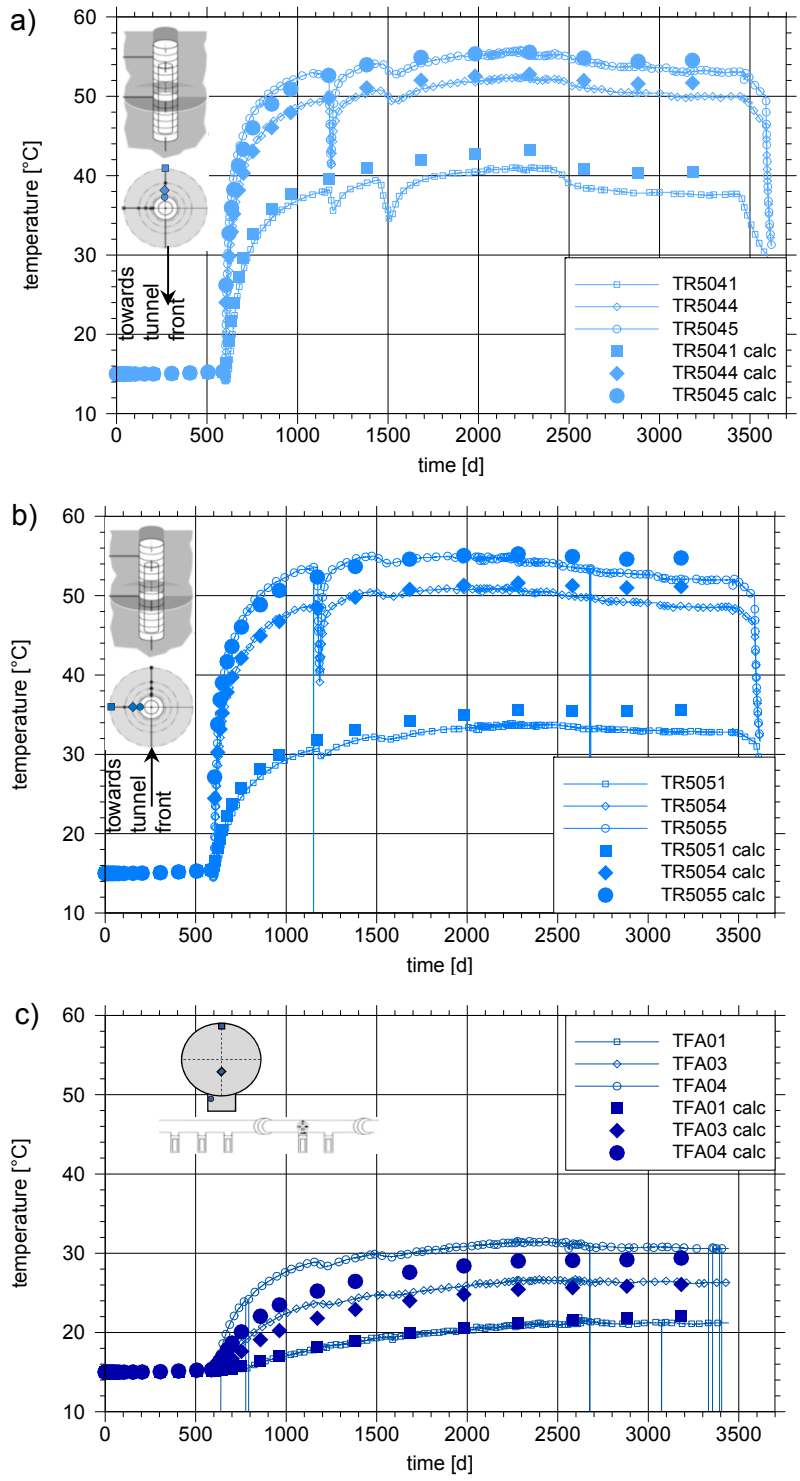
Fig. 2.45 Temperature development at some of the sensors in borehole 5;

a) sensors in the rock in the direction of the tunnel,

b) sensors in the rock orthogonal to the direction of the tunnel,

c) sensors in the backfill
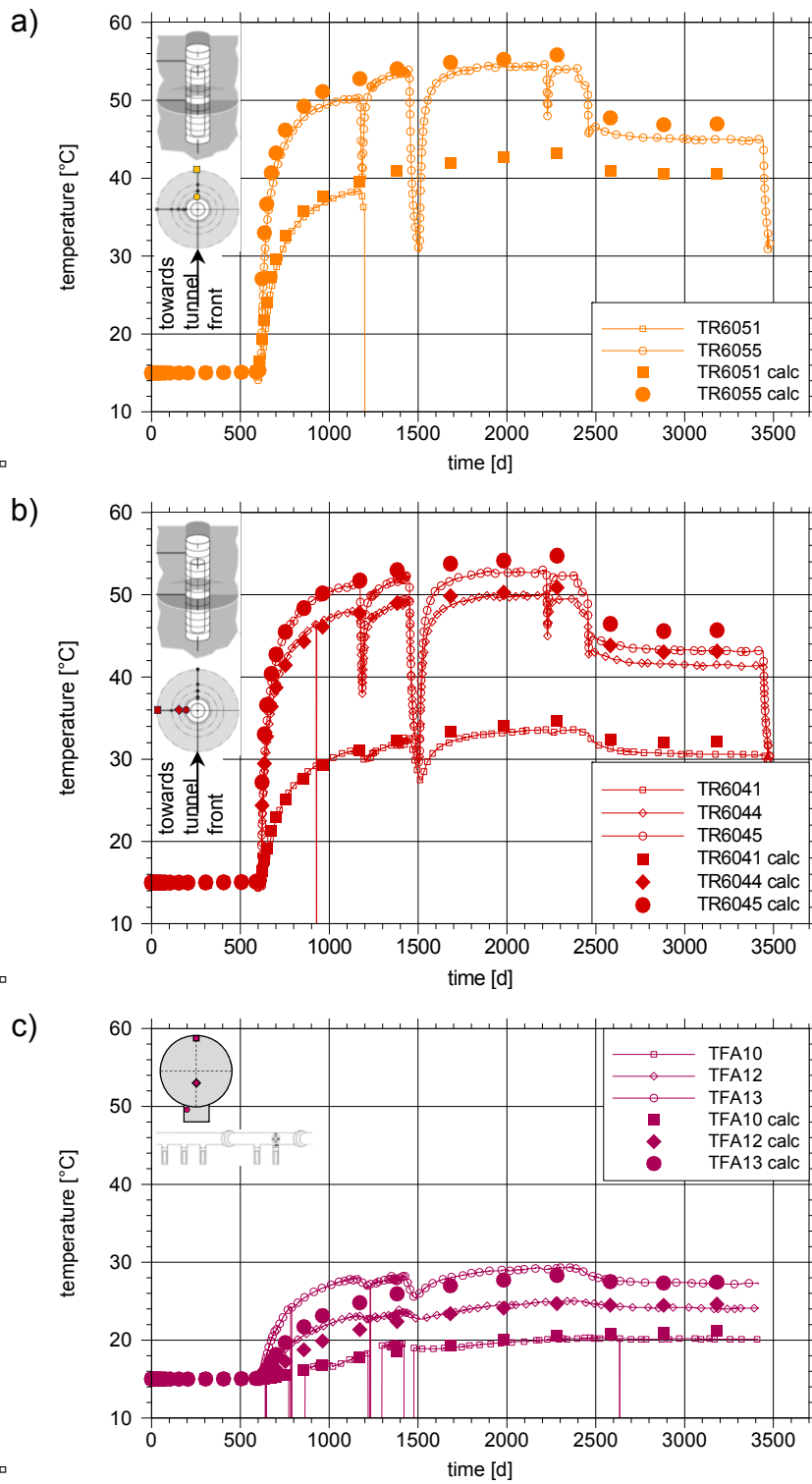
Fig. 2.46 Temperature development at some of the sensors in borehole 6;

     a) sensors in the buffer in the direction of the tunnel,

     b) sensors in the buffer orthogonal to the direction of the tunnel,

     c) sensors in the backfill

The resulting temperature distribution after 650 days – that is about 7 weeks after switching on the heaters 5 and 6 – are shown in Fig. 2.47. Significant temperature increase is rather limited to to the vicinity of the heaters. The plot is supplemented by Fig. 2.48 showing a vertical cross-section through heater 3 after 1100 days. This figure illustrates the transition between the rectangular heater area in this cross-section to the circular spreading pattern at a certain distance from the heater.
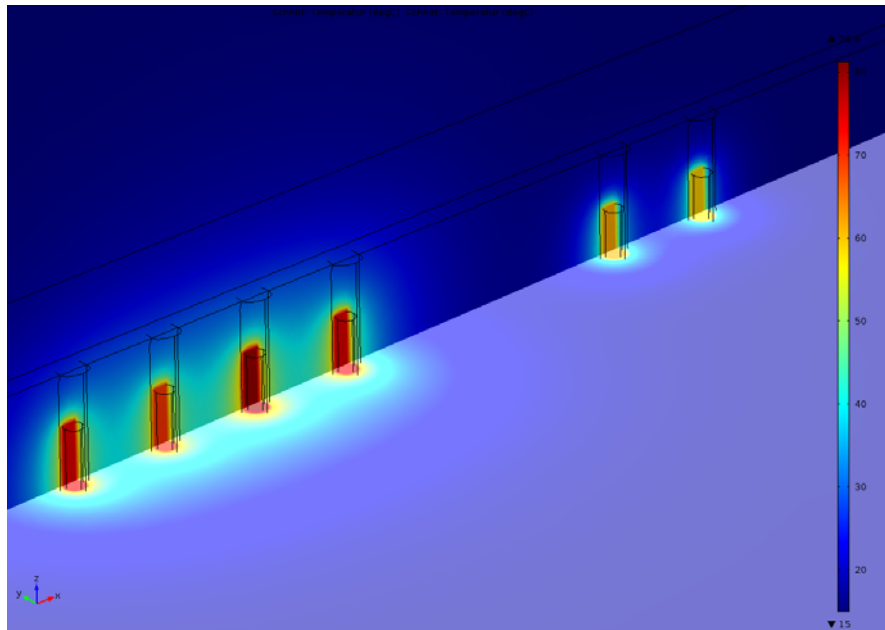
Fig. 2.47   Temperature distribution 650 days after switching on the first four heaters
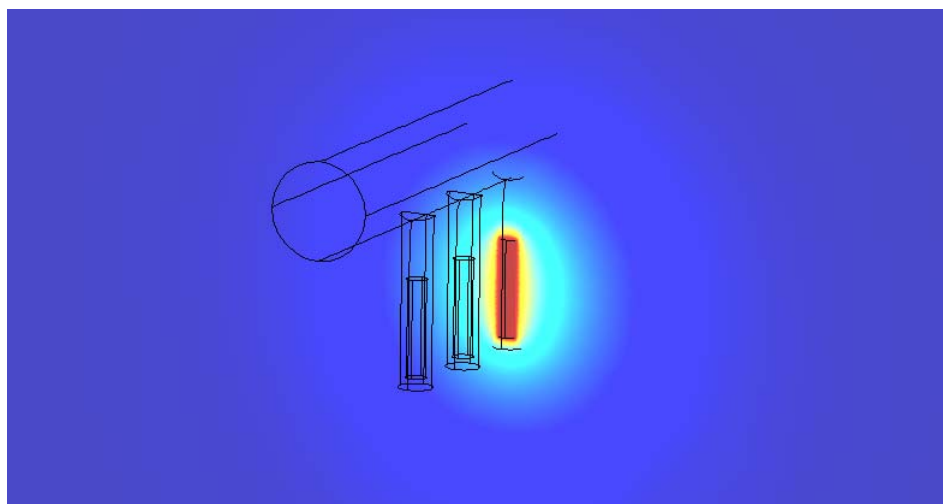
Fig. 2.48   Temperature distribution after 1100 days across heater 3

All in all, the results are already satisfying without further calibration. This conclusion corroborates in turn the validity of the simplifications of the geometry and the heat source data.

2.4.2   Thermo-hydraulic flow model

Model domain

(same as for the isothermal flow model, cf. section 2.3)

Material properties

Thermo-hydraulically coupled models require not only the hydraulic material properties described in section 2.3 and the thermal material properties given in section 2.4.1 but also temperature-dependent properties of the water, namely density and viscosity. Density was calculated after /OLD 98/ and viscosity after an ad hoc approach presented in /KRO 10/. A porosity value is additionally required with a view to heat transport in the groundwater. It was assumed to amount to 0.005 for the matrix as well as for the fractures.

State variables

As the maximum temperature in the thermo-hydraulic flow model is defined by the boundary conditions at the deposition boreholes whose evolution in time is depicted in Fig. 2.51, the temperature ranges between 15 °C and about 52 °C. The related water densities are 1017.5 kg/m³ and 991 kg/m³, respectively /IAP 03/, and $1.14 \cdot 10^{-3}$ Pa·s and $0.53 \cdot 10^{-3}$ Pa·s, respectively, /IAP 03/.

Initial and boundary conditions

Groundwater flow

(same as for the isothermal flow model, cf. section 2.3)

Heat flow

From the results of the heat flow model, the evolution of the temperature on the borehole surface was to be derived as a boundary condition for the thermo-hydraulic model. The required temperature distributions, however, are quite complex as indicated in Fig. 2.49.
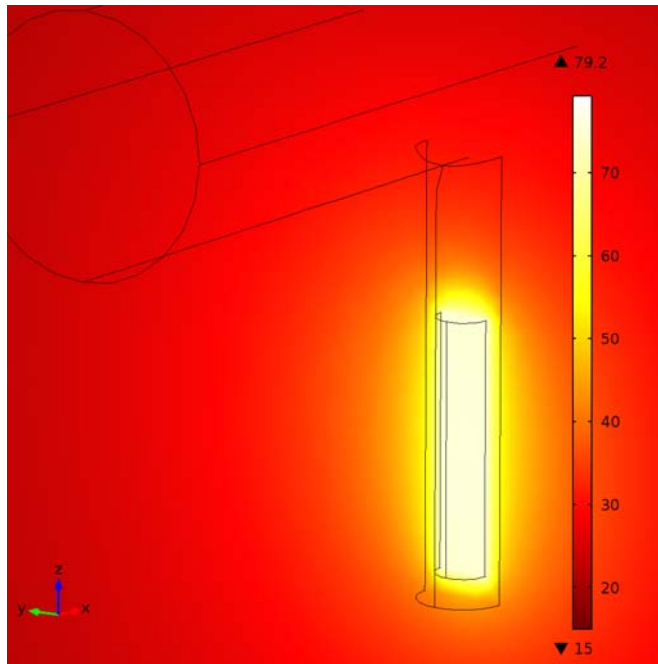
Fig. 2.49   Temperature in a vertical cross-section through heater 1 after 3000 days

While there clearly are distinct temperature differences in the vertical direction, the differences around the perimeter appear to be rather little. Fig. 2.50 shows the mean temperatures for deposition boreholes 1, 3, and 6 together with the mean temperatures along four vertical line segments that lay either in the direction of the tunnel or orthogonal to the tunnel axis. The maximum difference of the mean temperature in the vertical line segments does not exceed 3 °C for each borehole. Since only an indication of the influence of temperature on the flow field was sought, the mean temperature on the borehole surface was adopted as a thermal boundary condition.

From the results of the heat flow model, the evolution of the mean temperature on the borehole surface could have been easily derived by a post-processing procedure in COMSOL. The resulting data shown in Fig. 2.51 were then used as input for the ther-

mo-hydraulic model. The initial temperature of 15 °C was chosen to be the same as for the heat flow model.
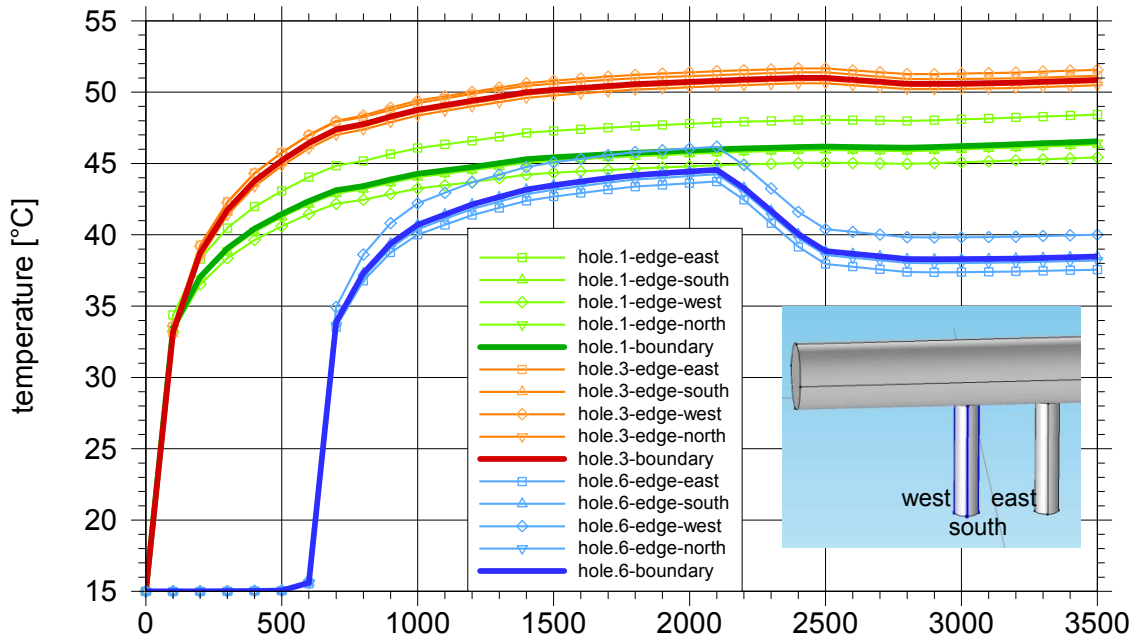
Fig. 2.50   Temperatures in boreholes 1, 3, and 6;

mean values along 4 vertical line segments per borehole (thin curves) and mean value on the surface (thick curves)
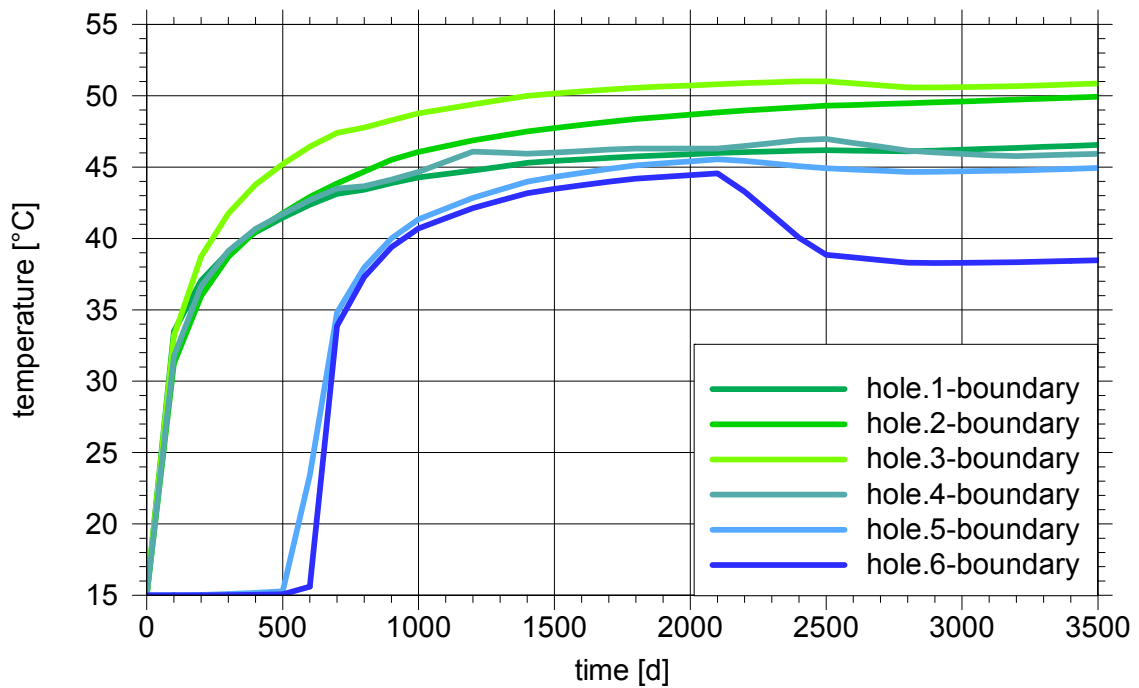
Fig. 2.51   Temperature evolution on the surface of the deposition boreholes

Boundary conditions

The thermo-hydraulic model was executed as a thermo-haline calculation where the salt concentration was set to zero everywhere at every time. In principle there are therefore three sets of boundary conditions as depicted in Fig. 2.52:

outer model boundary:

    prescribed pressure

    rock temperature (T = 15 °C)

    no salt

tunnel surface

    atmospheric pressure

    temperature outflow

    salt outflow

borehole surface

    atmospheric pressure

    temperature evolving according to the heat flow model

    salt outflow

$p(x,y,z)$ prescribed surface pressure
$T_{(t)}$ prescribed surface temperature

$p_0=1$ bar   atmospheric pressure
$T_0=15°C$ temperature of undisturbed rock
$c_0=0$ initial & boundary concentration

T_{out},c_{out} outflow boundary conditions
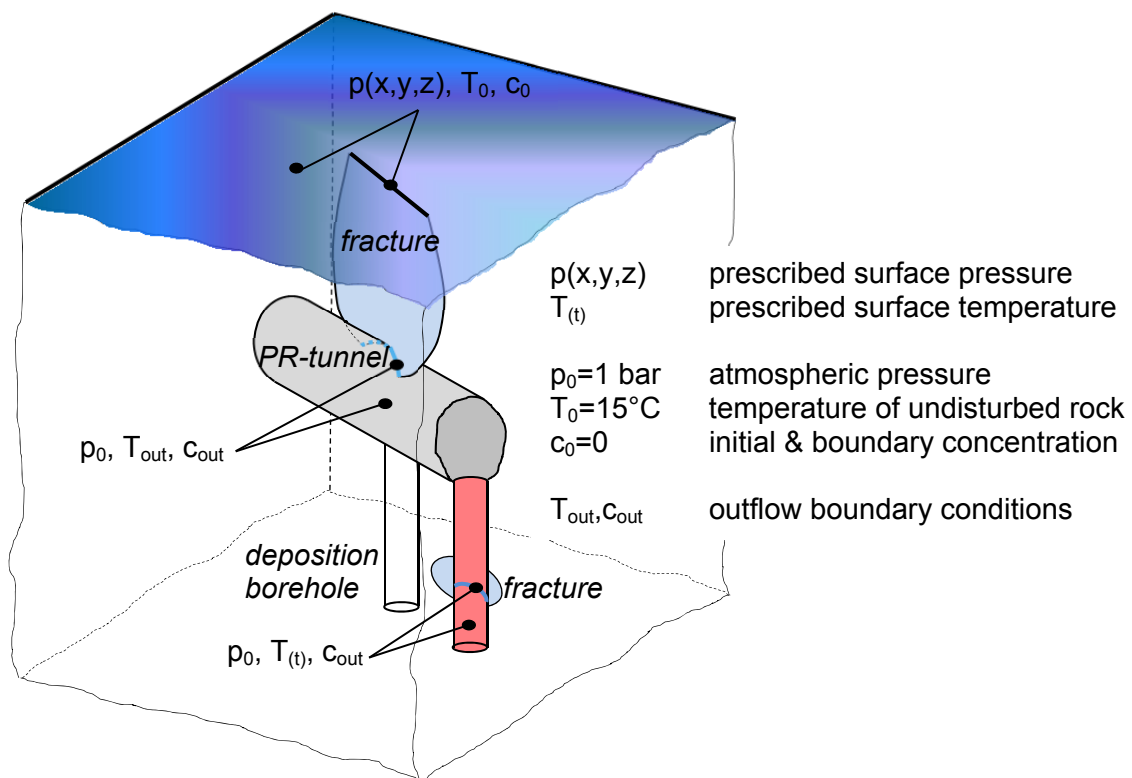
Fig. 2.52   Boundary conditions for the thermo-hydraulic model

Calibration targets

This model was set up for demonstration purposes only. Calibration was therefore not performed.

Results

The results of the model are given in terms of composite plots containing information about the calculated temperature as well as the velocity field. The temperature distribution is given as a transparent colour plot in a vertical cross-section through the PR. The velocity field is represented by velocity vectors in the same cross-section which are coloured to indicate their absolute value. Fig. 2.53 to Fig. 2.56 show the whole PR, Fig. 2.57 to Fig. 2.59 a close-up of section 2 containing deposition boreholes 5 and 6 where the cluster of minor fractures M2 to M6 is located. To facilitate comparison, each series of figures is drawn from the same perspective.

The two plots in Fig. 2.53 represent the isothermal steady-state solution for reference. Also for reference, the position of the fractures are indicated in the top plot but not shown further on as they tend to be confusing in the plots. Especially labelled are the three minor fractures with the highest permeability: M1, M2, and M6.

Fig. 2.54, Fig. 2.55, and Fig. 2.56 illustrate the evolution of the temperature and the related changes in the velocity field by showing model results for the whole PR at 300, 900, and 3600 days model time, respectively. For the same points in time the close-up of heaters 5 and 6 is depicted in Fig. 2.57 to Fig. 2.59.

The strongest influence of the heating on fracture flow is not observed in the major but in the minor deterministic fractures because the thermal influence of the heaters on the rock temperature is spatially rather limited. The major fractures therefore see hardly any significant temperature increase. The minor fractures, by contrast, are even cutting through the deposition holes so that heating causes a maximum impact on fracture flow by decreasing the water viscosity and consequently decreasing the hydraulic resistance to flow. This is best seen in the temporal evolution of the flow velocity in the vicinity of minor fractures M2 and M6 at the deposition holes 5 and 6 (cf. Fig. 2.53) as shown in close-ups in Fig. 2.57 to Fig. 2.59.
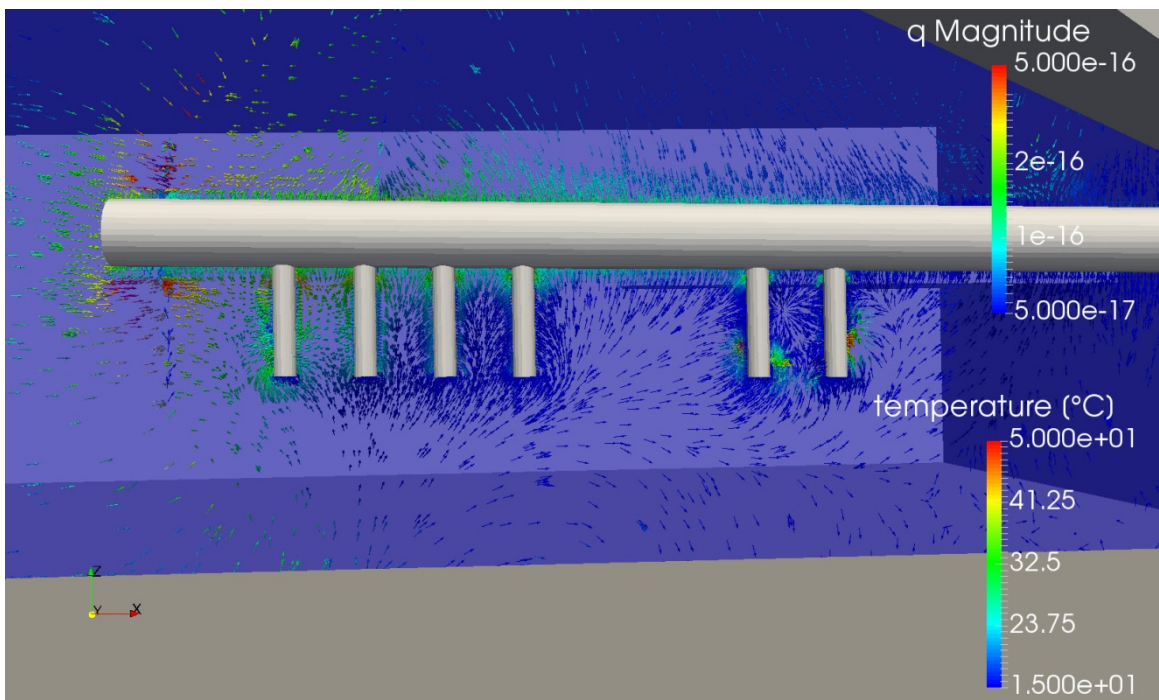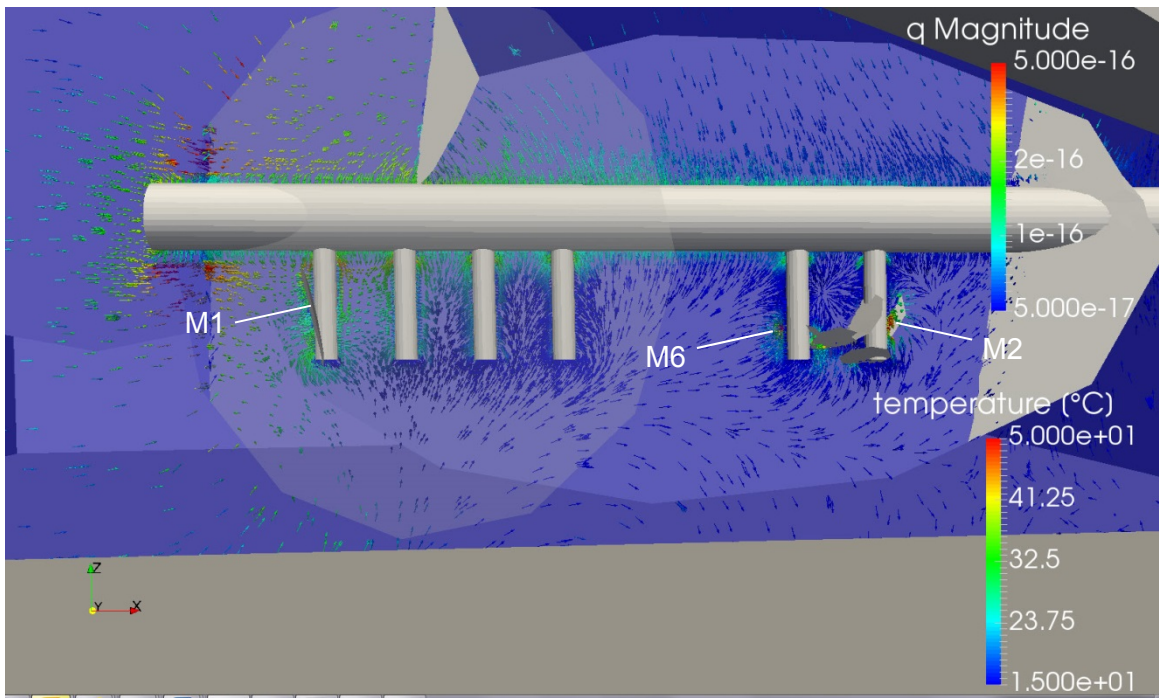
Fig. 2.53   Isothermal, steady-state flow in a vertical cross-section
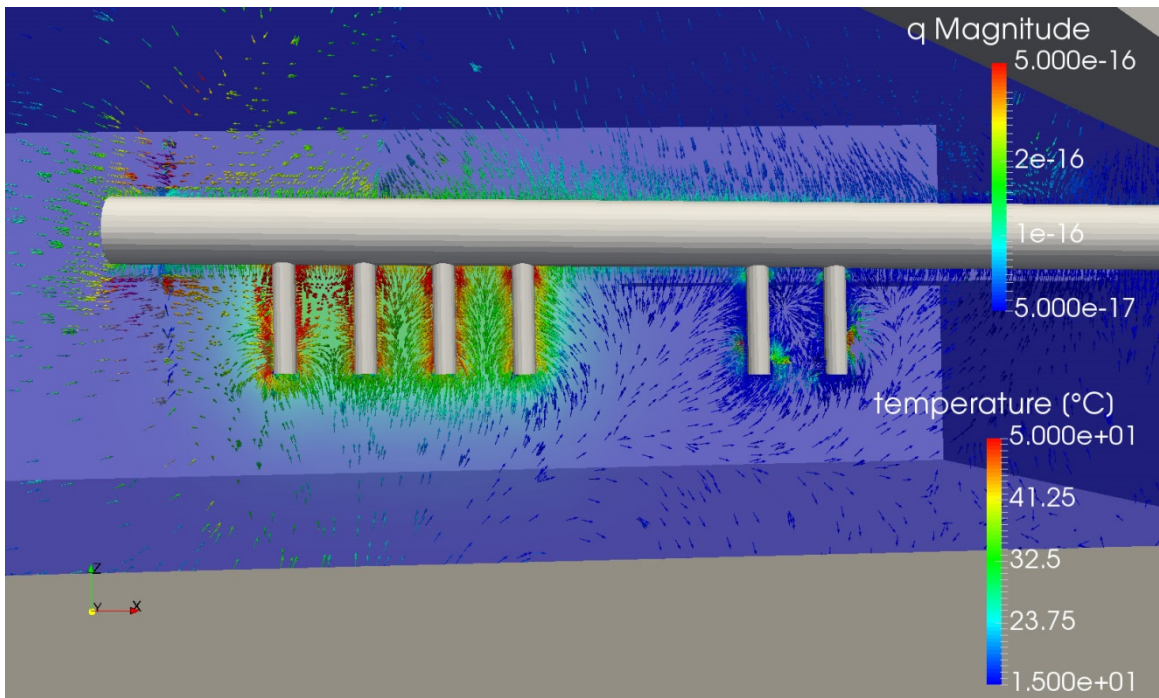
Fig. 2.54   Temperature and flow field in a vertical cross-section after 300 days
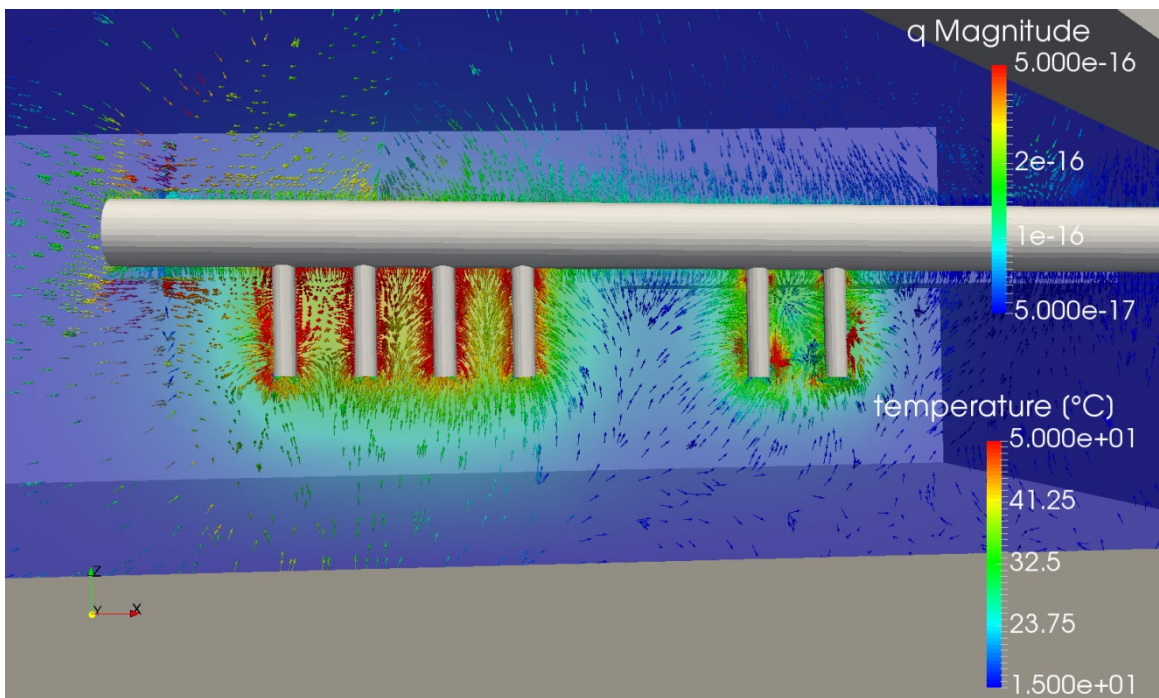
Fig. 2.55   Temperature and flow field in a vertical cross-section after 900 days
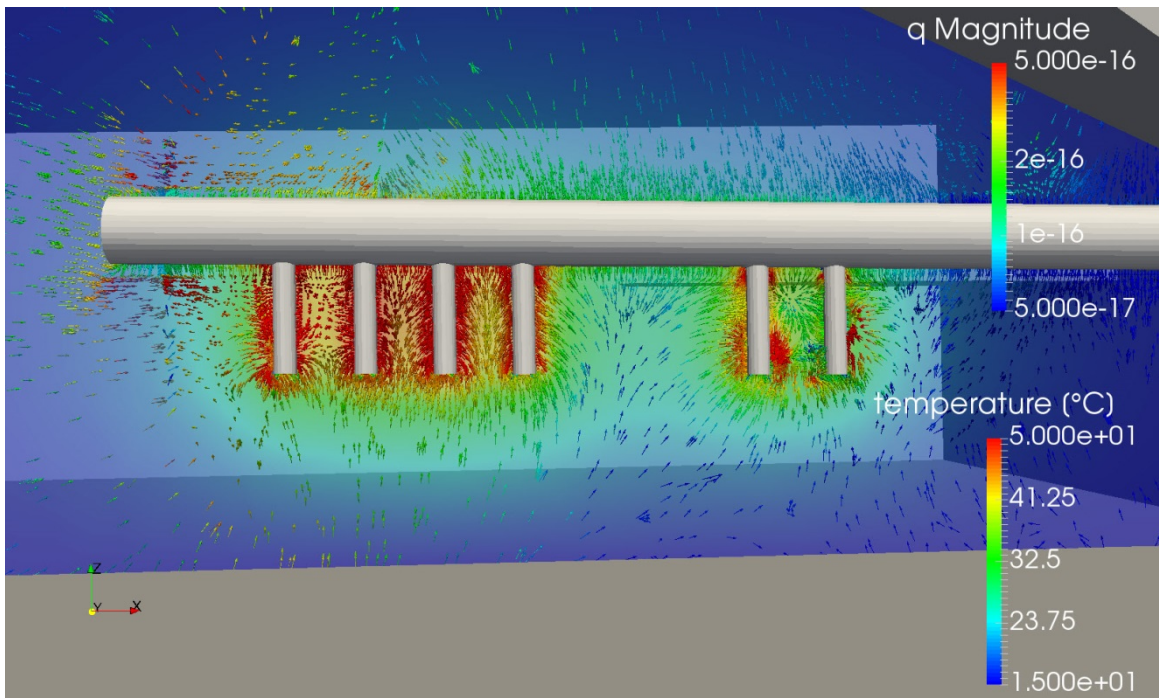
Fig. 2.56   Temperature and flow field in a vertical cross-section after 3600 days
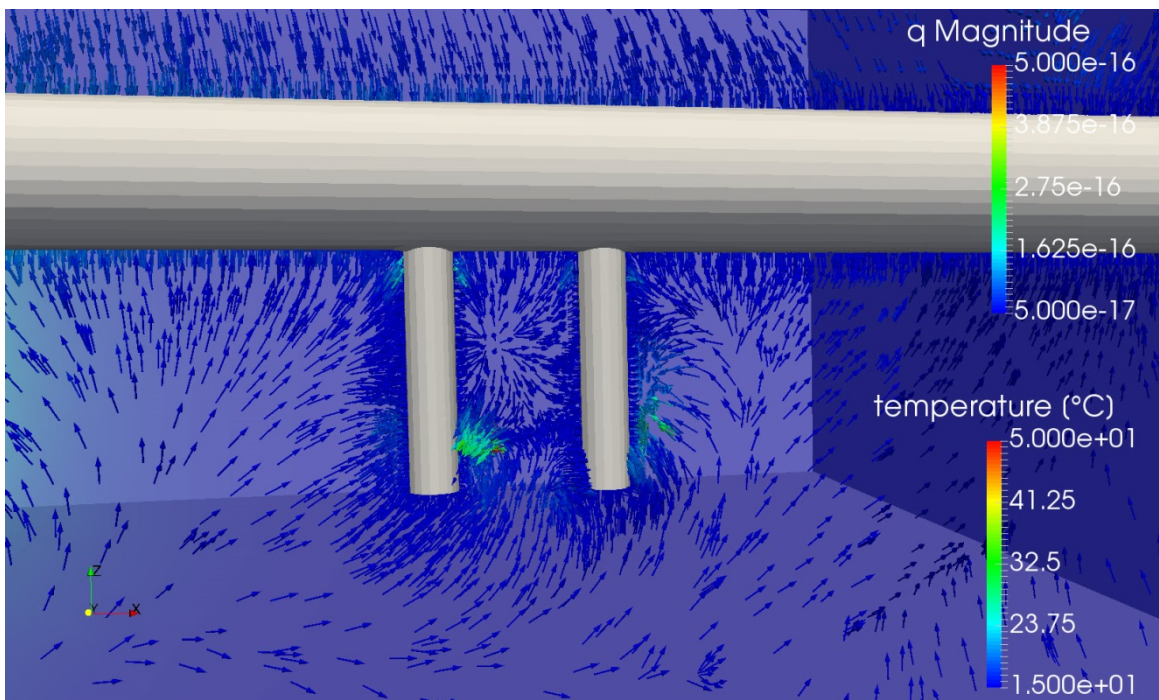
Fig. 2.57   Temperature and flow field in a vertical cross-section after 300 days
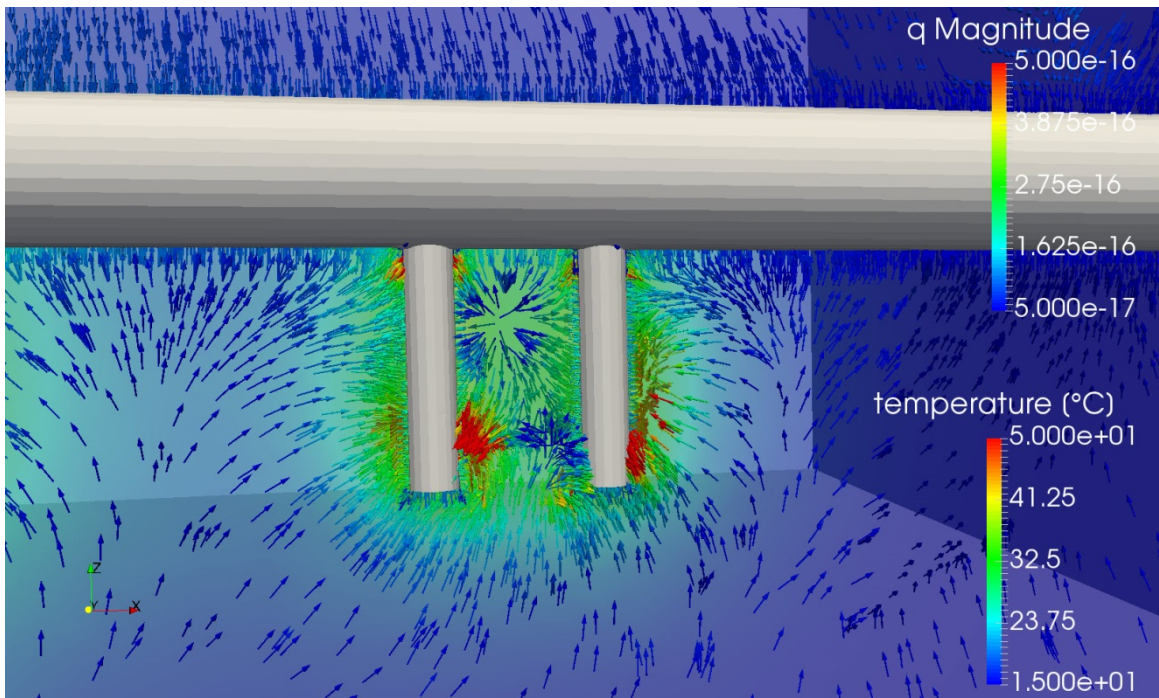
Fig. 2.58 Temperature and flow field in a vertical cross-section after 900 days
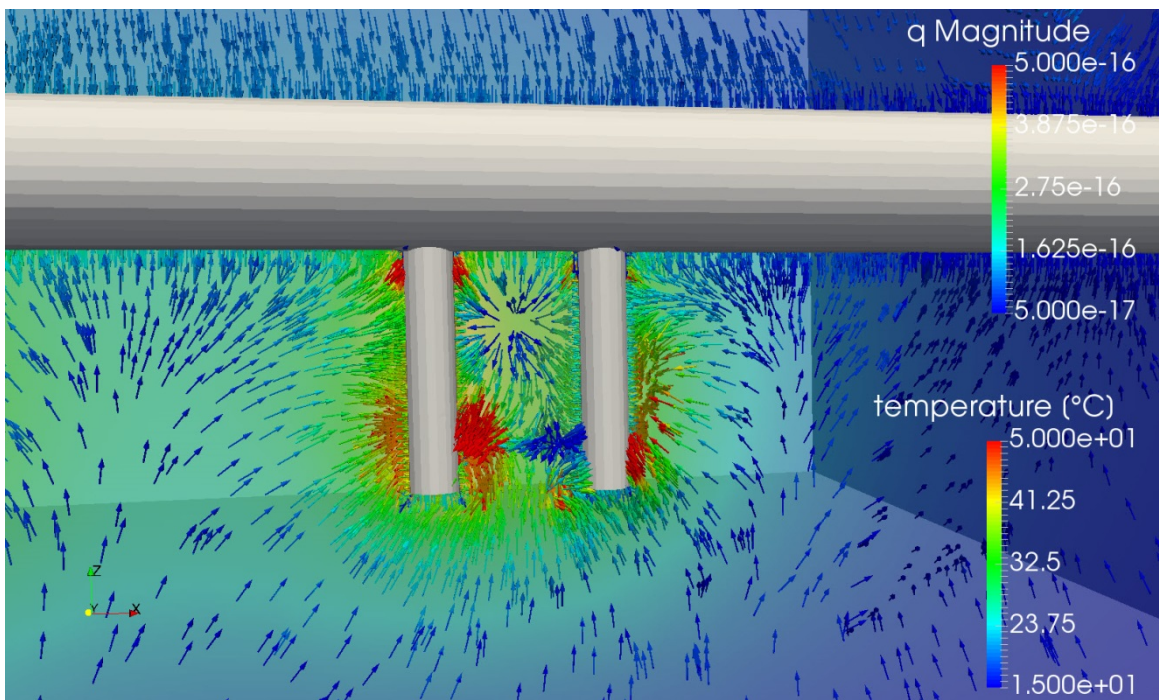
Fig. 2.59 Temperature and flow field in a vertical cross-section after 3600 days

Discussion

–   Intersection of fractures with tunnel and boreholes were determined from the out-flow measurements reasonably accurate. Size and orientation, however, were in some cases quite off. A comparison of the model results presented here with those from a model that was based on the initially conceived fracture system would have been telling something about the benefit from the knowledge of the actual fracture system.

–   The outflow profile along the PR-tunnel as well as total outflow into the deposition holes could be reproduced with minor modifications on the conceptual basis derived from modelling the BRIE. This confirms the idea of treating the background fractures as a continuous porous medium that adds to the flow of the much less permeable matrix.

–   The isothermal flow model demonstrated again the ability of code d^3f to reproduce a strong discontinuity in the flow field of the matrix that can be introduced by a lower-dimensional fracture. Moreover, some unexpected results came from the modelling that could nevertheless be reasonably explained in hindsight. This includes the in some cases much higher flow velocity at the rim of a fracture compared to its face as well as the influence of the skin at the intersections of tunnel and deposition holes.

–   The straight forward flow field that basically stretched from the outer model boundaries to the geotechnical openings suggests that the effort of reproducing the pressure boundary conditions by inverse distance weighing would not have been necessary. Instead, a rough averaging would probably have done almost quite as well. The increase of temperature due to a thermal load equivalent to the expected heating power of waste canisters was calculated with a heat flow model. The resulting temperatures matched the measured temperatures very well. The model shows that a noticeable temperature increase reached after ten years of heating only about ten metres from the deposition holes into the rock.

–   Since the thermo-hydraulic model did not contain heaters or buffers, it could not meet the true conditions during the operational phase of the experiment. Moreover, direct flow measurements were not possible in the experiment, meaning that the model results can only be of orientating character.

3 Heat flow – Borden field research site

3.1 Introduction

The Borden field research site is located at the Canadian Forces Base (CFB) Borden, approximately 80 km northwest of Toronto, Ontario, Canada, about 350 m north of a landfill that operated from 1970 to 1976. The highly permeable, unconfined aquifer consists of horizontal, discontinuous layers of medium-grained, fine-grained, and silty fine-grained sands /PAL 92/. CFB Borden is an extremely well-studied site, and numerous experimental studies took place here.

A thermal injection and storage experiment was conducted 1983/1984 to investigate the feasibility of storing thermal energy in shallow unconfined aquifers near the water table. In this experiment, a volume of 53.3 m³ of heated water was injected through an injection well in a depth between 3.3 m and 5.3 m below ground surface over a time period of 6 days. The injected water was drawn from a well located 60 m to the west of the injection well. During the whole storage period of 135 days groundwater temperatures were measured throughout a detailed 3d monitoring network /PAL 92/.
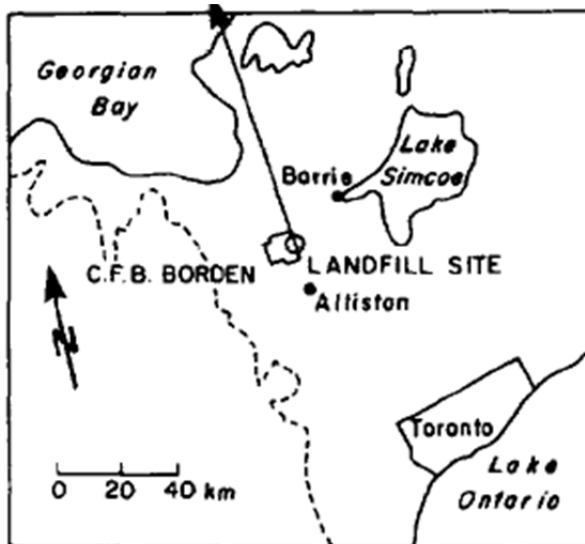
Fig. 3.1 Location of the Borden thermal injection experiment, /PAL 92/

The experiment allows the quantification of coupled physical processes as advective heat transport by fluid flow and heat conductance in the fluid-matrix-system. Therefore, based on the injection experiment, a 3d numerical experiment was performed. /MOL 92/ describes the development of a coupled density-dependent groundwater flow

and thermal energy transport model and the reproduction of the experimental data described in /PAL 92/ to validate the numerical model.

The subject of this work is the simulation and reproduction of the results of /MOL 92/ using d³f++.

3.2   The Model Description

The thermal transport problem is described by the Darcy equation, the continuity equation for the fluid, and the continuity equation for the heat /MOL 92/.

The Darcy equation describes the density-driven groundwater flow:

$$\mathbf{q} = -\frac{k}{\mu}\nabla p - \rho\mathbf{g}, \tag{3.1}$$

where $\mathbf{q}$ is the Darcy velocity of the fluid, k is the permeability of the medium, μ is the viscosity of fluid, which is dependent on the temperature T, ρ is the temperature dependent fluid density, p is the static pressure of the fluid, and g is the gravitational acceleration. The static pressure can be replaced by the equivalent freshwater head h^*,

$$h^* = \frac{p}{\rho_0 g} + z, \tag{3.2}$$

where ρ_0 is a reference freshwater density, z is the elevation above a datum.

The continuity equation for the fluid has the form

$$\partial_t(\phi\rho) + \nabla \cdot (\mathbf{q}\rho) = s, \tag{3.3}$$

where ϕ is the porosity of the media, s is the source of the fluid.

The continuity of heat in porous media is given by

$$\frac{\partial T}{\partial t} + \phi\frac{c_f \rho_f}{\bar{C}}v_f \cdot \nabla T - \nabla \cdot \left(\frac{\bar{\lambda}}{\bar{C}} + \phi\frac{c_f \rho_f}{\bar{C}}\boldsymbol{D_{mf}}\right) \cdot \nabla T = 0, \tag{3.4}$$

80

Where $\bar{C} = \phi\rho_f c_f + (1 - \phi)c_s\rho_s$ is the average specific heat of the whole system, $\bar{\lambda} = \phi\lambda_f + (1 - \phi)\lambda_s$ is the average thermal conductivity, c_f, c_s are the specific heat of the water and matrix solid, ρ_f, ρ_s are the density of the water and the matrix solid, respectively.

3.3   The Model Domain and Boundary Conditions

The three dimensional model domain and the flow boundary conditions are shown in Fig. 3.2. The domain dimensions are 40 m x 30 m x 20 m in the x, y and z directions, respectively. An injection well was placed between the point (12 m, 15 m, 14.7 m) and the point (12 m, 15 m, 16.7 m) with a length of 2 m, and warm water with temperature of 37°C was pressed into the domain with an injection rate of $1.04 \, l/s$ for 6 days. (Note that here the southwest corner represents the origin of coordinates, where it is represented by the injection well in /MOL 92/. For comparison purposes in Fig. 3.14 to Fig. 3.20 the origin is transformed to the well.)
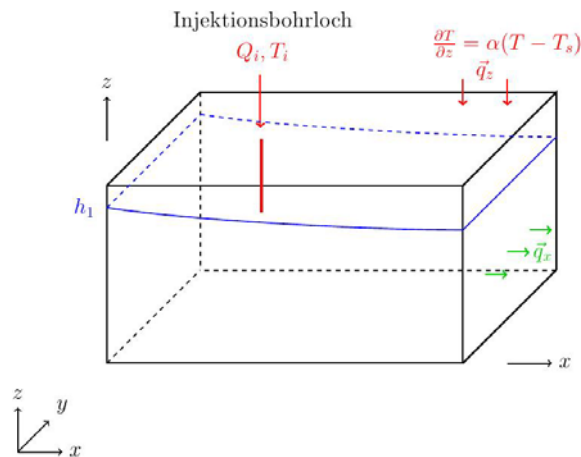
Fig. 3.2   Three dimensional model domain and boundary conditions.

For the groundwater flow, the southern, the northern und the bottom boundaries were assumed to be impermeable (Neumann boundary condition). At the western boundary, a hydrostatic pressure was applied (Dirichlet boundary condition). A constant outflow velocity (outflow boundary condition) was assigned to the eastern boundary. At the top, a uniform recharge rate was applied across the model surface. The free groundwater surface or water table was to be determined by the program d³f++.

For the heat transport, no heat exchange was assumed at the southern, the northern and the bottom boundaries (Neumann boundary condition). At the western boundary,

the temperature was kept at the initial temperature (Dirichlet boundary condition). At the eastern boundary, the heat is supposed to leave the model with the fluid (outflow boundary condition). At the top boundary, a thermal flux was applied, which is linearly dependent on the temperature difference between the observed air temperature und the computed aquifer temperature (Cauchy boundary condition). The required transient air temperatures for the boundary condition were obtained from /MOL 92/ using a si-nusoidal function, shown in Fig. 3.3.
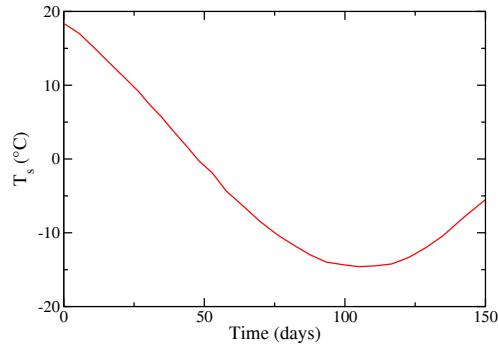
Fig. 3.3　　Input air temperature for the boundary condition

3.4　　Initial Conditions and Model Parameters

As described in /MOL 92/, a uniform vertical temperature gradient was assumed within the longitudinal cross section, based on observations prior to the thermal injection in the field experiment region. At the bottom of the aquifer, the initial temperature was 8.25°C increasing linearly to 10°C at z=13.5 m (6.5 m under the ground surface). Thereafter, the temperature increased linearly to 17°C near the ground surface. The initial temperature in a vertical longitudinal cross-section is shown in Fig. 3.4.
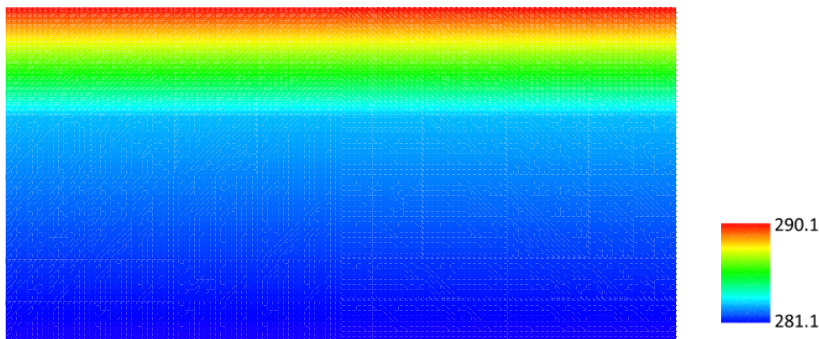
Fig. 3.4　　Initial temperature distribution (in K) in a vertical cross- section

The initial pressure was linearly dependent on z, and reached zero at ground level. In case of a free groundwater surface, the initial water level is 2 m below earth's surface.

The thermal parameters for the model were obtained from /MOL 92/ and listed in Tab. 3.1. The fluid density was assumed to be dependent on the temperature, using an ad-hoc formulation /KRO 10/:

$$\rho(T) = 999.974 - \left(\frac{T}{12.1} - 0.28\right)^2 + \left(\frac{T}{34}\right)^3 - \left(\frac{T}{78}\right)^5 + \left(\frac{T}{120}\right)^7, \qquad (3.5)$$

where T is the temperature in °C. The water viscosity was also supposed to depend on the temperature /KRO 10/,

$$\mu(T) = \mu_0 \cdot \left\{\frac{3.5}{(17 \cdot \theta + 575)^{1.18}} + 6 \cdot 10^{-5} \cdot \left(\frac{T}{200}\right)^2 - 1.2 \cdot 10^{-4}\right\}, \qquad (3.6)$$

where $\mu_0 = 1.787 \cdot 10^{-3}$ Pa s, as given in Tab. 3.1, and T is the temperature in °C.

3.5   Numerical Results

The code d³f++ is able to solve the fully coupled system of equations including the free surface and heat transport, but it cannot take into account the heat conduction above the water table, that means outside the model domain. Therefore two problems are treated separately: the groundwater flow problem with the free water surface without heat transport, and, at the other hand, the flow and heat transport problem in a confined aquifer.

Tab. 3.1   Thermal transport parameters: Parameters of the numerical model

Parameter	value
effective porosity ϕ	0.35
permeability k	$9.209 \cdot 10^{-12}$ m²
molecular diffusion D_m	$6.0 \cdot 10^{-10}$ m² s^{-1}
longitudinal dispersivity α_L	$1.0 \cdot 10^{-1}$ m
transverse dispersivity α_T	$1.0 \cdot 10^{-2}$ m

reference water density ρ_0	1000 kg m^{-3}
rock density ρ_s	2630 kg m^{-3}
specific heat of water c_w	4174 J kg^{-1} °C^{-1}
specific heat of rock c_f	2630 J kg^{-1} °C^{-1}
aquifer thermal conductivity λ	2.0 J m^{-1} s^{-1} °C^{-1}
viscosity μ_0	1.787·10^{-3} Pa s
recharge rate q_z on the top	6.342·10^{-9} m s^{-1}
outward flux q_x on the east side	4.693·10^{-7} m s^{-1}
source temperature	37.0 °C
source injection rate	1.03·10^{-4} m^3 s^{-1}
injection period	6 days

3.5.1 Free surface of water

The free surface model of the Borden site was set up without heat transport. The 3d coarse grid (level 0) is shown in Fig. 3.5. The grid can be refined to different levels. At the western boundary, the water head was kept at 2 m below ground surface, and at the eastern boundary an outflow with a uniform velocity of 4.693·10^{-7} m s^{-1} was defined. At the top boundary a recharge rate of 6.342·10^{-9} m s^{-1} specified. The result is shown in Fig. 3.6. After a short time an equilibrium with an almost horizontal water surface was reached. The water was almost horizontally flowing from the western boundary to the eastern boundary, whereas the velocity at the west boundary was a little higher.
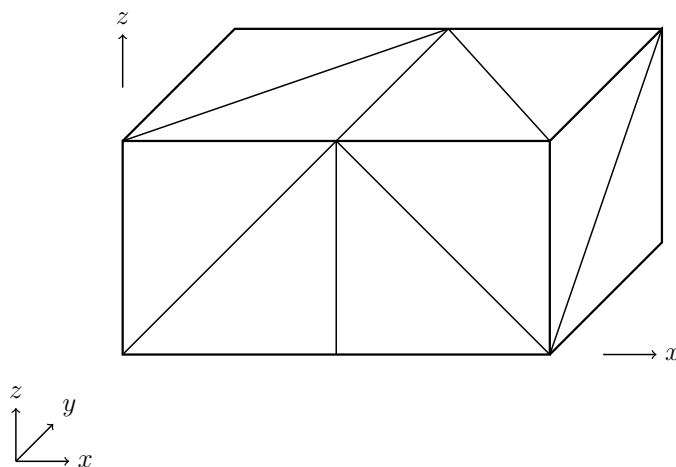
Fig. 3.5   3d coarse grid
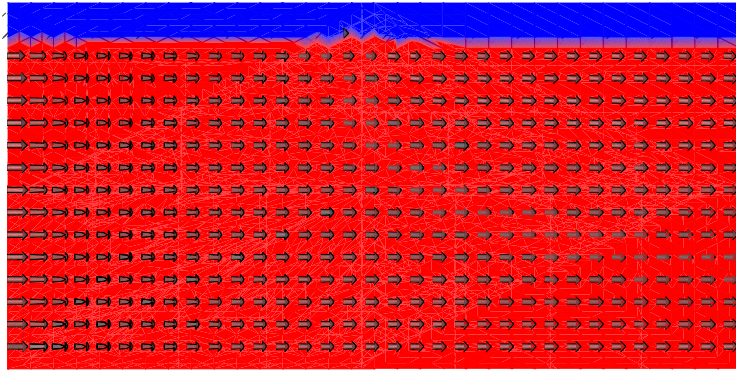
Fig. 3.6   Free groundwater surface at Borden in a x-z cross section at y=15 m

3.5.2   Flow and Heat transport

Flow and heat transport were simulated in a confined aquifer. The coarse grid is shown in Fig 3.5, which was the same as for the groundwater flow with free surface. The grid was refined to different refinement levels.

At the beginning of the project, the boundary condition for the upper boundary was not yet completely implemented. A constant thermal flux could be applied, but not a thermal flux that is linearly dependent on the temperature difference between the observed air temperature und the computed aquifer temperature (Cauchy boundary condition).

In the first trial run, thermal fluxes were applied, which remained constant for a certain period of time. Later, the fluxes were estimated from the derivative of the background aquifer temperature with respect to the depth of the aquifer based on Fig. 9 in /MOL 92a/. The estimated values listed in Tab. 3.2 were used for the simulations.

Tab. 3.2   Thermal flux estimated from Fig. 9 of /MOL 92a/

Time (days)	Flux ($°C \cdot m^{-1}$)
0	0
3	0.30243192
7	0.29654471
14	-1.2342228
21	-0.9903334
25	-1.7333044
32	-1.6857576

45	-2.4652879
56	-1.8343238

A simulation result of flow and transport is shown in Fig 3.7. Warm water with a temperature of 37°C was injected dot-like with a rate of $1.03 \cdot 10^{-4}$ m^3 s^{-1} at the point (x=12 m, y=15 m, z=16 m) during the first 6 days. During injection, the heated water flowed radially from the injected point, thereby dominating over the global flow from west to east. After 6 days, the injection of warm water was stopped and the heat spread further in the domain. In the meantime, the centre of the heat mass moved slowly eastward. In the simulations, a time step of 0.2 days was used. These conditions were maintained for all other models in the following if not stated otherwise.
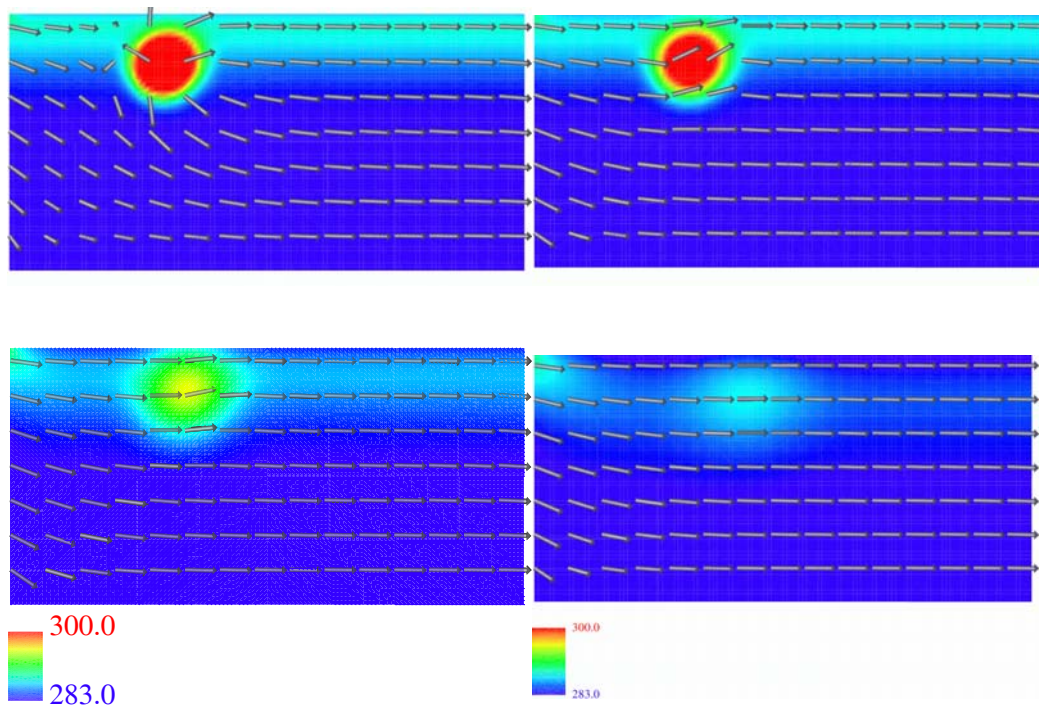
Fig. 3.7   Flow and heat distribution ina x-z cross section at y = 15 m at times t=6, 9, 27, and 76 days at refinement level 6 (temperature in K)

3.5.3   Convergence Test of the 3D-models

In the simulation, the grid can be refined to different degrees of refinement, called levels. This allows to investigate the grid convergence of the simulation results. The coarse grid shown in Fig. 3.5 has just 12 elements. With each additional refinement level, the number of resulting elements increases by a factor of 8. The coarse grid was refined to refinement levels = 4, 5, 6, and 7, respectively. The resulting numbers of el-

ements as well as the minimum and maximum length of the edges are listed in Tab. 3.3.

Tab. 3.3   Characteristic 3d-grid data for different refinement levels

refinement levels	elements	minimum edge (m)	Maximum edge (m)
4	49152	1.25	2.577
5	393216	0.625	1.288
6	3145728	0.3125	0.6442
7	25165824	0.15625	0.3221

Compared were the results at the end of warm water injection. Basis for this as well as for all subsequent comparisons are the temperature isolines of 30°C in the x-z cross section (y=15 m). Surprisingly, in the first Simulations, no clear convergence was observed after increasing the number of refinement levels. Checking the grids revealed that refinement level 6 produced already a much finer mesh than the grids used in /MOL 92/. The simulation results should thus already be convergent at this degree of refinement. In order to preclude an error in the code, the simulations were repeated with much finer grids in 2d.

3.5.4   Convergence Test of the Simulations in 2D

In order to study grid convergence, a 2d model was constructed as a vertical cross-section of the 3d model at y=15 m. The 2d model had therefore the dimensions of 40 m x 20 m in the x and z direction. Fig. 3.8 shows the coarse grid of the 2d model.
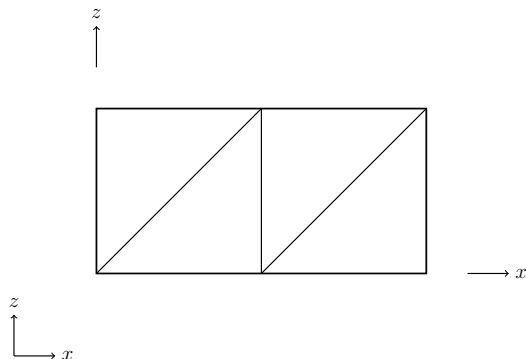
Fig. 3.8   2d coarse grid

The coarse grid has 4 elements and with each additional refinement level, the number of elements increases by a factor of 4. The grid was refined to the levels = 7, 8, 9, 10 and the resulting number of elements as well as the minimum length and the maximum length of the edges are listed in Tab. 3.4. Refinement level 10 of the coarse grid corresponded to a spatial grid resolution of $\Delta x = \Delta z = 0.019\ m$.

Tab. 3.4   Characteristic 2d-grid data for different refinement levels

refinement levels	elements	minimum edge (m)	Maximum edge (m)
7	65536	0.1562	0.221
8	262144	0.07812	0.1105
9	1048576	0.03906	0.05524
10	4194304	0.01953	0.02762

A problem with insufficient refinement could be excluded, but the results showed a similar behavior as in the 3d case. The implemention of thermal point source was therefore examined more closely, and, indeed, an error was detected. After correcting the point source formulation in the code a very good convergence for different refinement levels of coarse grid was achieved. Fig. 3.9 shows 30°C-isolines at time=6 days for refinement levels = 6, 7, 8, 9, 10.
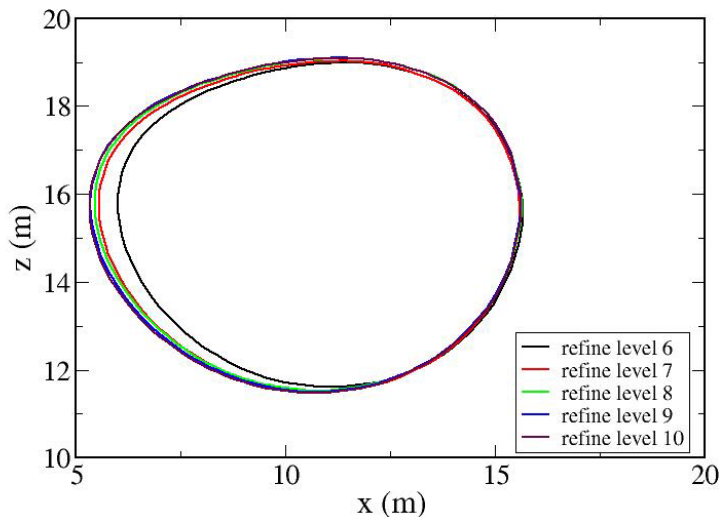
Fig. 3.9   30°C-isolines at time=6 days for refinement levels = 6, 7, 8, 9, 10 with an improved point source formulation

To test the program, a point source was used as the injected warm water source. Actually, a line source should have been used according to the field experiment. After the improvement of the implemented source formulation, a line source was applied between z=15.5 m and z=16.5 m with the source rate $1.03 \cdot 10^{-4}$ m s^{-1}, resulting in a total source rate of $1.03 \cdot 10^{-4}$ m^2 s^{-1} for the line source. The coarse grid was refined to refinement levels= 6, 7, 8, 9, 10 and the 30°C isolines at 6 days showed also a good convergence of the results with the line source (Fig. 3.10).
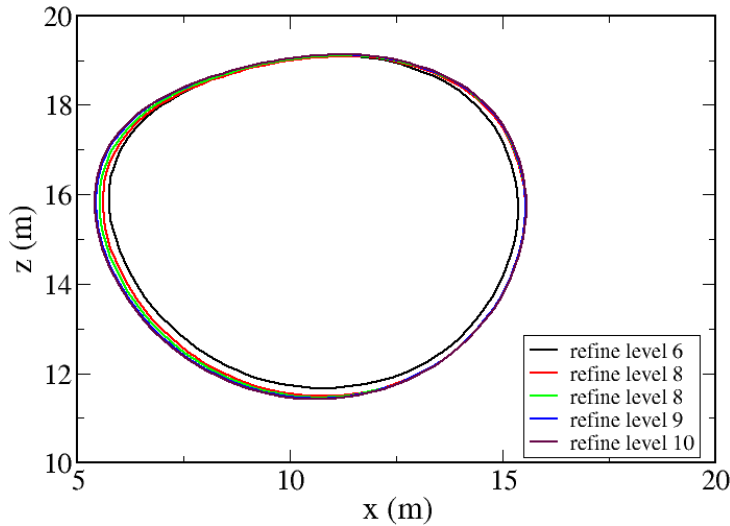
Fig. 3.10   30°C-Isolines at time=6 days for refinement levels = 6, 7, 8, 9, 10 with an improved line source formulation

3.5.5   Improved Point Source in 3d Models

With the corrected formulation of the point source the 3d simulation showed also convergence for different refinement levels. Fig. 3.11 depicts the convergence of 30°C isolines for time=6 days and the refinement levels = 4, 5, 6, 7. The line source was implemented at the point (12 m, 15 m, 16 m) with an injection rate of $1.03 \cdot 10^{-4}$ m^3 s^{-1}. The simulation time step was again 0.2 day. The area covered by the 30°C-isoline became larger and the isolines converged with increasing refinement level.
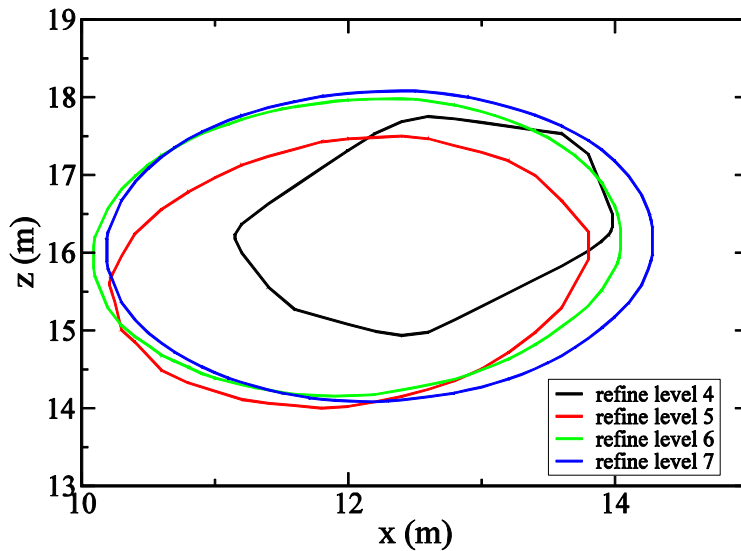
Fig. 3.11   30°C-isolines at time=6 days for refinement levels 4, 5, 6, 7 in 3d with an improved point source formulation

3.5.6   Improved Line Source in 3d Models

With the improved line source formulation the 3d models showed also good convergence for different refinement levels. Fig. 3.12 depicts the convergence of 30°C-isolines after a model time of 6 days on the refinement levels 4, 5, 6, 7. The line source was placed between the point (12 m, 15 m, 15.5 m) and the point (12 m, 15 m, 16.5 m) with an injection rate of $1.03 \cdot 10^{-4}\,m^2\,s^{-1}$, resulting in a total injection rate $1.03 \cdot 10^{-4}\,m^3\,s^{-1}$. The convergence with an increasing level of refinement can be clearly observed.
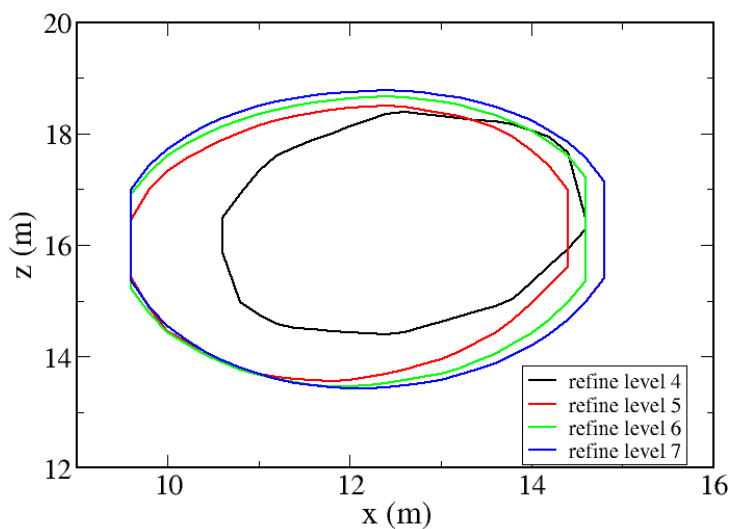
Fig. 3.12   30°C-Isolines at time=6 days for refinement levels = 4, 5, 6, 7 in 3d with an improved line source formulation

Because of the he high computational effort for the simulation with refinement level 7 (25 million nodes) the system was simulated over a model time of 76 days with refinement level 6. The resulting flow field and the thermal distribution are shown in Fig. 3.13. Warm water with a temperature of 37°C was injected in the well between the points (12 m, 15 m, 14.7 m) and (12 m, 15 m, 16.7 m) with a rate of $5.15 \cdot 10^{-5}$ m^2 s^{-1} during the first 6 days, resulting in a total injection rate of $1.03 \cdot 10^{-4}$ m^3 s^{-1} over the length of the injection well. During the injection period, a time step 0.2 day was used, and the flow of the injected water as well as the transported heat were clearly dominating over the background groundwater flow from west to east. After stopping the injection, the time step was increased to 1 day, and the warm water moved slowly eastward with the groundwater flow.
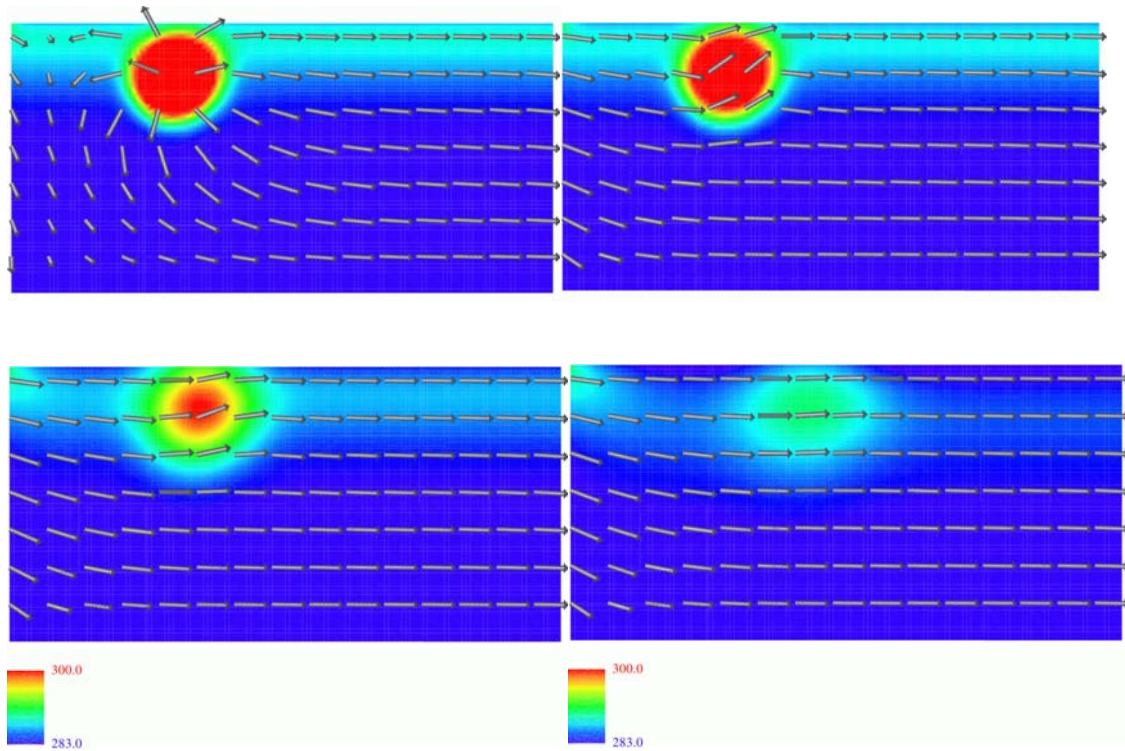
Fig. 3.13   Flow and heat distribution in x-z cross section (y = 15 m) at the time t=6, 9, 27, and 76 days with a line source at refinement level 6 (temperature in K)

In Fig. 3.14 the simulation results are compared with the measurements from the field experiment (/MOL 92a/, /MOL 92/). After a model time of 9 days, the simulated temperature plume has a similar extension than in the measurements, but the isolines have a little higher extension in negative z direction. After 27 days, the isotherms of 22°C, 20°C, 18°C and 16°C from the simulations fit quite well with those from the measurements. The extensions of the isolines of 15°C and 14°C from the simulation

are a little larger than those from the measurement. After 76 days, the simulated plume has a much larger extension than the measured one. Generally, the heat spreads somewhat faster in the simulation than in the field experiment.
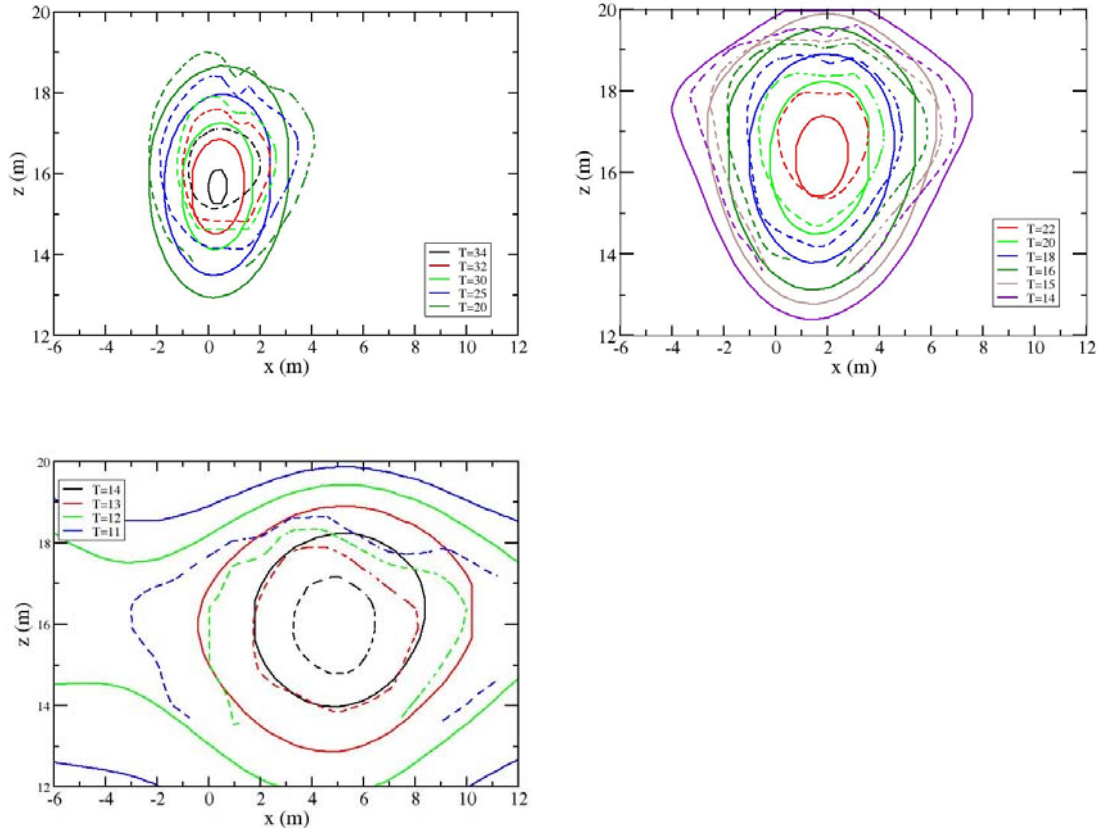
Fig. 3.14   Isolines of different temperatures in a x-z cross section (y=15 m) after 9 days, 27 days and 76 days, comparison of simulations (solid lines) and field experiments (dashed lines)

3.5.7   Influence of the Heat Transfer Factor

In a next step, a Cauchy boundary condition for the temperature in the form

$$\frac{\partial T}{\partial t} = \alpha(T - T_s) \tag{3.7}$$

was applied to the upper boundary, where T_s is the air temperature and α is the heat transfer factor relating to the interaction between the environment and the aquifer. The Cauchy boundary condition was tested varying the factor α. The air temperature values during the period of the field experiment were taken from /MOL 92/, see Fig. 3.3.

Simulations were performed for α = 1.0, α = 0.01, α = 0.001, and α = 0.0001 with a line source for fluid and heat. During the time of injection (the first 6 days), a time step of 0.2 days was used in the simulation, whereas the step time was increased to 1 day after the injection was stopped.

The computed temperature distributions were compared to the measured data and are shown in Fig. 3.15 for α = 1.0, Fig. 3.16 for α = 0.01, Fig. 3.17 for α = 0.001 and Fig. 3.18 for α = 0.0001, respectively. In Fig. 3.16 to Fig. 3.18, the origin of the x-axis is moved to the injection well. Generally, the heat plume is located a little lower in the model domain than indicated by the field experiment. It is also a little narrower.

An impact of the α-values on the temperature distribution at time=9 days is hardly visible. By and large the same applies also to the results for time=27 days.

Differences become more pronounced at later times when the air temperature drops below 0 °C and less heat is drawn from the groundwater with a decreasing α–value. As a consequence the plume appears to be more stretched towards the top boundary.
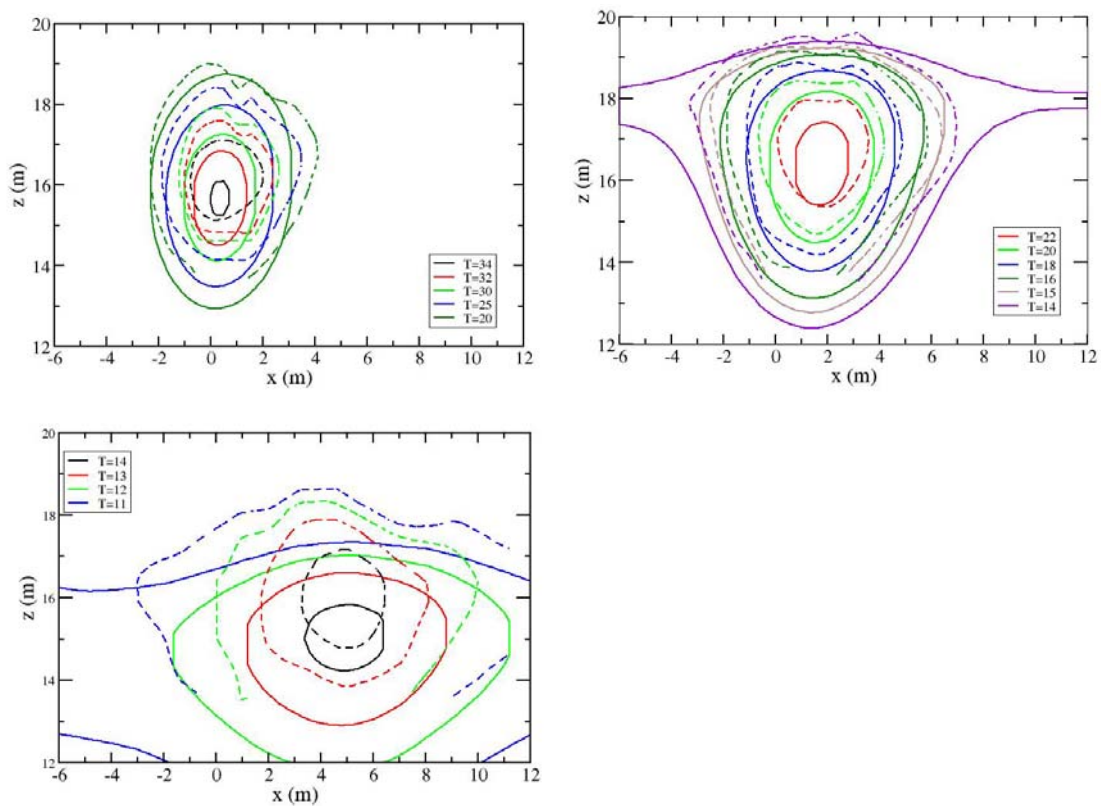
Fig. 3.15   Temperature isolines for times=9, 27 and 76 days; simulation with α = 1.0 (solid lines) and results from the field experiment (dashed lines).
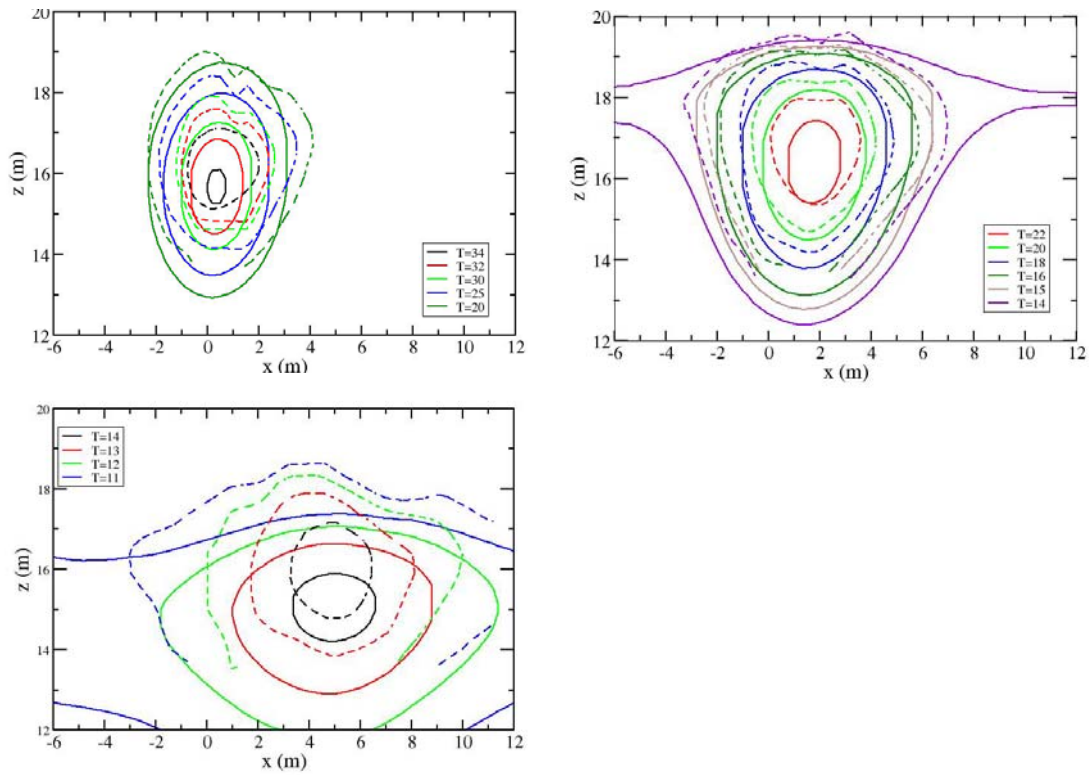
Fig. 3.16 Temperature isolines for times=9, 27 and 76 days; simulation with $\alpha = 0.01$ (solid lines) and results from the field experiment (dashed lines)
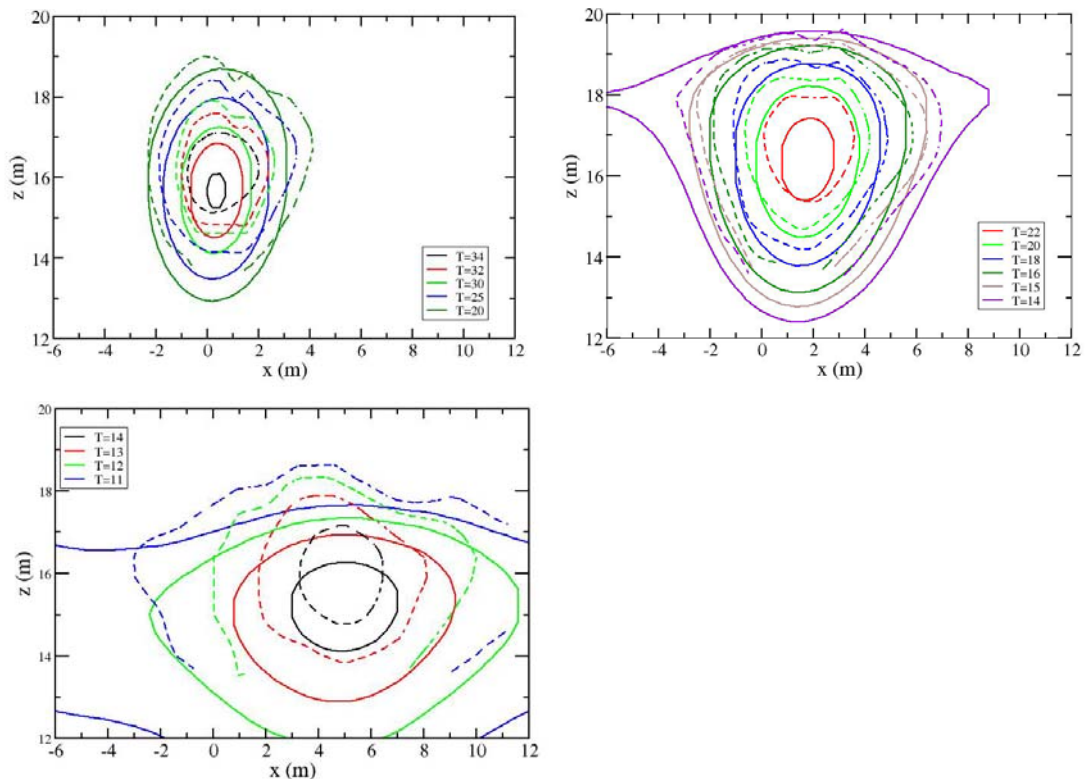
Fig. 3.17 Temperature isolines for times=9, 27 and 76 days; simulation with $\alpha = 0.001$ (solid lines) and results from the field experiment (dashed lines)
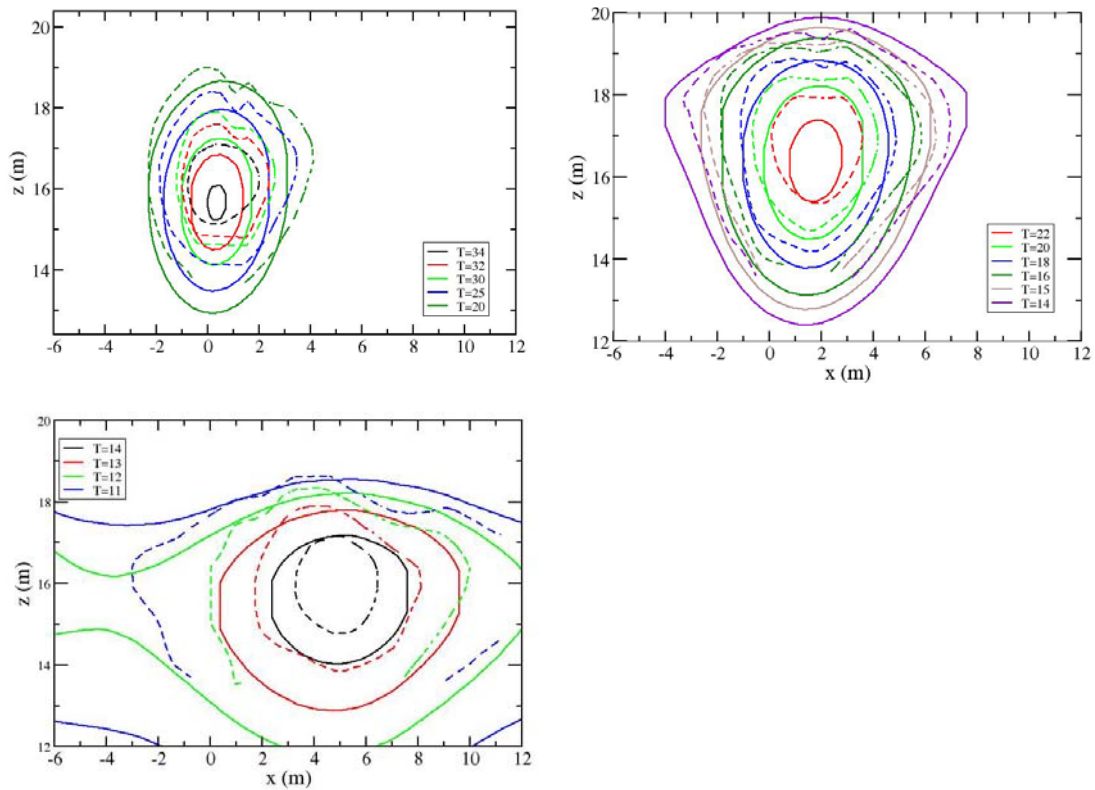
Fig. 3.18 Temperature isolines for times=9, 27 and 76 days; simulation with $\alpha = 0.0001$ (solid lines) and results from the field experiment (dashed lines)

In order to show the effect of different α-values more clearly, the isolines of temperatures T=13°C and T=12°C with different α at a model time of 76 days are compared in Fig. 3.19 with the related isolines from the field experiment. It can be observed that the isolines for α = 1.0 and α = 0.01 are almost identically, whereas the isolines for α = 0.001 are more spread out horizontally as well as towards the top, while the bottom of the isolines seems not to be affected in this variation. Even more pronounced is this in the plot for α = 0.0001. While these computed isolines fit best with the results in the field experiment in the upper area near the top surface, they are too wide at the same time. So the best fit may lie between α = 0.001 and α = 0.0001.
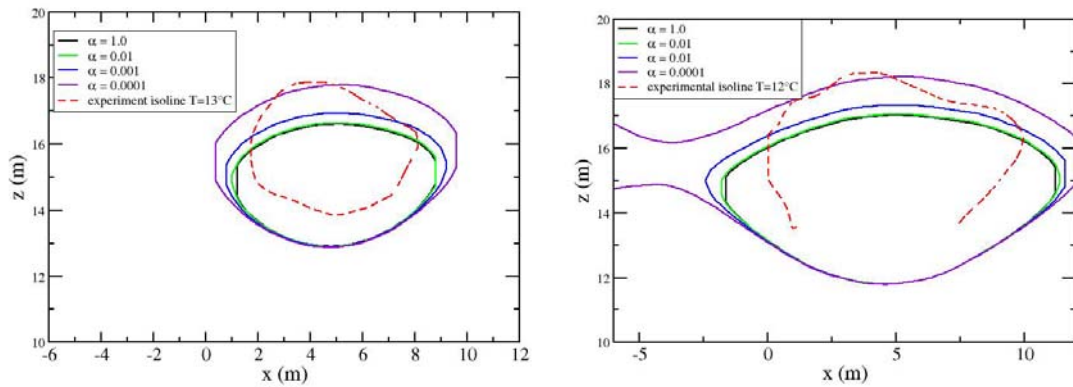
Fig. 3.19 Isolines of temperature T=13°C (left) and T=12°C (right) for time=76 days; simulation with $\alpha = 1.0, \alpha = 0.01$, $\alpha = 0.001$ and $\alpha = 0.0001$ (solid lines) and results from the field experiment (dashed lines)

Vertical temperature profiles along the line x=38 m, y=2 m, z =0 m to 20 m at different days for various α–values are plotted in Fig. 3.20 and can be compared to the experimental results from /MOL 92a/. Different α–values have influence only near the top surface (z > 17 m) as the response to the air temperature is stronger here for larger α–values. At the times 7 days and 14 days, the air temperature is still higher than the temperature at the top surface of the model region, thus the temperature at the top surface is also higher for larger α. At the times 32 days, 42 days and 56 days, the air temperature is lower than the temperature at the top surface of the model region, hence the temperature at the top surface is also lower for larger α. Most of the time either the curves from α = 0.0001 or from α = 0.001 show the best fit to the experimental observation confirming the conclusion from the previous paragraph that the best fit would lie between those values.
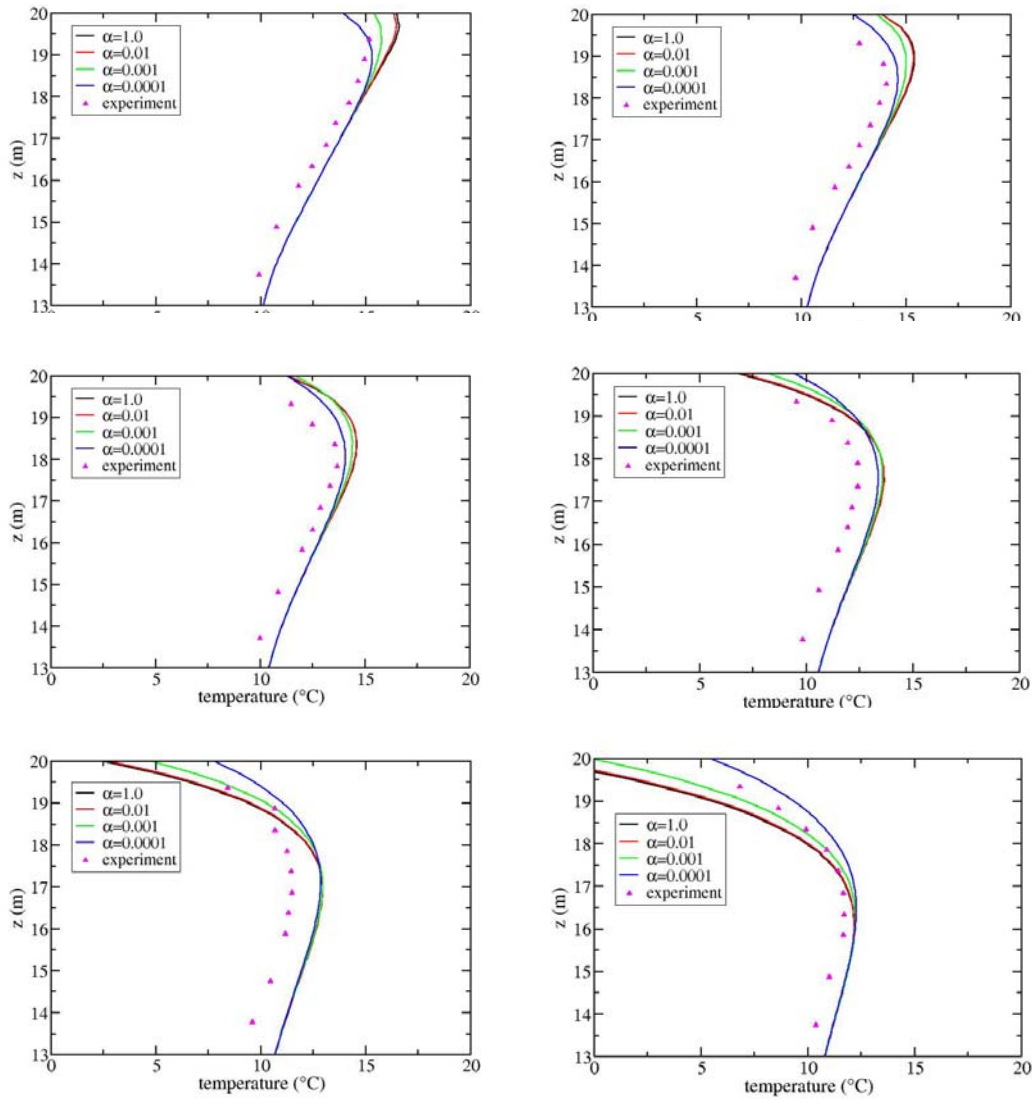
Fig. 3.20 Vertical variations in background aquifer temperature for different α compared to the results of field experiment at 7 days, 14 days, 21 days, 32 days, 42 days and 56 days

The simulation results for $\alpha = 0.0001$ are used to compare with the observations in the field experiment even further. Fig. 3.21 shows the trace of the position of the heat plume peak in the vertical z direction and in the longitudinal x direction. The plume peak moves up at first due to the buoyancy effect of the heated water, and then moves down due to increasing thermal loss at the surface. In the longitudinal direction, the plume moves eastwards from the position of the injection well (x=0) at a constant velocity of approximately 0.066 m/day, which is in very good agreement with the observation. Fig. 3.22 shows the development the peak plume temperature with time. After the

injection, the peak temperature decreases continuously. The simulation results for $\alpha = 0.0001$ fit very good with the measurement from the field experiment.
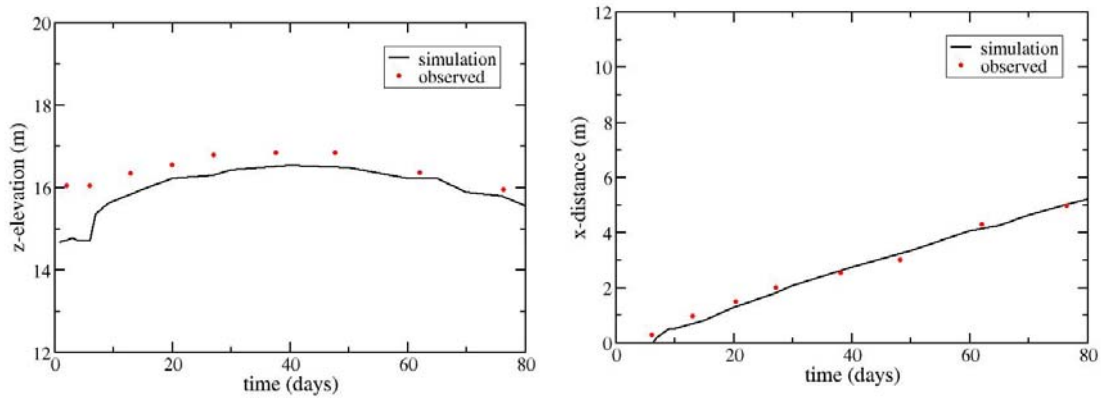
Fig. 3.21 Trace of heat plume peak position in the vertical z direction and the longi-tudinal x direction from simulation ($\alpha = 0.0001$) and results from the field experiment
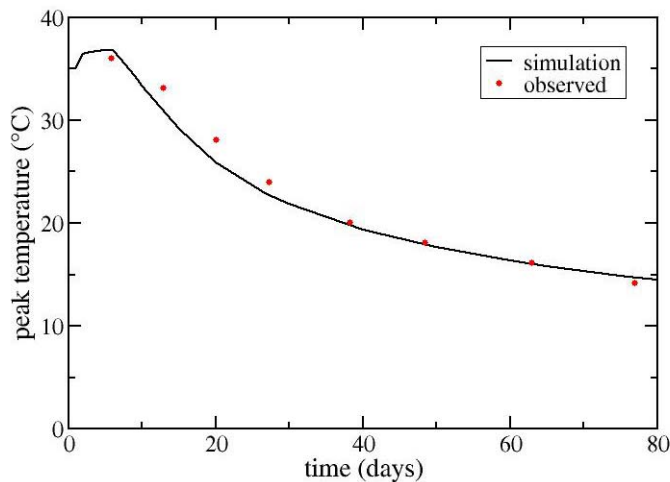
Fig. 3.22 Trace of plume peak temperature, simulation ($\alpha = 0.0001$) compared to the measurements in the field experiment

3.6 Discussion

The groundwater flow with free water surface as well as the heat and the groundwater flow without free water surface using d³f++ are studied in this chapter.

First, the free water surface and the flow velocity were obtained under proper boundary conditions in a three dimensional model.

Then the heat and the groundwater flow were studied in two and three dimensions. The coarse grids were refined to different refinement levels, so that the grid convergence of the simulation could be examined. Little errors were detected and could be fixed.

Furthermore, the influence of the heat transfer factor α, which controls the intensity of the heat transfer between the atmosphere and the aquifer, was studied. The results were compared to the field experiment results. It was found that the factor α has an influence only on the simulated temperature distribution in the upper and middle part of the aquifer. A good fit was found to be in the range of $\alpha = 0.0001$ to $\alpha = 0.001$.

The calculated development of the heat plume peak temperature and its position were compared with the observed results from the field experiment and a good agreement was observed.

It could be shown that d³f++ can deal with the heat and groundwater flow in 2d and 3d models and reproduce the results of the field experiment.

4 Laboratory experiment: Freshwater lens below an island

4.1 Laboratory experiment

The need for drinking water on islands is usually met by drawing water from a freshwater lens situated on saline ocean water. These freshwater resources are perpetually threatened by seawater intrusion due to overexploitation, sea-level rise or storm tides. A proper understanding of the flow regime in freshwater lenses is the basis for a sustainable drinking water management on islands as well as in coastal zones.

For this reason, a series of physical sand tank experiments was performed at the BGR in Hannover to investigate and visualize different groundwater flow regimes of freshwater lenses at laboratory scale /STO 12/, /DOS 13/, /STO 14/, /STO 16/.

One of these experiments was concerned with the influence of recharge rates on the maximum lens thickness steady state in the middle of an island and will be regarded here: A quasi 2d installation representing a cross-section of an infinitely long island was set-up in a sand tank. For this purpose an acrylic glass box of 2.0 m in length, 0.5 m in height and 0.05 m in thickness was filled with compacted, coarse sand with well-defined grain size distribution, forming a homogeneous sand cone as shown in Fig. 4.1. Hydraulic conductivity and total porosity were determined by tests as well as by using empirical formulas, densities by measurements of volume and grain density. Temperature was maintained at 23 °C during the experiment.
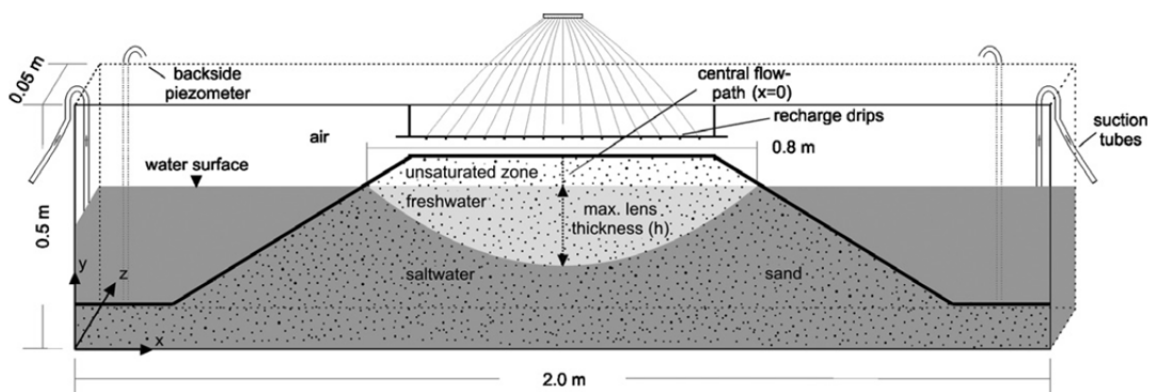
Fig. 4.1   Sand tank experiment physically simulating formation and degradation of a freshwater lense /STO 12/

At the beginning of the experiment, the sand was completely saturated with saltwater with a density of 1021.2 kg m^{-3}. A well-defined freshwater recharge was provided by a

peristaltic pump. For this purpose fifteen individual freshwater drips were installed above the sand cone. To allow freshwater discharge into the "ocean" and to maintain a constant water level, a thin layer was installed on top of the saltwater surface. Here, the freshwater was continuously withdrawed from the left and right model boundaries with a rate equals to the total freshwater recharge. Through the drips freshwater with a density of 997.4 kg m^{-3} was infiltrated displacing saltwater until a stable freshwater lens was formed. For visualization of this process, fluorescent tracers were added to the recharge water. Steady-state was reached after about 3.5 h of infiltration. In a second step, recharge was stopped and the subsequent complete degradation of the lens was observed. The whole experiment was monitored by cameras and measurements (Fig. 4.2).
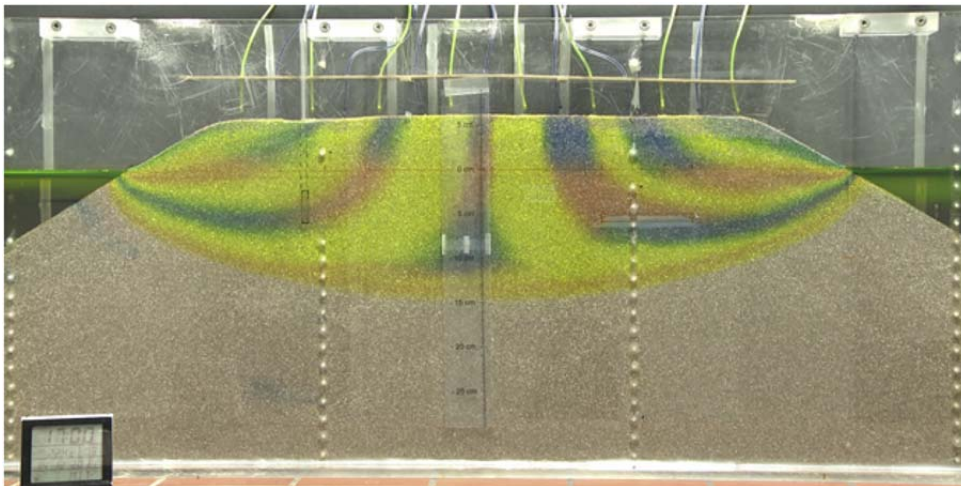
Fig. 4.2   Visualization of lens thickness and flow path by colored tracers /STO 12/

Finally, the experimental results were compared to the analytical models by /FET 72/ and /VAC 90/ as well as to a numerical FEFLOW model which matched very well. For detailed description of the experiment see /STO 12/.

4.2   Benchmark definition

Based on the experiment, a 2d numerical benchmark for variable-density flow in a freshwater lens was defined describing the formation and degradation of a freshwater lens over time /STO 16/. A calibrated parameter set was obtained using the parameter estimation tool PEST, and a sensitivity analysis was performed. The well-defined benchmark was used for a comparison of five numerical codes capable of solving the equations for variable-density flow, i.e. the first two equations of (1.1). These codes

were FEFLOW /DIE 14/, SPRING /KOE 16/, OpenGeoSys /KOL 11/, HydroGeoSphere /BRU 12/ and d³f++ /VOG 13/.

The fluid viscosity μ was assumed to be constant. The density ρ was assumed to depend linearly on the relative, normed brine mass fraction ω as described in equation (4.1).

$$\rho = \rho_0 \left(1 + \frac{\rho - \rho_0}{\rho_0} \omega \right) \qquad (4.1)$$

The models were all set up using the same conceptual model as described in Fig. 4.3: Because of symmetry the model domain covers only the right half of the experiment. The left boundary represents the line of symmetry and is, like the bottom boundary, closed for flow and transport (Neumann boundary condition, bc). To the horizontal top boundary another Neumann bc, an inflow velocity of $1.333 \cdot 10^{-5}\,m\,s^{-1}$, was assigned except for 0.01 m at the right corner that were regarded to be closed. The brine mass fraction ω was set to 0 at the horizontal top boundary. At the inclined top a Dirichlet bc was defined for the pressure

$$p = \rho_S\, g\, (z - h), \text{ where } h = 0.3\,m \text{ and } g = -9.81\,m\,s^{-2}. \qquad (4.2)$$

In case of inflow at the inclined top a brine mass fraction of $\omega = 1$ was assumed at this boundary, while ω adopted the current local value inside the domain in case of outflow ("in-out-bc").

recharge $1.333 \cdot 10^{-5}$ m s^{-1}
ω = 0

0.4 m

hydrostatic pressure
$\omega_S = 35$ kg m$^{-3} \equiv \omega = 1$

0.3 m

0.9 m
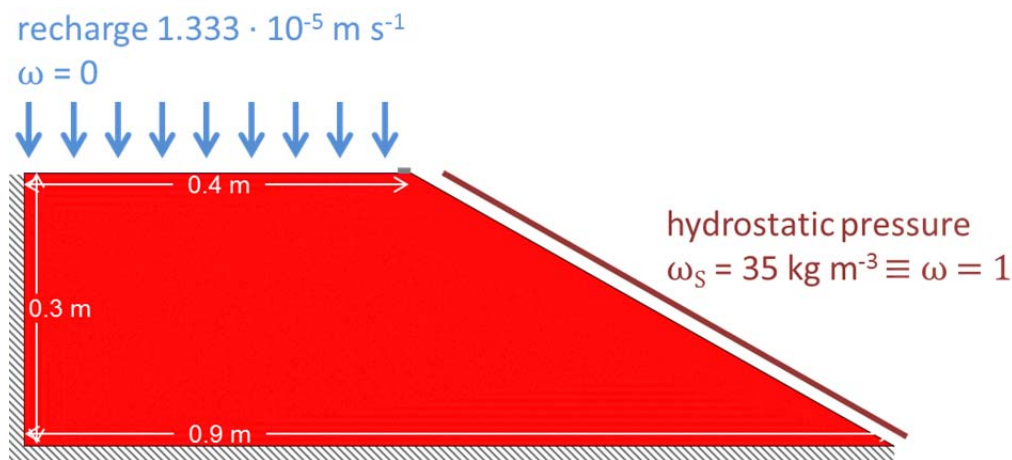
Fig. 4.3   Conceptual model and boundary conditions

As initial conditions the brine mass fraction ω was set to 1 and a hydrostatic pressure was assumed. The physical parameters used are compiled in Tab. 4.1.

Tab. 4.1   Benchmark freshwater lens: Parameters of the numerical model

parameter	value
effective porosity Φ	0.39
permeability k	$4.6 \cdot 10^{-10}\,\text{m}^2$
molecular diffusion D_m	$1.0 \cdot 10^{-9}\,\text{m}^2\,\text{s}^{-1}$
longitudinal dispersivity α_L	$5.0 \cdot 10^{-3}\,\text{m}$
transverse dispersivity α_T	$5.0 \cdot 10^{-4}\,\text{m}$
freshwater density ρ_0	$997\,\text{kg m}^{-3}$
seawater concentration ω_S	$35\,\text{kg m}^3$
seawater density ρ_S	$1021\,\text{kg m}^{-3}$
viscosity μ	$1.0 \cdot 10^{-3}\,\text{Pa s}$
recharge rate q_r	$1.333 \cdot 10^{-5}\,\text{m s}^{-1}$

The whole domain was supposed to be fluid-saturated over the whole model time, so that a moving groundwater surface had not to be regarded. All codes had to apply the Boussinesq approximation instead of solving the complete density dependent equation system, i.e. the transport equation, reducing the second equation in (1.1) to

$$\partial_t(\phi\omega) + \nabla \cdot (\omega\boldsymbol{q} - \boldsymbol{D}\nabla\omega) = 0. \qquad (4.3)$$

Furthermore, all codes were bound to abandon upwind-algorithms and to use only standard discretizations, and they were obliged to work on the same numerical grid consisting of 241,400 triangular elements and 121,362 nodes resulting of a grid convergence study. The time step size was set to 8.64 s.

4.3 Numerical model

In the first phase, the formation of the freshwater lens was simulated. The development of salt concentration and velocity vectors over time resulting from the d³f++ simulations are shown in Fig. 4.4.

The upper two pictures show the situation in the beginning, when the freshwater lens is building up. Freshwater is displacing saltwater, and a small transition zone of brackish water evolves between the lens and the displaced seawater. The general flow direction in the freshwater as well as in the seawater is downward and towards the "sea" boundary.

Between 2 and 2.5 h, though, the lens begins to stabilize. Starting at the seawater boundary, flow vectors change their directions. Freshwater as well as brackish water leave the domain at the very top of the simulated sea boundary while seawater is entering the domain further down due to the higher density and the related higher hydrostatic pressure. The thickness of the freshwater/saltwater interface decreases. The steady-state conditions are eventually characterized by a dynamic equilibrium between freshwater recharge and saltwater intrusion. Both feed the narrow zone of brackish water which represents the main path for water discharge from the model.

The second phase of this numerical benchmark started with the steady-state result of the first phase and continued with the degradation of the freshwater lens up to a situation where the freshwater was completely displaced by saltwater again.

To compare the behavior of the five codes, firstly, steady-state results of salinity distributions and flow directions for the different modeling tools were analyzed. Secondly, transient propagation of concentration contours and saltwater-freshwater interface properties during lens formation and degradation were compared to physical experimental results in /STO 12/.
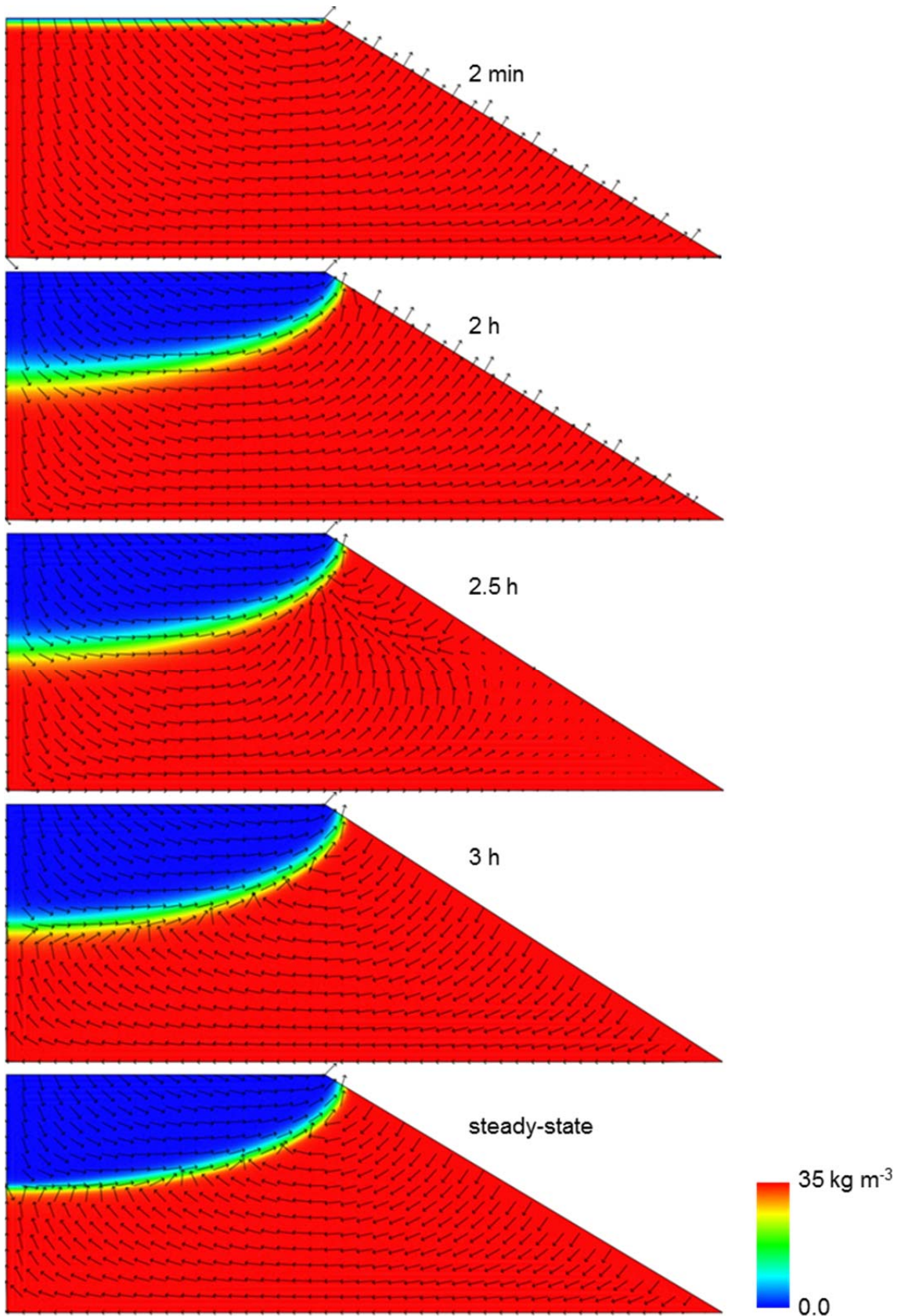
Fig. 4.4 Development of salt concentration and velocity vectors over time as results of d³f++ simulations

A comparison of the steady-state results for the salt concentration is shown in Fig. 4.5. The results show a high degree of similarity and agreement with the experimental results, but also some differences. The code SPRING shows differences at the freshwater discharge boundary because the in-out boundary condition mentioned above is not available in this code, i.e. seawater concentration had to be fixed at the whole boundary. Another noticeable difference is the thickness of the transition zone at its maximum depth that is much larger in the result of OpenGeoSys. In case of HydroGeoSphere the transition zone is thicker close to the outflow zone. SPRING shows only small differences, were the results of d³f++ and FEFLOW are almost identical.
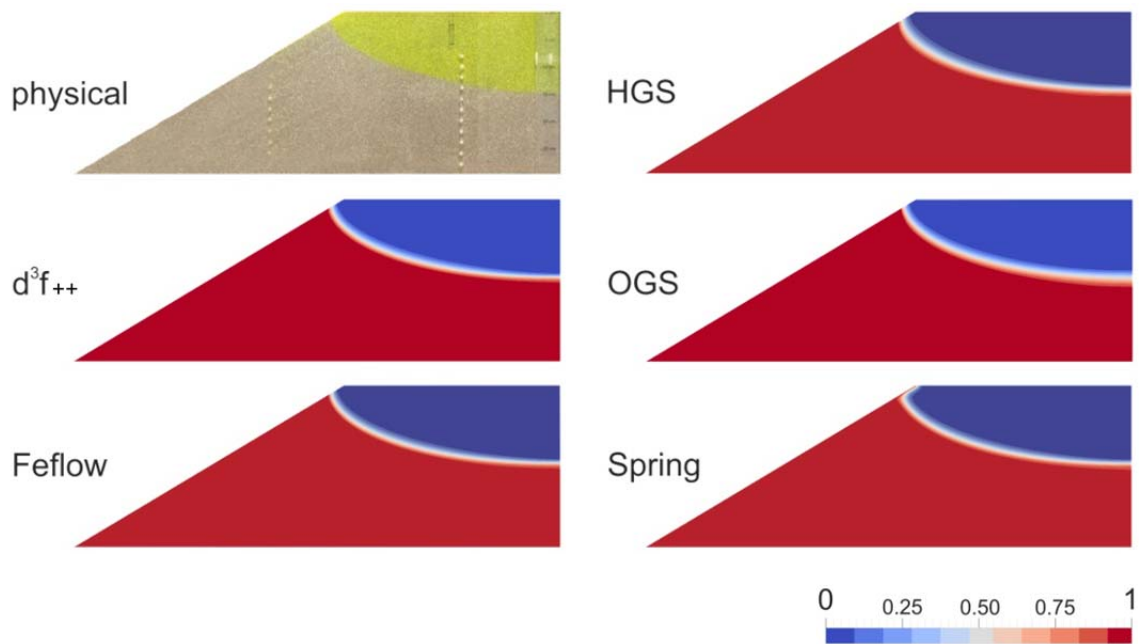
Fig. 4.5   Comparison of the salinity distributions at steady-state of the physical model (top left) and the numerical simulations /STO 16/

To make the differences clearly visible, the transient development of the interface width (0.1 < c < 0.9) at the vertical boundary is plotted in Fig. 4.6.

Additionally, the transient development of the maximum depth of the freshwater lens was analyzed. Therefore, the 0.5 – isochore at the symmetry line was compared for each code. Concerning this criterion all codes showed a complete agreement. For detailed results see /STO 16/.
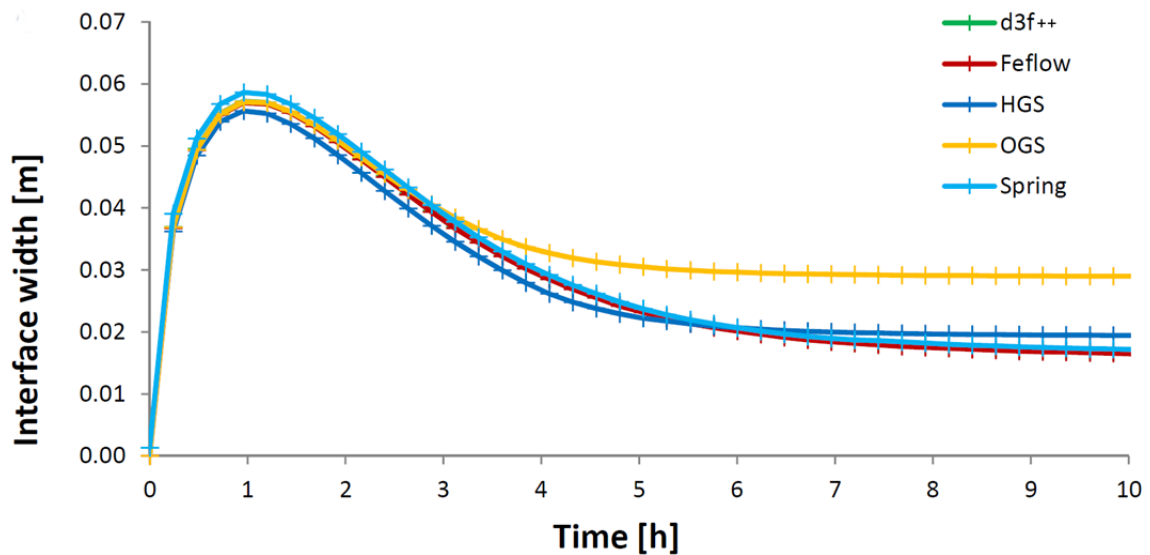
Fig. 4.6   Transient development of the interface width (0.1 < c < 0.9) at the vertical
boundary /STO 16/

The discrepancies in the thickness of the transition zone are assumed to arise from dif-
ferences in the specifications of the finite volume or finite element discretizations of the
partial differential equation system or in the numerical solvers, respectively. Multigrid
solvers should not be used to avoid such differences, therefore d³f++ and FEFLOW
used BiCGStab solvers.

In a second comparison, the steady-state flow fields were analyzed. For this purpose
the angles of flow direction with respect to a horizontal vector from right to left (0°) were
plotted as shown in Fig. 4.7. All models show a similar structure in their flow directions
except at the zone where the interface touches the symmetry line. On the right hand
side of Fig. 4.7, an enlarged view of this area is shown. The d³f++ model shows clear
transitions and no fluctuations of flow directions. In the results with SPRING, and more
apparent in FEFLOW-results, small irregularities are visible at the boundary. The larger
orange/red colored areas within the yellow zone obtained by HydroGeoSphere indicate
upward flow. In the OpenGeoSys-results, vectors jump between opposite flow direc-
tions from one cell to the next in this area of low flow velocities, visualized by alternat-
ing yellow, red, purple and blue colors.
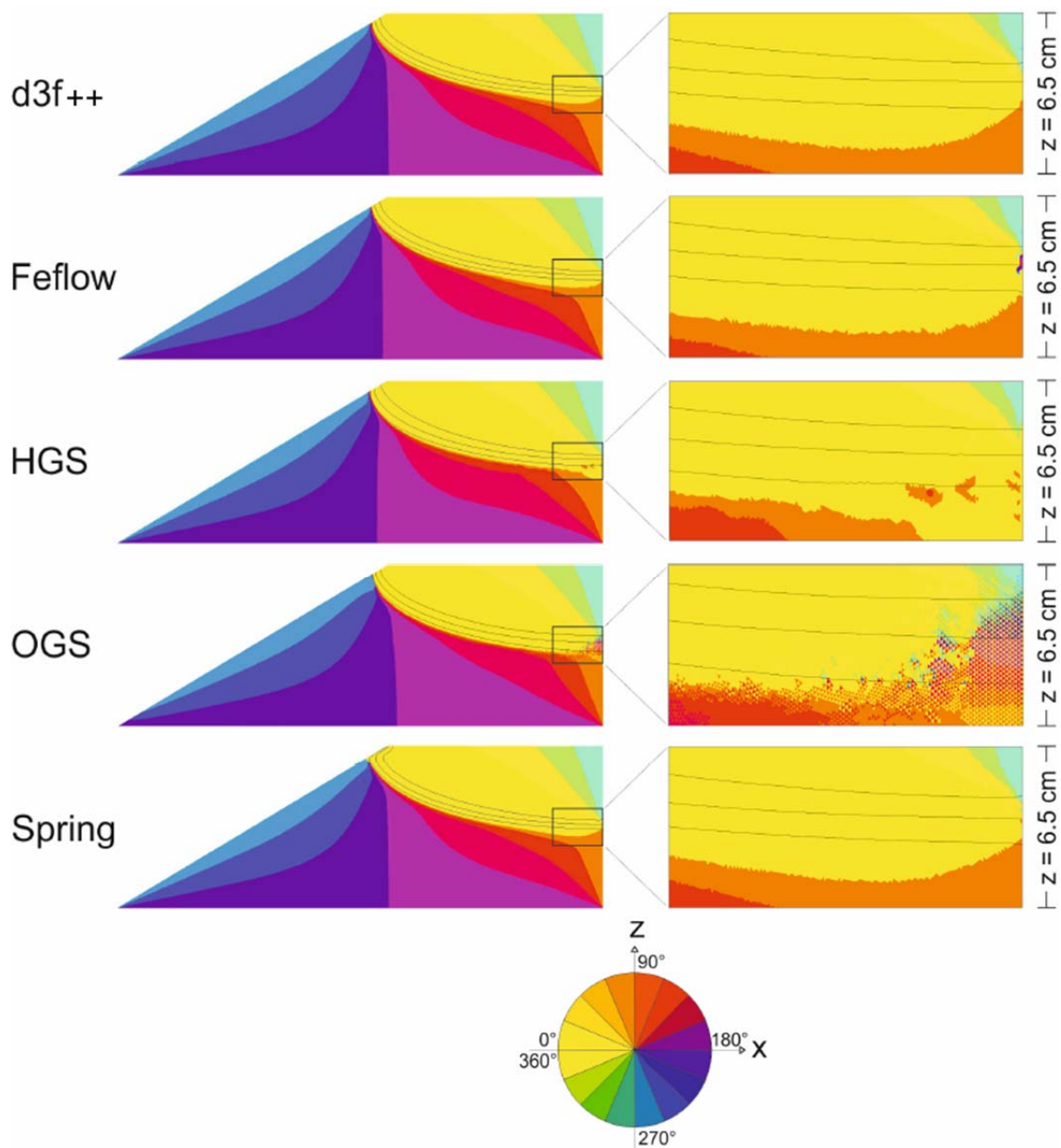
Fig. 4.7   Angles of flow direction at steady-state with respect to the horizontal vector from right to left (0°). The black lines represent the 0.1, 0.5, 0.9 concentration contours from top to bottom. On the right hand side, an enlarged view of the transition zone at the vertical boundary is shown. /STO 16/

4.4   Summary

Benchmarks based on laboratory experiments are very important for the testing of numerical codes. This benchmark firstly published in /STO 12/ may serve as a lab-scale principal model for the formation and degradation of a freshwater lens. Of course it is restricted to the homogeneous case, neglects the effects of a free groundwater surface

and one of the gravest difficulties of hydrogeological models – the extremely flat structures and anisotropies – are skipped here.

Nevertheless, this benchmark provides the possibility of comparing the results of various density-driven flow codes with regard to the relevant physical processes in the field of freshwater lenses.

All five numerical codes were able to adequately reproduce the results from the experiment. The numerical results showed a high degree of similarity and agreement with the experimental results, but despite all efforts to make the models as similar as possible also some differences resulting from different numerical solvers and a different set of available boundary conditions.

The code d³f++ was disadvantaged with a view to numerical efficiency because it was not allowed to use multigrid solvers. However, it was able to simulate formation and degradation of a freshwater lens physically correct including reasonable boundary condition, and thus provided the best results in the comparison with four other established codes.

5 Density-driven flow with free groundwater surface – the WIPP-Site model

The Waste Isolation Pilot Plant (WIPP) is a repository for transuranic waste situated in a semi-arid region of southeastern New Mexico and western Texas, 42 km east of the City of Carlsbad, USA.

The repository itself is located in a large, thick, Permian-age deposit of bedded salt, the Salado formation. This host rock formation is covered by flat bedded Permian halite, dolomite, anhydrite and clastic hydrogeological units as well as Triassic and Quaternary sandstone. Various modeling studies to examine groundwater flow in the rocks overlying the WIPP repository were performed in the past by Sandia National Laboratories (SNL), from 2d modeling up to a 3d basin-scale model covering an area of about 6,000 km² /DAV 89/, /COR 96/, /COR 00/. The basin model region is bounded by watersheds. It has a length of 112 km in north-south direction and a maximum width of 78 km. see Fig. 3.1.
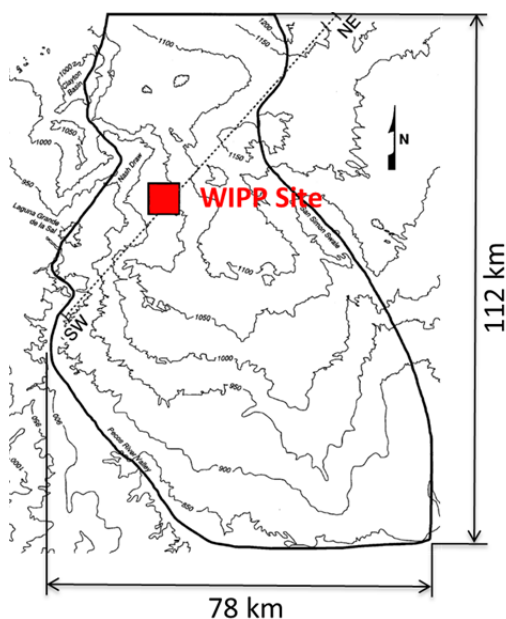
Fig. 5.1   WIPP-Site, boundary of the basin model after /COR 00/

Were previous models of GRS that were considering density effects, restricted to 2d or small scale domains (see e. g. /KRO 96/), the present model is threedimensional and includes the overburden in the entire basin. It has a maximum depth of almost 700 m.

5.1 Hydrogeological situation

The studied region is characterized by a smooth topographic relief, the elevation of the land surface ranges from about 850 m a.s.l. at the river Pecos to 1200 m in the north-eastern part. A schematic hydrogeogical cross section of host rock and overburden is shown in Fig. 5.2.
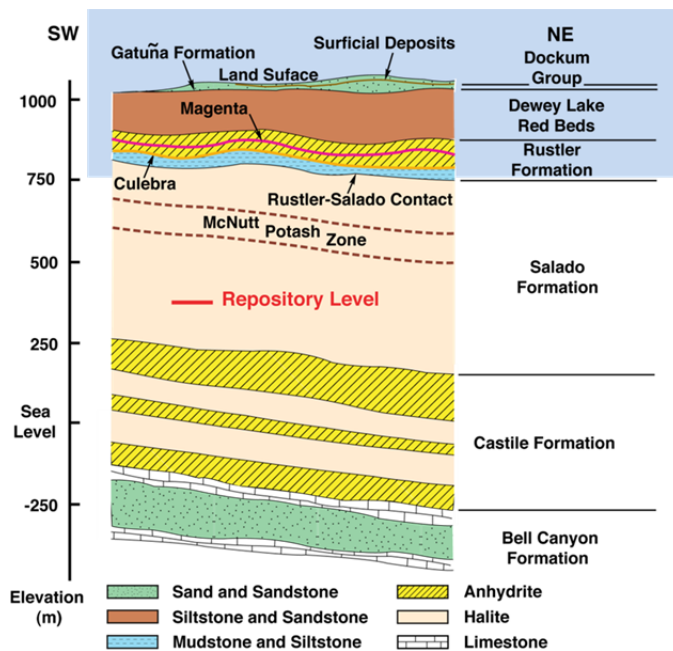
Fig. 5.2   WIPP-Site, schematic cross section (US DOE)

The lowest layer above the Salado, the Permian Rustler formation consists of anhydrite interbedded with dolomitic limestone, interlaminated dolomite and anhydrite, muddy halite, and clastics ranging from mudstone to fine-grained sandstone. It has a thickness of 100-150 m and is divided into five layers or members, /DAV 89/, see Fig. 5.3.

The lowest of these members, Los Medanos Member, consists of basal, fine-grained sandstone and mudstone overlain by interbeds of anhydrite, halite, and mudstone and has a thickness of 27 – 37 m. The basal, fine-grained sandstone forms the upper part of the Rustler-Salado contact zone. The anhydrite, halite and mudstone in the upper part of the lower unnamed member are relatively impermeable and act as confining beds for the brine in the Rustler-Salado contact zone that is under artesian conditions.

The following Culebra Dolomite Member is a fine-textured, microcrystalline dolomite or dolomitic limestone. The Culebra has a thickness of approximately 8 meters over a

very large area, but there exist zones with a thickness of only 2 m or less. In some parts the Culebra Dolomite is extensively fractured, and the intensity of fracturing increases from east to west. First hydrologic field studies focused on the Culebra Dolomite. Because of its relatively high permeability in the vicinity of the WIPP site, the Culebra is considered to be an important potential pathway for the transport of radionuclides.

The Culebra Dolomite Member is overlain by the Tamarisk Member. East of the WIPP site the Tamarisk Member consists of about 55 meters of anhydrite and muddy halite. In the vicinity of the WIPP-Site and to the west in Nash Draw, the 20 to 30 meters of Tamarisk halite have been completely removed, leaving behind a 2- to 5-meter-thick mudstone residue. In the vicinity of the WIPP site the Tamarisk is almost impermeable. Westward toward Nash Draw, an increased permeability was observed, possibly due to fracturing. Here the Tamarisk is assumed to consist of two anhydrite layers, separated by a thin bedding of mudstone and halite, respectively, see Fig. 5.3.

The overlying Magenta Dolomite Member consists of dolomite and anhydrite with a thickness of about 7 m. It is partially fractured and has also relatively high permeabilities increasing from east to west, even though somewhat lower than in the Culebra. The Magenta is dry at several locations in central and northern Nash Draw, and it has been completely removed by erosion in southern Nash Draw.

The Forty-niner Member is the youngest unit in the Rustler Formation. It consists of approximately 25 meters of low permeable anhydrite and muddy halite. In the vicinity of the WIPP site and to the west, the halite has been completely dissolved, leaving behind a 2- to 3-meter-thick residue of mudstone. In this basin model the Forty-niner member is assumed to consist of two anhydrite layers, separated by a thin bedding of mudstone and halite, respectively, see Fig. 5.3.

The Rustler Formation is overlain by the Permian Dewey Lake Red Beds, consisting of alternating beds of siltstone and fine-grained sandstone. In the eastern part of the basin it is 150 to 180 meters thick; whereas towards the west, it has increasingly been subject to erosion and is completely removed by erosion in the western part of the basin /DAV 89/. Here, the overlying, undifferentiated Triassic Rocks including the Dockum Group (Fig. 5.2) are combined with the Dewey Lake Red Beds to one layer of the hydrogeological model, see Fig. 5.3.
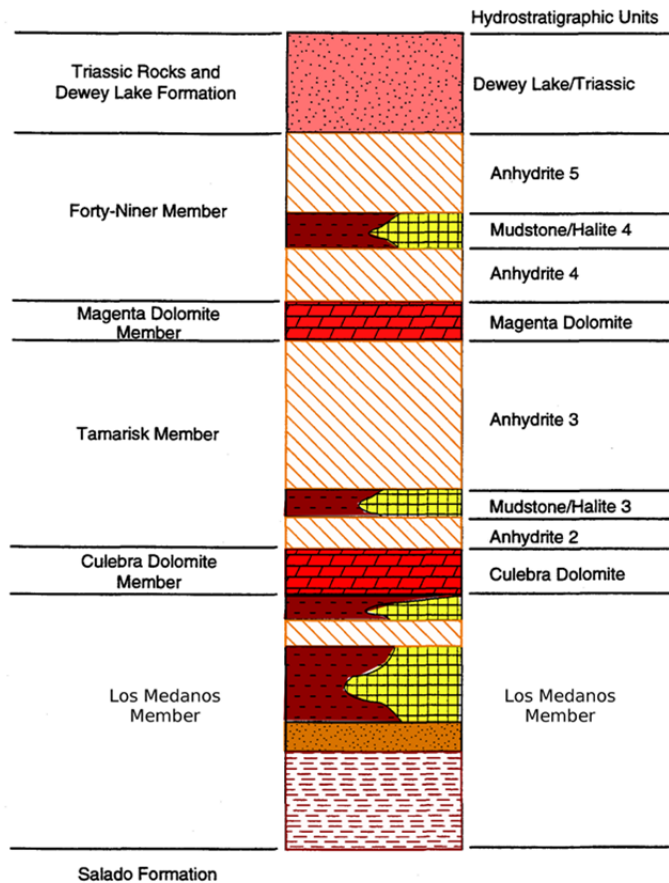
Fig. 5.3 Hydrostratigraphic units of the WIPP-Site basin-scale model /COR 96/

Based on geological data as well as on data from plant and animal remains, alternating climatical conditions are assumed throughout the Pleistocene Epoch with mean precipitation rates about twice that of the present /COR 00/. Up to 10,000 years in the past, precipitation is assumed to vary between 500 and 600 mm/year, decreasing rapidly to about 280 – 340 mm/year as the present values, whereas three peaks of 420 mm/a are supposed to have occurred 6,000, 4,000 and 1,500 years ago.

Because of the dry climates, groundwater recharge constitutes only a small percentage of precipitation, sinking from 2 mm/year 14,000 years ago to only 0 to 0.2 mm/year during the last 8,000 years /COR 00/. It is assumed that the groundwater table was near the land surface 14,000 years ago, while it is at a depth up to 150 m below especially in the north-eastern part of the model area /COR 00/.

5.2   Model description

The objective of the current modeling is to enhance the understanding of the ground-water flow dynamics in the basin in a time frame of tens of thousands of years and forecasting the impact of density effects. This includes varying recharge rates while checking the position of the water table and the groundwater flow patterns. Finally, a comparison of the d³f++ results with PFLOTRAN-simulations /LIC 14/ is planned.

The first small 3d density-driven flow model of the WIPP-Site region was presented by Davies using SUTRA /VOS 84/, /DAV 89/. In 1996, Corbet and Knupp presented a basin-scale groundwater model without regarding density effects, using the SNL-code SECOFL3D /COR 96/, /COR 00/.

The d³f++ model presented here is directly based on the SECOFL3D input data provided by SNL. The geometrical data were received as raster data describing the 10 basal surfaces of the hydrogeological layers as well as the land surface. These 11 raster surfaces were converted into a 3d d³f++ numerical grid using the ProMesh preprocessing tool (www.promesh3d.com), see Fig. 5.4.
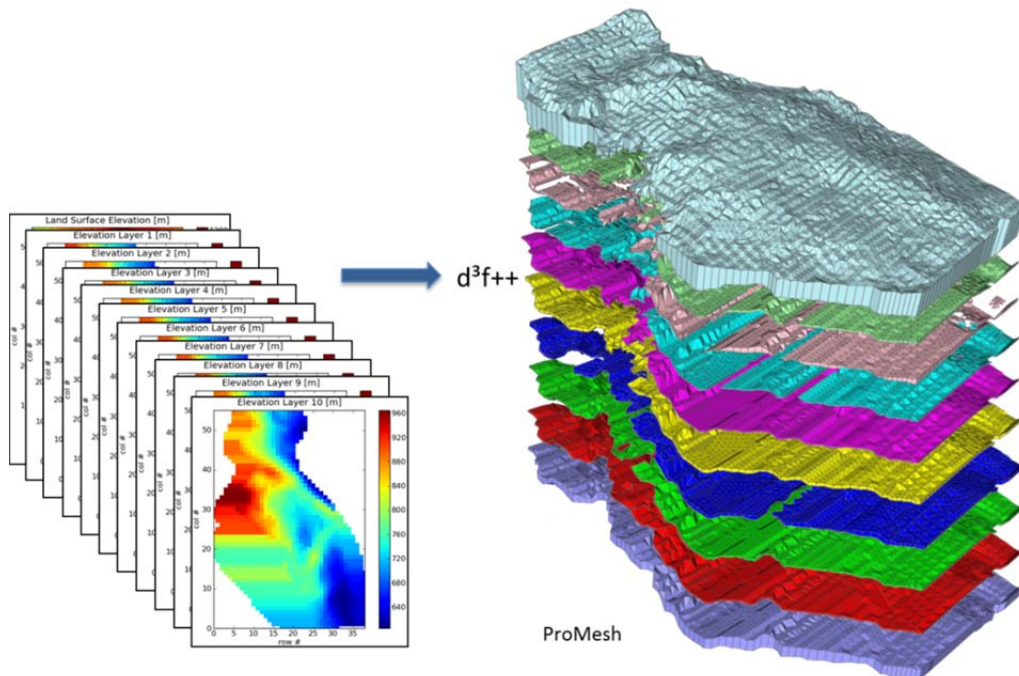
Fig. 5.4   Construction of the 3d d³f++ model from 11 raster surfaces

The model domain has a depth of about 700 m and consists of 10 flat bedded layers with contrasts in their permeabilities of up to seven orders of magnitude, where the two

main aquifers, the Culebra Dolomite and the Magenta Dolomite, have a thickness of only 2 m over huge areas. These characteristics combined with the large horizontal extension of the model domain evoke high numerical anisotropies.

For this reason, the first d³f++ model restricts to only six layers as described on the left hand side of Fig. 5.3. The resulting geometry model is shown in Fig. 5.5.
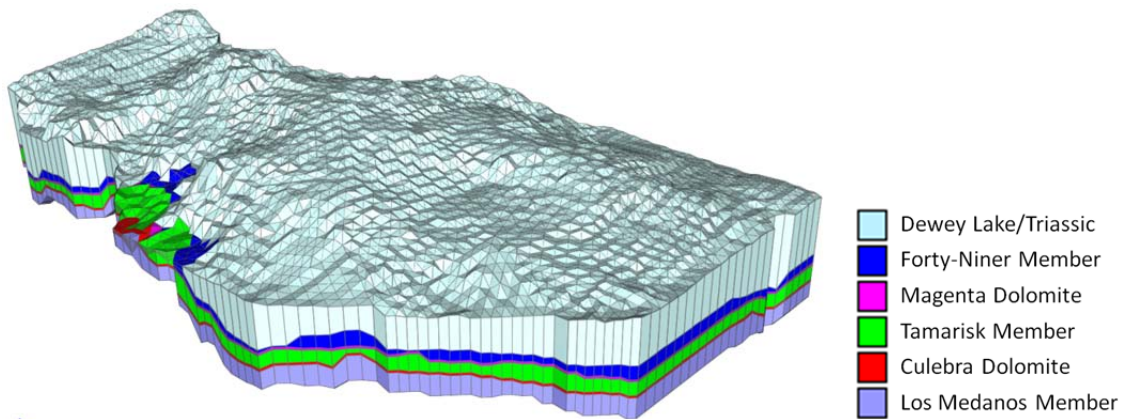
Fig. 5.5   WIPP-Site: 6 layers model, 50x exaggerated in vertical direction

The permeabilities and porosities used for each hydrogeological unit are compiled in Tab. 5.1. It has to be kept in mind that the permeabilities are not constant over the whole basin area within one layer. They are varying from lower values in the east, where the halite and limestone structures are still undisturbed, compared to the western, lower bedded areas, where formations and members are dissolved or strongly fractured, respectively.

Tab. 5.1   WIPP-site model: permeabilities and porosities

unit	permeability [m²]	porosity
Dewey Lake/Triassic	10^{-14}-10^{-12}	0.15
Forty-Niner Member	10^{-17}-10^{-16}	0.14
Magenta Dolomite	10^{-17}-10^{-12}	0.14
Tamarisk Member	10^{-21}-10^{-18}	0.14
Culebra Dolomite	10^{-17}-10^{-11}	0.15
Los Medanos Member	10^{-21}-10^{-18}	0.1

The diffusion coefficient D_m was set to 10^{-9} m² s^{-1} and the dispersion lengths are set to $\alpha_L = 10$ m and $\alpha_T = 1$ m (see equation (1.1)).

Fig. 5.6 illustrates exemplarily the distribution of conductivities in the Culebra Dolomite and the formation above the Rustler. (To get the permeabilities, these values have to be multiplied by a factor of about 10^{-7}.)
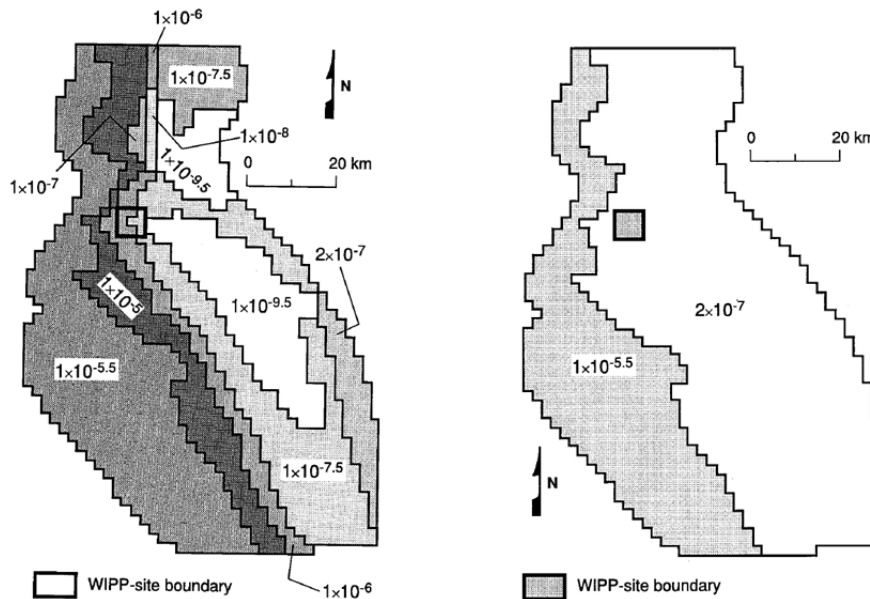
Fig. 5.6   WIPP-Site model: Distribution of hydraulic conductivities on example of the Culebra Dolomite (left) and the Dewey Lake/Triassic (right) after /COR 00/

5.3   Numerical model

Corbet and Knupp /COR 00/ used a computational grid consisting of only 18,000 hexahedrons. They started simulating groundwater flow about 14,000 years model time in the past in order to match the present groundwater flow regime, verifying their model among other by pressure measurements and the current groundwater table. The first objective of the d³f++ modelling is the reproduction of their results, but using a density-driven flow model. In the next steps, the model will be improved and resolved by finer computational grids. After that, simulations of the future groundwater regime will be performed. Concurrently, SNL does the same modelling using their own code PFLOTRAN /LIC 14/. Finally, these works will lead into a benchmark exercise between d³f++ and PFLOTRAN.

The WIPP-Site model provoked some improvements of ProMesh. At the beginning, the 3d grid generator was restricted to tetrahedron meshes. Because of the extremely thin layers with their large horizontal extension, the first coarse grid consisted of 2.6 million of tetrahedron elements, which is not viable for a multigrid algorithm. Therefore a prism grid generator was developed and implemented resolving the thin layers by only one element in vertical direction. The result was a coarse grid consisting of 54,200 prism elements enabling simulations up to multigrid level two.

In this case the coarse grid only has nodes on the layer boundaries while the fine grids also have inner nodes. That means jumps in permeabilities are resolved on the finer grids, but not on the coarse grid. This discrepancy led to inconsistencies within the multigrid method. Therefore another algorithm was implemented allowing a better vertical resolution. To avoid getting high numbers of nodes again, a new refinement method was developed: By construction of special projectors within the multigrid algorithm, it is possible now to include the complete geometrical information of the original raster data in the grid refinement process, that means using a coarse grid consisting of relatively few elements causes no loss of geometrical information on the finer grids while the grid quality remains good on all grid levels.
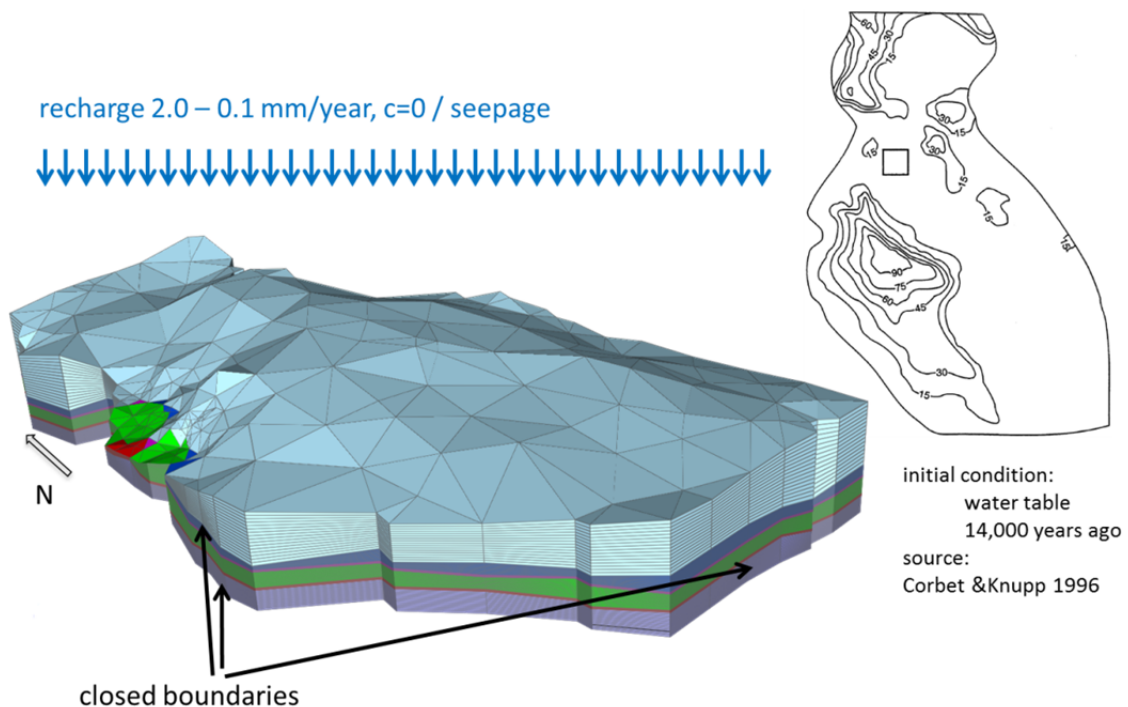
Fig. 5.7   WIPP-Site model with coarse grid and boundary conditions, 50 times exaggerated in vertical direction

right: initial condition for the free groundwater surface after /COR 00/

The coarse grid consisting of 35,136 prism elements is shown in Fig. 5.7. The bottom of the model and the lateral boundaries are assumed to be closed for groundwater flow. On the bottom boundary the concentration of saturated brine is prescribed as a Dirichlet boundary condition, where a Neumann-zero-condition is set for the salt concentration on the lateral boundaries. On the upper boundary a groundwater recharge varying from about 2 mm 14,000 years ago to 0.1 mm in the present is defined, and freshwater concentration is assumed. In the north-western region, the Nash Draw, a leaching boundary develops. As an initial condition the salt concentration was set to zero in the whole model.

5.4 Results

First simulations were performed using a level one multigrid solver with 280,000 elements on the fine grid, assuming a fixed water table. In this configuration a simulation on 12 processors over a model time of 14,000 years needed about 20 min computing time allowing time steps of 100 years. For results see Fig. 5.8.
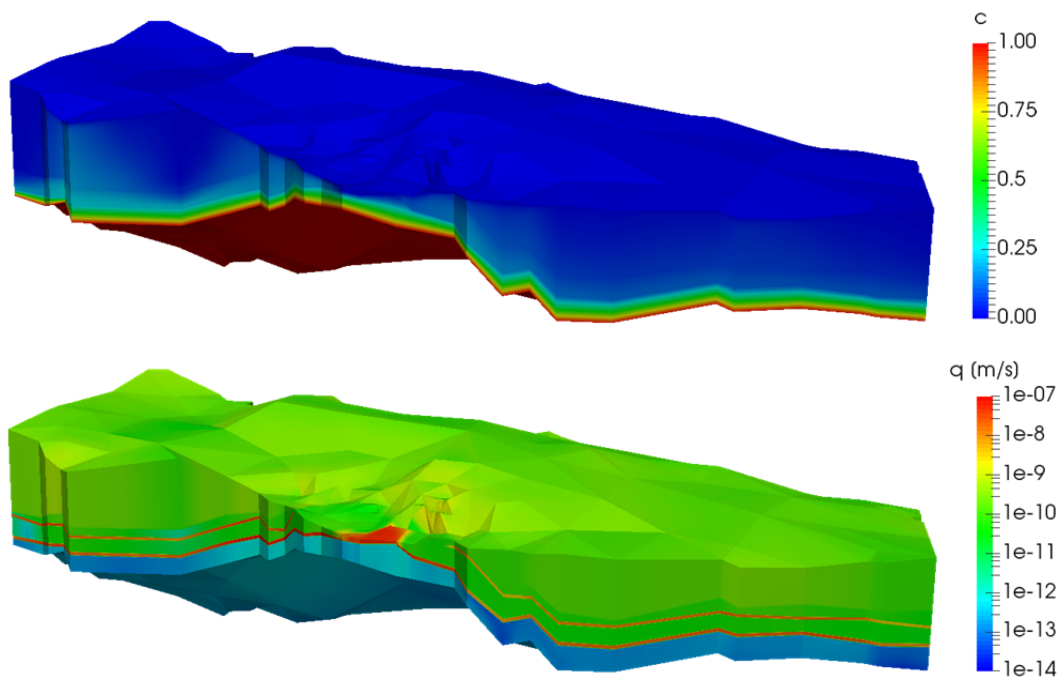
Fig. 5.8   WIPP-Site model with fixed groundwater table:
Results for salt concentration (above) and velocity field (below, on a logarithmic scale) after a model time of 14,000 years

In the lower graphic in Fig. 5.8 the higher velocities in the two thin, but highly permeable main aquifers Culebra Dolomite and Magenta Dolomite are clearly visible. The concentration plot above shows that in the major part of the model domain most of the brine is transported through these two aquifers. Only in some parts of higher permeabilities near the western boundary the salt reaches the upper layers.

In the next step the WIPP-Site model was set up with a free groundwater surface. As an initial condition the groundwater surface was placed near ground surface as shown at the in Fig. 5.7 (right).

To handle free surface groundwater flow d³f++ is using a level set method, see /FRO 12/ and /SCH 12/. The implementation of this method still leads to grave restrictions with regard to time step size, so that up to now only some months of model time could be computed. First results are shown in Fig. 5.9. The upper pictures show the strong movement of the free groundwater surface, where the velocity plot below shows the same characteristics as the correspondent graphic in Fig. 5.8. The upper, green part of picture 3 with apparently high velocities is situated above the groundwater surface, that means outside of the model domain and therefore irrelevant.
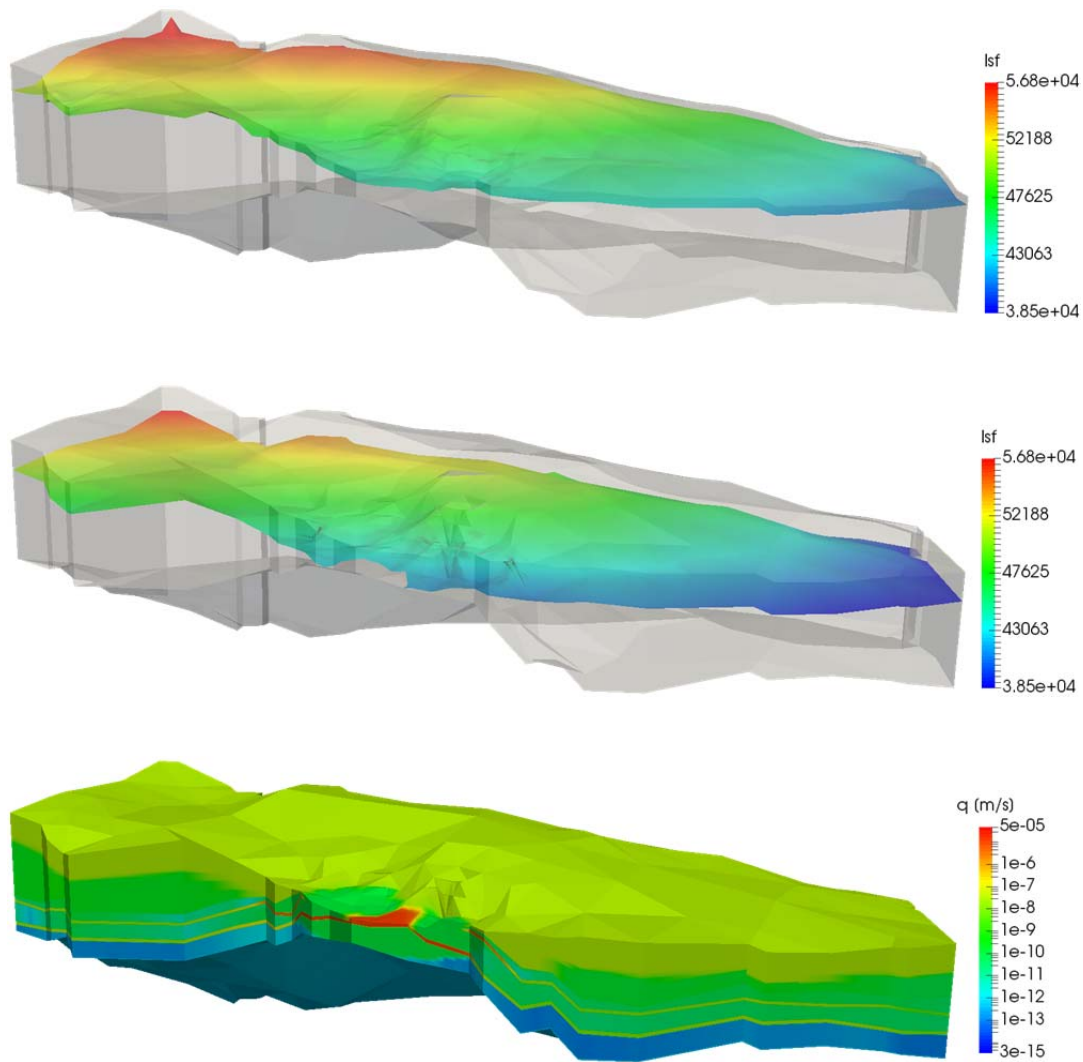
Fig. 5.9   WIPP-Site: results of free surface modeling

picture 1: free groundwater surface, initial condition

picture 2: simulated groundwater surface

picture 3: velocities (logarithmic scale)

5.5   Summary

The Waste Isolation Pilot Plant (WIPP) is a repository for transuranic waste situated in a semi-arid region east of Carlsbad, New Mexico, USA, in a thick, Permian-age deposit of bedded salt. This host rock formation is covered by flat bedded Permian halite, dolomite, anhydrite and clastic hydrogeological units as well as Triassic and Quaternary sandstone. The present model covers the whole overburden in the entire basin. The model domain has a horizontal extension of about 6,000 km², a depth of about 700 m and consists of flat bedded layers with contrasts in their permeabilities up to seven orders of magnitude, where the two main aquifers have a mean thickness of only 2 m.

These characteristics combined with the large horizontal extent of the model domain evoke high numerical anisotropies. A second challenge is the large free groundwater surface with extremely low groundwater recharge rates as an upper boundary condition.

The objective of this work was to show and to improve the ability of d³f++ to set-up a WIPP-like 3d model with a reasonable effort, to simulate density-driven groundwater flow correctly and, especially, to handle a free groundwater surface in such a big model.

Recent enhancements of the preprocessor ProMesh opened up the possibility of an almost automatic set-up of 3d geological models based on raster data describing the layer boundaries. Additionally, grid generation was significantly improved. Within the geometrical multigrid algorithms a new concept of grid refinement was developed, allowing very coarse grids on the base level without loss of geometrical information. The d³f++ solvers work very efficient despite of the high anisotropies. Modeling the large free groundwater surface was successful, even though the time step lengths are still not satisfying. This problem has to be overcome to reach the demanded model times.

The objective of current WIPP-Site modeling is to enhance the understanding of the groundwater flow dynamics in the basin in a time frame of tens of thousands of years and forecasting the impact of density effects. Finally, a comparison of the d³f++ results with PFLOTRAN-simulations /LIC 14/ is planned. The work will be continued in the framework of another BMWi funded project "Groundwater flow and transport in complex real systems" under contract no. 02E11476A.

6 Reactive transport

The simulation of reactive transport implies that both, transport and chemical reactions concerning the substances of interest are considered. Often, relatively simple physico-chemical reactions (e. g. sorption with linear distribution coefficients) are incorporated in transport models or a relatively simple representation of the transport process (e. g. 1D-transport) is assumed in geochemical models. A more sophisticated approach to reactive transport is the combination of a transport model and a geochemical model.

Such a combination – namely the coupling of the transport code r^3t /FEI 04/ with the geochemical code PHREEQC /PAR 13/ – was developed during the project "Radionu-clide transport modelling. Performance assessment of repositories in clays" /RUE 07/. Merging of r^3t and d^3f to the code d^3f++ /SCH 16/ brought the necessity to implement the coupling with PHREEQC anew and to adapt it to the altered code structure.

Comparative simulations were performed with the well-established code PHAST /PAR 10/ which contains PHREEQC in order to qualify the coupling of d^3f++ with PHREEQC.

6.1 Model setup

The model setup is based on a test case developed in the project WEIMAR (FKZ 02 E 11072A). The model domain consists of a one-dimensional horizontal column with a length of 20 m (cf. Fig. 6.1). An inflow with constant rate but changing chemical composition is situated at the left hand side of the model. The right hand side of the model is open to flow and transport.
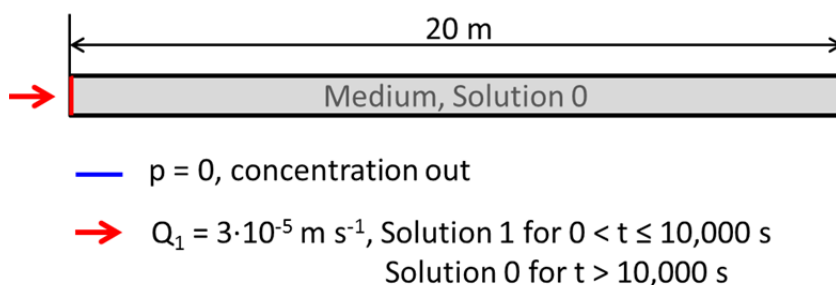
Fig. 6.1 Model domain with boundary conditions

The model domain comprises a homogeneous medium of a material mix whose components and their related reactive surfaces are listed in Tab. 6.1. The hydraulic parameters of the medium are set to typical values for aquifers (Tab. 6.2). It is assumed that calcite is present in the entire model domain and may be dissolved or precipitate from the solution at any time.

Tab. 6.1   Properties of material components

Mineral phase/group	Reference binding sites [sites/nm²]	Specific surface area [m²/g]	Solid mass [g/kgw]
Quartz	2.31	0.007	9,010
Feldspar	2.31	0.21	1,060
Mica	2.31	1.72	53
Fe(III)-oxids/-hydroxids	2.31	0.26	53
Al-hydroxids	2.31	0.11	53
2-layer-clay minerals	2.31	0.07	159

Tab. 6.2   Hydraulic parameters

Parameter	Unit	Value
Permeability κ	m^2	$1.019368 \cdot 10^{-11}$
Porosity ρ	-	0.2
Molecular Diffusion Coefficient D_m	$m^2 s^{-1}$	$1.0 \cdot 10^{-9}$
Longitudinal / Horizontal / Vertical Dispersivity D_L / D_H / D_V	m	0.0
Specific Storage S_S	m^{-1}	0
Tortuosity T	-	1.0
Density ρ	$kg\ m^{-3}$	$1.0 \cdot 10^3$
Viscosity μ	$kg\ m^{-1}\ s^{-1}$	$1.0 \cdot 10^{-3}$

The model domain is filled initially with Solution 0 (cf. Tab. 6.3). During the first 10,000 s, Solution 1 enters the model domain from the left. This solution has the same chemical composition as Solution 0 but additionally contains several radionuclides and bromide as tracer as listed in Tab. 6.3. After that, the inflow changes back to Solution 0 which prevails until the end of the simulation.

Tab. 6.3   Composition of Solution 0 and Solution 1

Parameter	Unit	Solution 0	Solution 1
pH	[-]	7.0	7.0
Ionic strength	[mol l^{-1}]	0.08104	0.08104
Na	[mol l^{-1}]	$1.0 \cdot 10^{-3}$	$1.0 \cdot 10^{-3}$
Cl	[mol l^{-1}]	$60.0 \cdot 10^{-3}$	$60.0 \cdot 10^{-3}$
Ca	[mol l^{-1}]	$25.02 \cdot 10^{-3}$	$25.02 \cdot 10^{-3}$
DIC	[mol l^{-1}]	$1.0 \cdot 10^{-3}$	$1.0 \cdot 10^{-3}$
Cs	[mol l^{-1}]		$1.0 \cdot 10^{-8}$
Ra	[mol l^{-1}]		$1.0 \cdot 10^{-8}$
Ni	[mol l^{-1}]		$1.0 \cdot 10^{-8}$
Am	[mol l^{-1}]		$1.0 \cdot 10^{-10}$
Th	[mol l^{-1}]		$1.0 \cdot 10^{-10}$
Np	[mol l^{-1}]		$1.0 \cdot 10^{-8}$
U	[mol l^{-1}]		$1.0 \cdot 10^{-8}$
Se	[mol l^{-1}]		$1.0 \cdot 10^{-8}$
Br	[mol l^{-1}]		$1.0 \cdot 10^{-8}$

6.2   Results

Tracer simulations with bromide were performed to compare the d^3f++-results with results from the code PHAST without the influence of sorption. The results after 100,000 s simulation time show a good agreement (Fig. 6.2). This implies that the flow and transport (without sorption) agree quite well.
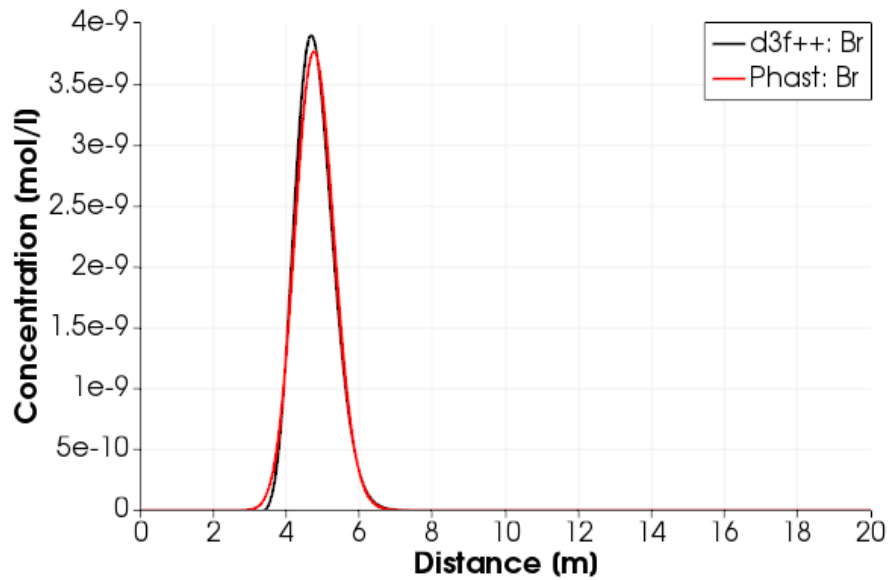
Fig. 6.2   Spatial distribution of bromide after 100,000 s simulation time

No further results can be shown here because the new implementation of the d^3f++ PHREEQC coupling on the ug4 platform is still in progress. It proved to be much more difficult than expected to bridge the structural differences between the two codes. Numerous problems have already been solved, e. g. the realization as a d³f++ plugin, building of the PHREEQC library and its linking to d³f++ for various architectures, and the control of simulation runs via LUA scripts. However, some problems still remained. This work will be continued.

7   Summary and conclusions

The objective of this report is proving the capability of the new code d³f++ to simulate density-driven flow and pollutant transport correctly in large scale, complex geological situations in order to improve the confidence in groundwater modeling in general. The applications presented here are related to haline and thermohydraulic groundwater flow and transport in porous or fractured media. Among them are laboratory and field experiments as well as real site studies. The d³f++ results are verified by measurements or compared to the results of other density-driven flow codes.

The applications presented in chapter 2 are related to Task 8 defined by the Task Force on Groundwater Flow and Transport of Solutes (TF GWFTS) of the Svensk Kärnbränslehantering AB (SKB) to investigate the hydraulic interaction of the granitic host rock and the bentonite clay buffer in a deep geological repository at the Hard Rock Laboratory (HRL) at Äspö. Presented are the results from work on the Buffer-Rock-Interaction-Experiment (BRIE) in the framework of Tasks 8c and 8d and on the Prototype Repository in the framework of Task 8e.

- The flow model for Task 8c was able to reproduce the trend of a pressure decrease along the tunnels which had been observed in the series of five probing boreholes. The calculated flow rates for all boreholes lay within a factor of four of the measured values. Parameter variations confirmed that inflow rates are mainly depending on matrix permeability and on additional water-bearing fractures that were opened by these boreholes. The large deterministic fractures have apparently little influence on these flow rates. It is not clear if this has to do with an unsuitable location of the model boundary or with the heterogeneities introduced by the network of background fractures. Parameter variations indicated a surprisingly high effective permeability of the rock matrix including background fractures in comparison to the values for the undisturbed matrix. It suggests on a larger scale a network of rather well-connected smaller fractures.

- Task 8d differs from 8c by some additional probing boreholes and more outflow and pressure measurements. Conceptionally, the direct modelling of assumed fractures to account for the locally varying outflow from borehole to borehole had been dropped in favour of a low permeable skin at tunnel and borehole walls which was believed to be a more general approach. The set of permeabilities for the reference case provided already a good match with the measured and estimated outflow

rates indicating that a good approximation within the limits of the model concept has been found.

The outflow from the boreholes was too high by a factor of up to 10. The inconsistent trend of increasing pressure in the model and the measured decreasing outflow towards the end of the tunnel indicates an influence of background fractures that could not be captured by a deterministic model.

- Subtask 8e is concerned with the full-scale Prototype Repository (PR) at the HRL at Äspö. To simulate the operational phase of a repository, the boreholes contain heaters and buffer during the experiment. Other differences between the BRIE and the PR concern the geometry of the geotechnical openings and the size of the in-situ tests thus allowing for a check of the approach developed for the BRIE. Work on Task 8 served the purpose of calculating outflow data from the rock as well as testing the features for flow and transport in fractured rock that were newly implemented in d^3f++ /SCH 12/.

As a result, the strongest influence of the heating on fracture flow is not observed in the major but in the minor deterministic fractures because the thermal influence of the heaters on the rock temperature is spatially rather limited. The major fractures therefore see hardly any significant temperature increase. The minor fractures, by contrast, are even cutting through the deposition holes so that heating causes a maximum impact on fracture flow.

In the Borden field research site, a thermal injection and storage experiment was conducted to investigate the feasibility of storing thermal energy in shallow unconfined aquifers near the water table. A certain volume of heated water was injected through a well. During the whole storage period of 135 days groundwater temperatures were measured. The experiment forms an excellent basis for qualifying d^3f++ with respect to coupled groundwater flow with free water surface and heat transport which has already been done in the past by /MOL 92/. The subject of the work presented here is the simulation and reproduction of the results using d^3f++. The flow and heat transport with free water surface as well as the heat flow without free water surface using d^3f++ are studied in this chapter separately because d^3f++ does presently not allow simulation of heat conduction above the groundwater surface, meaning outside the model domain. Groundwater flow and heat transport were studied in two and three dimensions on the same coarse grid but with different refinement levels, so that grid convergence could be examined. Furthermore, the influence of the heat transfer factor α, which controls

the heat transfer between the atmosphere and the aquifer, was studied. The results were compared to experimental results from the field. It was found that variation of factor α has only influence on the temperature distribution of the upper and middle part of the aquifer. Smaller α lead to a better fit in the upper part of the temperature profile, whereas larger α result in a better fit in the middle part of the temperature profile. The development of the peak plume temperature from simulation matched very well with the results observed in the field. It could be shown that d³f++ can deal with the heat and groundwater flow in 2d and 3d models and reproduce the results of the field experiment.

Benchmarks based on laboratory experiments are also very important for testing of numerical codes. The benchmark published in /STO 12/ can serve as a lab-scale principal model for the formation and degradation of a freshwater lens in the case of a homogeneous aquifer. This 2d benchmark allowed to compare the results of various density-driven flow codes with regard to the modeling of building-up and degradation of freshwater lenses. All five numerical codes were able to adequately reproduce the experimental results, but also some deviations arose resulting from differences in the numerical solvers and available boundary conditions. The code d³f++ could prove its capability to simulate formation and degradation of a freshwater lens physically correctly, and it came out ahead of this comparison.

The Waste Isolation Pilot Plant (WIPP) is a repository for transuranic waste in New Mexico, USA. The model presented in this report covers the overburden with a horizontal extension of about 6,000 km². It consists of flat bedded layers with contrasts in their permeabilities over up to seven orders of magnitude, where the two main aquifers have a mean thickness of only 2 m. These characteristics combined with the large horizontal extension of the model domain evoke high numerical anisotropies. The objective of this work was to enhance the understanding of the groundwater flow dynamics in the basin as well as to show the ability of d³f++ to set-up a 3d model with an extreme ratio between vertical and horizontal extent, to handle a series of hydrogeological layers with highly differing properties in such a geometry and permeability, to simulate density-driven groundwater flow correctly and, especially, to handle a free groundwater surface of these dimension. The d³f++ solvers worked very efficient despite of the high anisotropies. Modeling the large free groundwater surface was successful, even though the time step lengths are still not satisfying. This problem has to be overcome to reach the demanded model times. The work will be continued in the frames of another BMWi

funded project. Finally, a comparison of the d³f++ results with PFLOTRAN-simulations /LIC 14/ is planned.

The new implementation of d³f++ on the UG4 platform turned out to be much more difficult than expected with respect to bridging the structural differences between the two codes d³f++ and PHREEQC. Numerous problems have already been solved, but up to now only simple test cases could be realized.

8 References

/ALM 05/ Alm, P., Forsmark, T., Rhén, I.: Prototype Repository Installations for meas-urements of flow Repository into tunnels, water pressure in rock Repository and hydromechanical responses in Repository boreholes during operation phase. International Progress Report IPR-05-04, SKB, 2005.

/BAS 97/ Bastian, P., Birken, K., Johannsen, K., Lang, S., Neuß, N., Rentz-Reichert, H., Wieners, C.: UG – A flexible software tool for solving partial differential equations. Computing and Visualization in Science 1, 27-40, 1997.

/BOC 13/ Bockgård, N., Vidstrand, P., Åkesson, M.: Modelling the interaction be-tween engineered and natural barriers – An assessment of a fractured bedrock de-scription in the wetting process of bentonite at deposition tunnel scale. Technical Committee of Task 8, SKB, Rev. 2013-10-27, 2013.

/BRU 12/ Brunner, Philip; Simmons, Craig T. "HydroGeoSphere: A Fully Integrat-ed, Physically Based Hydrological Model". Groundwater. 50 (2): 170–176, 2012.

/COM 13/ COMSOL: COMSOL Multiphysics Reference Manual version 4.4, COMSOL AB, 2013.
http://www2.humusoft.cz/ftp/comsol/guides/COMSOL_ReferenceManual.pdf

/COR 96/ Corbet, T., Krupp, P.: The role of regional groundwater flow in the hy-drogeology of the Culebra member of the Rustler formation at the Waste Isolation Pilot Plant (WIPP), Southeastern New Mexico, SAND96-2133, Albuquerque, 1996.

/COR 00/ Corbet, T.: A groundwater-basin approach to conceptualize and simulate post-Pleistocene subsurface flow in a semi-aride region, southeastern New Mexico and western Texas, USA; Hydrogeology Journal 8:310-327, 2000.

/DAV 89/   Davies, P., Variable-density ground-water flow and paleohydrogeology in the Waste Isolation Pilot Plant (WIPP) region, southeastern New Mexico, USGS Open File Report 88-490, USA, 1989.

/KOE 16/   König, C., Becker, M., Diehl, A., Seidel, T., Rosen, B., Rüber, O., Zimmermann, C.: SPRING – Simulation of Processes in Groundwater, Benutzerhandbuch, delta h Ingenieurgesellschaft mbH, http://spring.delta-h.de, Witten, 2016.

/DIE 14/   Diersch, H.-J.G., 2014. FEFLOW: Finite element modeling of flow, mass and heat transport in porous and fractured media, Springer Heidelberg, New York, Dordrecht, London, ISBN 978-3-642-38738-8, 996 pp, 2014.

/DOS 13/   Dose, E.J., et al. Experiments and modeling of freshwater lenses in layered aquifers: Steady state interface geometry. Journal of Hydrology, J. Hydrol. 509: 621–630. DOI: 10.1016/j.jhydrol.2013.10.010.

/FEI 99/   Fein, E.; Schneider, A. (eds.): d3f – ein Programmpaket zur Modellierung von Dichteströmungen. Final report. FKZ-02 C 0465 0. Gesellschaft für An-lagen- und Reaktorsicherheit (GRS) mbH, GRS-139, Braunschweig 1999.

/FEI 04/   Fein, E. (ed.): Software Package r^3t. Model for Transport and Retention in Porous Media. Final Report, FKZ 02 E 9148/2 (BMWA), Gesellschaft für Anlagen- und Reaktorsicherheit (GRS) gGmbH, GRS-192, 2004.

/FEI 08/   Fein, E.; Kröhn, K.-P.; Noseck, U.; Schneider, A.: Modelling of field-scale pollutant transport. Final report. FKZ-02 E 9934. Gesellschaft für Anlagen- und Reaktorsicherheit (GRS) mbH, GRS-231, Braunschweig 2008.

/FET 72/   Fetter, C.W., 1972. Position of the saline water interface beneath oceanic islands. Water Resour. Res. 8, 1307–1314.

/FOR 01/   Forsmark, T., Rhén, I., Andersson, Ch.: Prototype Repository: Hydrogeology – Deposition- and lead-through boreholes: Inflow measurements, hydraulic responses and hydraulic tests. International Progress Report IPR-00-33, SKB, 2001.

/FOR 05/   Forsmark, T. and Rhén, I.: Prototype Repository: Hydrogeology – Hydrogeology – diaper measurements in DA3551G01 and DA3545G01, flow measurements in section ll and tunnel G, past grouting activities. International Progress Report IPR-05-03, SKB, 2005.

/FRA 12a/   Fransson, Å., personal communication, 2012.

/FRA 12b/   Fransson, Å.:Bentonite Rock Interaction Experiment (BRIE). Presentation on the Meeting #28 of the TF GWFTS, Berlin, 2012.

/FRA 15/   Fransson, Å., Åkesson, M., Andersson, L.: Bentonite Rock Interaction Ex-periment Characterization of rock and installation, hydration and dismantling of bentonite parcels. Report R-14-11 (draft), Swedish Nuclear Fuel and Waste Management Company (SKB), Stockholm, 2014.

/FRO 12/   Frolkovič, P.: Application of level set method for groundwater flow with moving boundary, Adv. Wat. Res. 2012

/GRI 10/   Grillo, A., Lampe, M., Wittum, G.: Three-dimensional simulation of the thermohaline-driven buoyancy of a brine parcel, Comput Visual Sci 13 287–297, 2010.

/HEP 13/   Heppner, I., Lampe, M., Nägel, A., Reiter, S., Rupp, M., Vogel, A., Wittum, G.: Software framework UG4: Parallel multigrid on the hermit supercom-puter. In: High Performance Computing in Science and Engineering 12, p. 435-449, Springer, 2013.

/HOF 13/   Hoffer, M., Poliwoda, C., and Wittum, G.: Visual reflection library: a frame-work for declarative GUI programming on the Java platform. Computing and Visualization in Science 16 (4), 181-192, 2013.

/IAP 03/   The International Association for the Properties of Water and Steam: Revised Release on the IAPWS Formulation 1985 for the Viscosity of Ordinary Water Substance. 2003. Homepage: http://www.iapws.org.

/JOH 02/   Johannsen, K., Kinzelbach, W., Oswald, S., Wittum, G.: The saltpool benchmark problem - numerical simulation of saltwater upconing in a porous medium, ADVANCES IN WATER RESOURCES 25 (2002) 309–1708.

/KOL 11/   Kolditz, O. and Shao, H. (eds.): OpenGeoSys – Developer Benchmark Book 5.0.04, Internet Report, available through www.opengeosys.net, Helmholtz Centre for Environmental Research, AESA TU Dresden, 2011.

/KRI 07/   Kristensson, O. and Hökmark, H.: Prototype Repository - Thermal 3D modelling of Äspö Prototype Repository. Report IPR-07-01, SvenskKärnbränslehantering AB (SKB), Stockholm, 2007.

/KRI 10/   Kristensson, O. and Johannesson, L.-E.: Description of the Prototype Repository Test compiled for EBS Task-Force. (includes accompanying data files) Clay Technology Ab, draft version, 2010.

/KRO 96/   Kröhn, K.-P., Schelkes, K.: Modelling of regional variable density groundwater flow in an area in New Mexico: importance of onfluencing parameters and processes. In: Calibration and Reliability in Groundwater Modelling (Proceedings of the ModelCARE 96 Conference held at Golden, Colorado, September 1996), pp 353-361, 1996.

/KRO 10/   Kröhn, K.-P.: State Variables for Modelling Thermohaline Flow in Rocks. FKZ 02 E 10336 (BMWi), Gesellschaft für Anlagen- und Reaktorsicherheit (GRS) mbH, GRS-268, Köln, 2010.

/KRO 17a/   Kröhn, K.-P.: Hydraulic Interaction of Engineered and Natural Barriers – Task 8b-8d,8f of SKB. Summary report, FKZ 02 E 11213 and 02 E 11102 (BMWi), Gesellschaft für Anlagen- und Reaktorsicherheit (GRS) mbH, GRS-430, Braunschweig, 2017. (under review).

/KRO 17b/   Kröhn, K.-P.: Hydraulic Interaction of Engineered and Natural Barriers – Task 8e of SKB. Summary report, FKZ 02 E 11213 and 02 E 11102 (BMWi), Gesellschaft für Anlagen- und Reaktorsicherheit (GRS) mbH, GRS-431, Köln, 2017. (in preparation)

/KUL 02/   Kull, H. (ed.), Helmig, R., Jacobs, H., Jockwer, N., Kröhn, K.-P., Zimmer, U.: Two-Phase-Flow Experiment in the Fractured Crystalline Rock of the Äspö Hard Rock Laboratory. Final Report. FKZ-02 E 9027 8. Gesellschaft für Anlagen- und Reaktorsicherheit (GRS) mbH, GRS-183, Braunschweig, 2002.

/LIC 14/   Lichtner, P. C., Hammond, G. E., Lu, C., Karra, S., Bisht, G., Andre, B., Mills, R. T., and Kumar, J.: PFLOTRAN user manual: A massively parallel reactive flow and transport model for describing surface and subsurface processes. http://www.pflotran.org/ 2014.

/MAT 04/   Matthäi, S.K. and Belayneh, M.: Fluid flow partitioning between fractures and a permeable rock matrix. Geophysical Research Letters, vol. 31, L07602, doi: 10.1029/2003GL019027, 2004.

/MOL 92/   Molson, J. W., Frind, E. O., Palmer, C. D.: Thermal energy storage in an unconfined aquifer: 2. Model development, validation, and application. Water Resources Research, vol. 28, no. 10, p. 2857, 1992.

/MOL 92a/   Molson, J. W., Frind, E. O., Palmer, C. D.: Thermal energy storage in an unconfined aquifer: 1. Field Injection Experiment. Water Resources Research, vol. 28, no. 10, p. 2845, 1992

/NOS 12/   Noseck, U., Brendler, V., Flügge, J., Stockmann, M., Britz, S., Lampe, M., Schikora, J., Schneider, A..: Realistic integration of sorption processes in transport codes for long-term safety assessments, Final Report GRS-297, BMWi-FKZ 02E10548. Gesellschaft für Anlagen- und Reaktorsicherheit (mbH), Braunschweig, (2012), 293 p.

/OLD 98/   Oldenburg, C., Pruess, K.:Layered thermohaline convection in hypersalinegeothermal systems. Transport in porous media 33:29-63, 1998.

/OLS 92/   Olsson, O. (ed.): Site Characterisation and Validation – Final Report. Technical Report TR 92-22, Swedish Nuclear Fuel and Waste Management Company (SKB), 1996.

/OSW 98/   Oswald, S.: Dichteströmungen in porösen Medien: Experimente und Modellierung. Dissertation, ETH Zürich, Nr. 12812, 1998.

/PAL 92/   Palmer, C. D., Blowes, D. W., Frind, E. O., Molson, J. W.: Thermal energy storage in an unconfined aquifer: 1. Field Injection Experiment. Water Resources Research, vol. 28, no. 10, p. 2845, 1992.

/PAR 10/   Parkhurst, D.L., Kipp, K.L., and Charlton, S.R., 2010, PHAST Version 2—A Program for Simulating Groundwater Flow, Solute Transport, and Multicomponent Geochemical Reactions: U.S. Geological Survey Techniques and Methods 6-A35, 235 p.

/PAR 13/   Parkhurst, D.L., and Appelo, C.A.J.: Description of input and examples for PHREEQC version 3—A computer program for speciation, batch-reaction, one-dimensional transport, and inverse geochemical calculations. U.S. Geological Survey Techniques and Methods, book 6, chap. A43, (2013) 497 p.

/PAT 97/   Patel, S., Dahlstrom, L.-O., Stenberg, L.: Characterisation of the Rock Mass in the Prototype Repositoryat Äspö HRL Stage 1. Report HRL-97-24, SvenskKärnbränslehantering AB (SKB), Stockholm, 1997.

/REI 13/   Reiter, S., Vogel, A., Heppner, I., Rupp, M., Wittum, G.: A massively parallel geometric multigrid solver on hierarchically distributed grids. Computing and Visualization in Science 16 (4), 151-164, 2013.

/RHÉ 01/   Rhén, I. and Forsmark, T.: Prototype Repository - Hydrogeology - Summary report of investigations before the operation phase. International Progress Report IPR-01-65, SKB, 2001.

/RUE 07/   Rübel, A., Becker, D., Fein, E.: Radionuclide transport modelling - Performance assessment of repositories in clays. FKZ 02 E 9813. Gesellschaft für Anlagen- und Reaktorsicherheit (GRS) mbH, GRS-228, Braunschweig 2007.

/SCH 04/   Schneider, A.; Birthler, H.: Modellrechnungen zur großräumigen dichte-ab-hängigen Grundwasserbewegung. FKZ-02 C 0628 4. Gesellschaft für An-lagen- und Reaktorsicherheit (GRS) mbH, GRS-191, Braunschweig 2004.

/SCH 12/   Schneider, A. (ed.): Enhancement of d3f und r3t (E-DuR). Final report, FKZ 02 E 10336 (BMWi), Gesellschaft für Anlagen- und Reaktorsicher-heit (GRS) mbH, GRS-292, 2012.

/SCH 13/   Schneider, A. (ed.), Representation of inhomogeneities in the flow and transport codes d³f and r³t, GRS 311, Braunschweig, 2013.

/SCH 16/   Schneider, A. (ed.): Modelling of Data Uncertainties on Hybrid Comput-ers (H-DuR). Final report, FKZ 02 E 11062A (BMWi), Gesellschaft für Anlagen- und Reaktorsicherheit (GRS) gGmbH, GRS-392, 2016.

/STO 12/   Stoeckl, L., Houben, G., Flow dynamics and age stratification of fresh-water lenses: Experiments and modelling. Journal of Hydrology, Vol-umes 458–459, 21 August 2012, Pages 9-15.

/STO 14/   Stoeckl, L., Walther, M., Schneider, A., Yang, J., Graf, T.: Comparison of numerical models using a two-dimensional benchmark of density-driven flow. 23th Salt Water Intrusion Meeting, June 16-20, Husum, Germany, 2014.

/STO 16/   Stoeckl, L.: Variable-Density Flow in the Subsurface of Oceanic Islands: Physical Experiments and Numerical Modeling. PHD-Thesis, Leibniz-University Hannover, 2016.

/SUN 05/   Sundberg, J., Back, P.-E., Hellström, G.: Scale dependence and esti-mation of rock thermal conductivity. Report R-05-82, SvenskKärnbräns-lehantering AB (SKB), Stockholm, 2005.

/SVE 12/   Svensson, U.: Task 8 Modelling a one m3 block of granite. Presentation at the 28th Meeting of the Task Force on Groundwater and Transport of So-lutes, Berlin, 2012.

/VAC 90/   Vacher, H.L., Bengtsson, T.O., Plummer, L.N., 1990. Hydrology of meteoric diagenesis: residence time of meteoric ground water in island fresh-water lenses with application to aragonite-calcite stabilization rate in Bermuda. Geolog. Soc. Am. Bul. 102 (2), 223–232.

/VID 11/   Vidstrand, P., personal communication, 2011.

/VIL 07/   Vilks, P.: Forsmark site investigation – Rock matrix permeability measurements on core samples from borehole KFM01D. Report P-07-162, Svensk Kärnbränslehantering AB (SKB), Stockholm, 2007.

/VOG 13/   Vogel, A., Reiter, S., Rupp, M., Nägel, A., Wittum, G.: UG 4: A novel flexible software system for simulating PDE based models on high performance computers. Computing and Visualization in Science 16 (4), 165-179, 2013.

/VOS 84/   Voss, C.I.: A finite-element simulation model for saturated-unsaturated, fluid-density-dependent ground-water flow with energy transport or chemically reactive single-species solute transport: U.S. Geological Survey Water-Resources Investigations Report 84-4369, 409 p, 1984.

Table of figures

141

142

143

List of tables